

Nonequilibrium Dynamics of Strongly Correlated Quantum Systems

Von der Fakultät Mathematik und Physik
der Universität Stuttgart
zur Erlangung der Würde eines
Doktors der Naturwissenschaften (Dr. rer. nat.)
genehmigte Abhandlung

Vorgelegt von

Salvatore Rosario Manmana

aus Catania (Italien)

Hauptberichter: Prof. Dr. Alejandro Muramatsu

Mitberichter: Prof. Dr. Reinhard M. Noack

Tag der mündlichen Prüfung: 13.12.2006

Institut für Theoretische Physik der Universität Stuttgart

2006

Table of Contents

Zusammenfassung	4
1 Introduction	5
I Numerical Methods for Strongly Correlated Quantum Systems	9
2 Strongly Correlated Quantum Systems	11
2.1 Models	12
2.1.1 Integrability of Quantum Systems	17
2.2 One dimensional systems: Luttinger Liquids	18
2.3 Quantum Criticality	22
2.4 Experimental Realization in Optical Lattices	25
2.5 Strongly Correlated Systems out of Equilibrium	27
2.5.1 Thermalization	28
3 Krylov Space Approach to Calculating the Time Evolution	35
3.1 Iterative Diagonalization Methods	35
3.1.1 Implementation of Quantum Many Body Systems	36
3.1.2 The Lanczos and the Jacobi-Davidson Algorithm	38
3.2 Time Evolution with the Lanczos Method	45
4 The Density Matrix Renormalization Group Method for Systems in Equilibrium	51
4.1 RG-like methods for a particle in a box	52
4.2 Density Matrix Projection for Interacting Systems	55

4.3	DMRG Algorithms	57
4.3.1	Infinite System Algorithm	58
4.3.2	Finite System Algorithm	59
4.3.3	Programming Details	61
4.3.4	Measurements	64
4.3.5	Wave Function Transformations	65
5	Applying the DMRG: Susceptibilities and Correlation Functions of the Ionic Hubbard Model	69
5.1	Introduction	69
5.1.1	Model and exactly solvable limits	71
5.1.2	Details to the Application of the DMRG	74
5.2	Energy gaps	75
5.3	Ionicity	78
5.4	Order parameters and susceptibilities	79
5.4.1	The bond order parameter and susceptibility	79
5.4.2	The electric susceptibility and the density-density correlation function	86
5.5	Summary	91
6	Adaptive Time-Dependent Density Matrix Renormalization	93
6.1	Time-Evolution Schemes	94
6.1.1	Lanczos t-DMRG	96
6.1.2	Trotter t-DMRG	97
6.1.3	Comparing the Adaptive Lanczos and Trotter t-DMRG Variants	98
6.2	Error analysis	99
6.2.1	Accuracy of the Method for a Quench Scenario	100
6.2.2	Accuracy of the Method for Wavepacket Dynamics	102
6.3	Discussion	103

II Time Evolution of Strongly Correlated Quantum Sys-

tems	109
7 Coherent Matter Waves of Interacting Bosons on a Lattice	111
7.1 Local Density and Momentum Distribution Function	113
7.2 Spatial Decay of Correlations	115
7.3 Conclusions	116
8 Strongly Correlated Fermions after a Quantum Quench	119
8.1 The Strong Coupling Limit	121
8.2 Relaxation to a Non-Thermal Quasi-Stationary State	122
8.3 Application of the Generalized Gibbs Ensemble	125
8.4 Discussion	128
9 Summary and Conclusion	129
Appendix A: Details to the t-DMRG	133
Appendix B: Time Dependence of the OPDM after a Quantum Quench to the Atomic Limit	137
Bibliography	140
Publications	150
Curriculum Vitae	153
Acknowledgements	154

List of Figures

2.1	Sketch of the tight-binding chain.	14
2.2	Virtual exchange processes leading to antiferromagnetic Heisenberg coupling.	16
2.3	Phase diagram of the quantum Ising model with transverse field.	22
3.1	Convergence behavior of the Lanczos algorithm.	42
3.2	Error of the Lanczos time evolution method.	48
4.1	The lattice and the flowchart for the DMRG iteration scheme.	52
4.2	Failure of the NRG for a quantum particle in a box.	53
4.3	Typical superblock configuration for DMRG algorithms.	58
4.4	A step in the finite system algorithm.	60
4.5	Convergence of the DMRG.	62
4.6	Superblock configuration relevant for the wave function transformation.	65
5.1	Gaps after extrapolating $L \rightarrow \infty$	77
5.2	Ionicity for various values of δ	78
5.3	Scaling of the bond order parameter for $\delta = 20$	80
5.4	The bond order parameter in the thermodynamic limit.	81
5.5	The BO parameter with a finite dimerization field.	83
5.6	The bond order susceptibility.	84
5.7	Finite size extrapolation of the bond order susceptibility.	85
5.8	A scaling analysis of χ_{BO} for $\delta = 20$	86
5.9	Electric susceptibility.	88
5.10	The density-density correlation function in the strong coupling limit.	89

6.1	Variants of the t-DMRG.	94
6.2	Flowcharts Lanczos and Trotter t-DMRG	96
6.3	Errors in $\langle n_k \rangle$ for a system with 18 sites	99
6.4	Relative error in the energy for $L = 24$ sites.	104
6.5	Relative error in $\langle n_k \rangle$ for $L = 24$	105
6.6	Absolute error in the density-density correlation function for $L = 24$.106	
6.7	Comparison of the errors for a Lanczos t-DMRG run with large dt versus Trotter t-DMRG with small dt	107
6.8	Error analysis for initially trapped hard-core bosons.	108
7.1	Time evolution of $\langle n_i \rangle$ for an initial Fock state of HCBs.	112
7.2	Comparison between HCBs and SCBs	114
7.3	Momentum distribution function and position of the peaks for SCBs.115	
7.4	Spatial decay of the OPDM.	116
7.5	The lowest natural orbital.	117
8.1	Collapse and revival of an initial Luttinger liquid state.	121
8.2	Analysis of the quasi-stationary state in the integrable case.	123
8.3	Time-averaged momentum distribution $\langle n_k \rangle$ for $V=10$	124
8.4	The quasi-stationary state in the non-integrable case.	125
8.5	Analysis for a system accessible to full diagonalization.	126
8.6	Influence of the constraints $\langle H^n \rangle$ on the energy distribution func- tion $P(E)$	127
1	Time dependence of the number of density-matrix eigenstates.	134
2	Time dependence of the number of the discarded weight.	135
3	Dimension of the density-matrix basis and discarded weight for initially trapped hard-core bosons.	136

List of Tables

2.1	Critical exponents for the classical Ising model in two spatial dimensions.	24
3.1	Reduction of the dimension of the Hilbert space when respecting symmetries.	37
6.1	Errors in $\langle n_k \rangle$ at time $t = 15$	100

Zusammenfassung

In dieser Arbeit werden stark korrelierte Quantenvielteilchensysteme in Gleichgewichts- und Nichtgleichgewichtssituationen untersucht. Dazu werden etablierte numerische Methoden angewandt und weiterentwickelt. Der Schwerpunkt der Arbeit liegt dabei in der Weiterentwicklung der *Dichtematrixrenormierungsgruppe* (DMRG) zur Behandlung quantenmechanischer Vielteilchensysteme ausserhalb des Gleichgewichts.

Die DMRG ist eine der exaktesten Methoden zur Untersuchung eindimensionaler Quantensysteme auf Gittern. Nach ihrer Einführung 1992 durch S. White [1] wurde sie weiterentwickelt um dynamische Korrelationsfunktionen und Systeme bei endlichen Temperaturen zu berechnen. In ihren Varianten ist sie auf eine Vielzahl von Problemen angewandt worden und wird nun als ein Standardverfahren für niedrigdimensionale Quantenvielteilchensysteme angesehen; für eine Einführung in die Methode und eine Übersicht über die mit diesem Verfahren behandelten Probleme Verweisen wir auf die Literatur [2, 3, 4].

Die Möglichkeit, ultrakalte Atome in *optischen Gittern* zu speichern [5], hat in den letzten Jahren die experimentelle Untersuchung stark korrelierter Quantensysteme weit voran getrieben. Das vielleicht bekannteste Beispiel ist die experimentelle Realisierung eines *Mott-Isolators* in einem optischen Gitter [6]. Die Experimente lassen ein hohes Mass an Kontrollmöglichkeiten zu. Dies ermöglicht es, Quantenvielteilchensysteme auch *ausserhalb* des Gleichgewichts kontrolliert zu untersuchen. Prominente Beispiele dafür sind der “Collapse and Revival” eines Bose-Einstein-Kondensats (BEC) [7], die Realisierung einer “Newtonschen Wiege” mit ultrakalten Atomen [8], und das “Quenchen” eines ferromagnetischen Spinor-BECs [9]. Das Grundprinzip, das die Speicherung ultrakalter Atome in optischen Gittern ermöglicht, ist die Wechselwirkung zwischen einem durch ein externes elektrisches Feld induziertes *Dipolmoment* in den Atomen mit einem elektrischen Feld. Im Fall der optischen Gitter wird dieses elektrische Feld durch einen Laserstrahl bereitgestellt. Ein periodisches Gitter kann dann erhalten werden indem gegeneinander laufende Strahlen überlagert werden. Durch Ändern der Parameter der Laserstrahlen kann nun das Experiment sehr genau kontrolliert werden. Es ist, vor allem, auch möglich, die *Wechselwirkung* zwischen den

Teilchen zu beeinflussen, so dass das System in einer wohldefinierten Weise aus dem Gleichgewicht gebracht werden kann.

Ist die Wechselwirkung sehr stark, so treten starke *Korrelationseffekte* auf, so dass das System nicht mehr durch effektive Einteilchenmodelle, wie z.B. in der Mean-Field-Näherung, behandelt werden kann. Es ist zwar möglich, einige Systeme mit Hilfe des *Bethe-Ansatzes* exakt zu lösen, aber im allgemeinen ist es notwendig auf Näherungsverfahren, wie z.B. die Störungstheorie, zurückzugreifen. Diese Verfahren sind aber für bestimmte Parameterwerte nicht gut kontrolliert und können zu fehlerhaften Ergebnissen führen. Daher ist es wichtig, effiziente *numerische Verfahren* zur Verfügung zu haben. Ausser der bereits erwähnten DMRG werden wir in dieser Arbeit auch exakte Diagonalisierungsverfahren, wie die Lanczos- oder die Jacob-Davidson-Methode, behandeln. Eine Erweiterung des Lanczos-Verfahrens ermöglicht es, die Zeitentwicklung stark korrelierter Quantensysteme mit einer Genauigkeit vergleichbar zur *Maschinengenauigkeit* zu berechnen. Diese Methode ist die Grundlage für eine mögliche Erweiterung der DMRG zur Behandlung von Nichtgleichgewichtsproblemen, der sogenannten *adaptiven zeitabhängigen DMRG* (“adaptive t-DMRG”). Eine zweite Variante der adaptiven t-DMRG baut auf der Suzuki-Trotter-Zerlegung des Zeitentwicklungsoperators auf [10]. Eine Fehleranalyse zeigt, dass beide Methoden, bei geeigneter Wahl der Kontrollparameter, am Ende der Zeitentwicklung einen Fehler von $< 1\%$ für schwierig zu berechnende Observablen, wie z.B. die Impulsverteilungsfunktion, besitzen. In dieser Arbeit werden diese Methoden eingesetzt, um zwei Nichtgleichgewichtssituationen von aktuellem Interesse zu untersuchen. Als erstes wird ein System aus sogenannten *soft-core* Bosonen, die anfangs in einem Fallenpotential festgehalten wurden, nach dem Ausschalten des Potentials untersucht. Ähnlich wie für sogenannte *hard-core* Bosonen, die *exakt* behandelt werden können, entstehen (quasi-)kohärente Materiewellen, die die Möglichkeit zur Realisierung eines *Atomlasers* auf optischen Gittern aufzeigen. Die zweite von uns untersuchte Nichtgleichgewichtssituation ist ein System stark korrelierter Fermionen nach einem sogenannten “Quanten-Quench”, d.h., nach einer plötzlichen Änderung eines *intrinsischen* Parameters, wie z.B. der Stärke der Wechselwirkung zwischen den Teilchen. Bei diesem System interessieren wir uns vor allem für das Verhalten nach langen Zeiten; insbesondere stellt sich die Frage, ob, Boltzmanns *Ergodenhypothese* folgend, ein *thermischer* Zustand erhalten wird.

Die Arbeit ist wie folgt gegliedert. In Kapitel 2 werden stark korrelierte Quantensysteme eingeführt und die für diese Arbeit relevanten Modelle vorgestellt. Die Konzepte *Luttinger-Flüssigkeit* und *Quantenkritikalität* und die mögliche Realisierung von Quantenvielteilchensystemen in optischen Gittern werden diskutiert. In Abschnitt 2.5 werden Nichtgleichgewichtssituationen stark korrelierter

Quantensysteme diskutiert, wobei ein besonderes Augenmerk auf die Ergodenhypothese und die mögliche *Thermalisierung* solcher Systeme gelegt wird.

In den Kapiteln 3 und 4 werden die für diese Arbeit wichtigen numerischen Methoden und ihre Implementierung vorgestellt. In Abschnitt 3.2 wird die Erweiterung der Lanczos-Methode für zeitabhängige Probleme vorgestellt und ihr Fehler untersucht, der innerhalb von Hochbruck und Lubich [11] gefundenen Fehlergrenzen liegt. Wie bereits erwähnt, sind die Fehler sehr klein und können von der Grössenordnung der Maschinengenauigkeit gehalten werden.

In Kapitel 5 wird die DMRG Methode angewandt um das Quantenkritische Verhalten des sogenannten *ionischen Hubbardmodells* zu untersuchen. Die numerischen Ergebnisse stimmen mit einem Phasendiagramm mit *zwei* kritischen Punkten, in Übereinstimmung mit Ergebnissen aus einer Bosonisierungsrechnung [12], überein. Wir finden eine *dimerisierte* Zwischenphase und eine stark-Kopplungs-Phase mit einer *divergierenden elektrischen Suszeptibilität*, obwohl diese Phase ansonsten Eigenschaften eines stark korrelierten Isolators aufweist.

In Kapitel 6 werden die erwähnten zwei Varianten der *adaptiven zeitabhängigen DMRG* vorgestellt und eine Fehleranalyse beider Methoden für beide in dieser Arbeit behandelte Nichtgleichgewichtssituationen vorgestellt.

In Kapitel 7 wird die adaptive t-DMRG angewandt um ein System aus anfangs durch ein Fallenpotential festgehaltenen soft-core Bosonen zu untersuchen, nachdem das Fallenpotential abgeschaltet wird. Die Ergebnisse werden mit exakten Ergebnissen für hard-core Bosonen verglichen [13]. Obwohl die theoretische Behandlung der hard-core Bosonen es erlaubt, sehr grosse Systeme sehr genau zu behandeln, ist die experimentelle Realisierung schwieriger im Vergleich zu den soft-core Bosonen. Daher ist es von Bedeutung für die Experimente, von theoretischer Seite Vorhersagen für die soft-core Bosonen treffen zu können. Ähnlich zu den hard-core Bosonen finden wir, dass sich *kohärente Materiewellen* bilden. Zusätzlich finden wir, dass sich der Wellenvektor durch die Stärke der Wechselwirkung steuern lässt. Dies zeigt, dass es in optischen Gittern möglich ist, einen *Atomlaser* mit einstellbaren Parametern zu realisieren.

In Kapitel 8 wird die Zeitentwicklung stark korrelierter spinloser Fermionen nach einem Quench untersucht, d.h. in unserem Fall nachdem die Stärke der Wechselwirkung zwischen den Teilchen plötzlich geändert wurde. Im Stark-Kopplungs-Limes finden wir, vergleichbar zu den Experimenten mit einem BEC [7], einen “collapse and revival” einer Luttingerflüssigkeit. Die adaptive t-DMRG erlaubt es, die Zeitentwicklung für relativ grosse Systeme über ausreichend lange Zeiträume zu verfolgen, so dass das Relaxationsverhalten untersucht werden kann. Der Ergodenhypothese entsprechend, ist die allgemeine Erwartung, dass das System zu einem thermischen Zustand relaxiert. Wir finden jedoch Relaxation zu einem *nicht-thermischen quasistationären Zustand*. Das untersuchte System ist integrierbar mit Hilfe des Bethe-Ansatzes; eine allgemeine Erwartungshaltung für

klassische Systeme ist, dass ein System *nicht integrabel* sein muss, um zu thermalisieren. Dies wird untersucht, indem das System durch einen zusätzlichen Wechselwirkungsterm nicht-integrabel gemacht wird. Auch in diesem Fall finden wir Relaxation zu einem nicht-thermischen Zustand. Wir finden jedoch, innerhalb der Genauigkeit der Methode, dass für bestimmte Anfangsbedingungen zwei unterschiedliche Anfangszustände mit der selben Energie zum selben quasistationären Zustand relaxieren können, der sich zwar vom thermischen Zustand unterscheidet, ihm aber sehr nahe kommen kann. Wir diskutieren die Möglichkeit, den entstehenden quasistationären Zustand durch ein *verallgemeinertes Gibbs-Boltzmann Ensemble* zu beschreiben.

Chapter 1

Introduction

Recent experiments on optical lattices [5] have made it possible to study properties of quantum many-body systems in equilibrium (see, e.g., Refs. [6, 14]) and in situations out-of-equilibrium. Prominent examples for the latter are the observation of collapse and revival of an initial Bose-Einstein condensate (BEC) [7], the realization of a quantum version of Newton's cradle [8] and the quenching of a ferromagnetic spinor BEC [9]. The experimental investigation of these systems has only become possible due to the unprecedented possibilities of controlling the parameters of the systems allowed by the storage of ultracold atoms in optical dipole traps. In optical lattices, it is exploited that the electric field of a laser beam induces a dipole moment in an atom which, in turn, interacts with the electric field of the laser beam. In this way, a periodic potential building up the optical lattice is obtained by overlapping counter-propagating laser beams. Controlling the parameters of the laser beams leads to a high degree of control of the system; in particular, it is possible to tune the interaction strength between the particles, so that systems can be pushed out of equilibrium in a controlled way.

For large values of the interaction, the systems become strongly correlated and cannot be treated using mean-field like approaches. Although certain models can be solved exactly by means of the *Bethe Ansatz* [15], in general, approximate methods like perturbation theory must be applied. For certain parameter regimes, the validity of such approximate approaches is questionable and their application can lead to erroneous results. Numerical methods are, therefore, of great importance for the investigation of strongly correlated systems. In this thesis, we focus on the so-called *exact diagonalization* techniques (ED) and on the *density matrix renormalization group* method (DMRG), one of the most accurate numerical approaches for treating strongly correlated systems in one spatial dimension. Since the invention of the DMRG by S.R. White in 1992 [1], it has become a standard tool. A multitude of quasi one-dimensional systems has been treated using this method; for an overview we refer to Refs. [2, 3, 4]. In this approach, the ground

state of a system is obtained in an iterative procedure based on an extension of Wilson's numerical renormalization group (NRG) [16]. Instead of working in an efficient basis of energy eigenstates like in the NRG, in the DMRG the system is divided into two parts and an effective basis of eigenvectors of the *reduced density matrix* of one part of the system is considered. The resulting iterative procedure is very efficient, and the method allows for the investigation of ground-state properties of strongly correlated systems with several hundred to several thousand lattice sites. Extensions to calculate dynamical correlation functions and finite temperature properties have been developed in the course of the years [2, 3, 4]. However, these methods are applicable to systems in equilibrium only.

Strongly correlated systems *out of equilibrium* belong to the most challenging problems in theoretical physics. Due to the lack of appropriate analytical as well as numerical methods, only little is known about the non-equilibrium properties of these systems. However, the DMRG has recently been extended to treat *time-dependent* systems in situations out-of-equilibrium, opening up new possibilities for the investigation of their properties. In this thesis, we present two variants of the *adaptive time-dependent DMRG* which make it possible to investigate a variety of quasi one-dimensional systems out of equilibrium with high accuracy. Using these methods, we investigate the emergence of (quasi-)coherent matter waves of *soft-core bosons* on an optical lattice after releasing the particles from an initial trapping potential, as well as the relaxation dynamics of a strongly correlated fermionic system after a quantum quench.

The thesis is organized as follows. In chapter 2, strongly correlated quantum systems are introduced and the *models* relevant for this thesis are presented. The *Luttinger liquid phenomenology*, the concept of *quantum criticality*, and the possible *realization* of such systems on optical lattices is discussed. In Sec. 2.5, situations out-of-equilibrium for strongly correlated systems are discussed, with a focus on the possible *thermalization* of a general quantum many-body system.

In chapters 3 and 4, algorithms for *iterative diagonalization procedures* and the *DMRG* as well as implementation details are presented. An extension of the *Lanczos method* for time-dependent problems is shown to have extremely small errors during the time-evolution, in agreement with an estimate for an upper error bound found by Hochbruck and Lubich [11].

In chapter 5, using the DMRG, susceptibilities and correlation functions of the *ionic Hubbard model* are obtained. The results presented elucidate the quantum critical behavior of this model in one spatial dimension. In particular, we find strong indications for the existence of *two* critical points, in accordance with a scenario found by Fabrizio, Gogolin, and Nersesyan [12] using a bosonization ansatz. At the first critical point, only the charge degrees of freedom become critical while at the second transition point only the spin degrees of freedom are

critical. The intermediate phase is found to have a finite dimerization. The strong coupling regime is a strongly correlated insulator phase, but with a *divergent electric susceptibility*.

In chapter 6, we present two variants of the *adaptive time-dependent DMRG* (adaptive t-DMRG). The first variant is based on the Lanczos time-evolution method introduced in Sec. 3.2. The second approach is based on a Suzuki-Trotter decomposition of the time-evolution operator [10]. Both approaches are compared to each other, and an error analysis is performed for each one.

In chapter 7, we apply the adaptive t-DMRG to treat a system of initially trapped *soft-core bosons* (SCB) and compare to exact results obtained for hard-core bosons (HCB) [13]. Although HCBs can be treated theoretically in an efficient way, it is more difficult to realize them in experiments on optical lattices. Therefore, it is of relevance for the experiments to treat SCBs. This can be done in a very accurate way using the adaptive t-DMRG. We find that, similar to the HCBs, *coherent matter waves* emerge when releasing the trap. Our results show that the wavevector depends on the interaction strength, demonstrating that it is possible to engineer *atom lasers* on optical lattices.

In chapter 8, the time evolution of strongly correlated spinless fermions after a quantum quench is investigated. In the strong coupling limit, *collapse and revival of a Luttinger liquid* state is found, reminiscent of the experimental realization of the collapse and revival of a BEC on an optical lattice [7]. Using the adaptive t-DMRG, it is possible to investigate systems and times large enough so that the relaxation of the system after the quench can be analyzed. We investigate the time evolution of a model which is integrable using the Bethe Ansatz, but which can be easily made non-integrable by adding an additional interaction term. We find relaxation to a *non-thermal quasi-stationary state*, independent of the integrability of the system. However, for certain initial conditions, two initial states with the same energy are found to relax, within the resolution of our method, to the same quasi-stationary state. We discuss the possibility of describing the quasi-stationary state in terms of a *generalized Gibbs-Boltzmann* distribution.

Part I

Numerical Methods for Strongly Correlated Quantum Systems

Chapter 2

Strongly Correlated Quantum Systems

Many problems in condensed matter physics can be described effectively within a single-particle picture [17] or by introducing quasiparticles according to Landau's Fermi liquid theory. However, in systems where interaction leads to strong correlation effects between the system's component parts, mapping to an effective single-particle model can lead to an erroneous description of the system's behavior. In such cases, it is necessary to treat the full many-body problem. However, in the investigation of condensed matter systems, one is often interested in the low-energy properties of a system. For the investigation of these properties numerical methods have been developed which enable us to efficiently treat effective models that describe these low-energy properties.

In this thesis, we treat systems on lattices, i.e., systems composed of N quantum mechanical subsystems, where each subsystem is located on a site j and is described by a (usually finite) number of basis states $|\alpha_j^{(\ell)}\rangle$, $\ell = 1, \dots, s_j$, which depend on the model and may vary from site to site. One often is interested in general properties of the physical models that go beyond their behavior on finite lattices. In these cases, it is necessary to investigate the behavior in particular limits, e.g., by investigating the model's behavior when $N \rightarrow \infty$ (the thermodynamic limit). Insight can also be gained by considering the limit of a continuous quantum field by taking $\ell \rightarrow x/a$, where a is the lattice constant. Here, we restrict ourselves to treat finite lattices, as, e.g., realized in recent experiments on optical lattices [6]. Given the site basis $\{|\alpha_j^{(\ell)}\rangle\}$, a possible *configuration* $|\alpha_1^{(\ell)}, \alpha_2^{(\ell)}, \dots, \alpha_N^{(\ell)}\rangle$ of the total system is given by the direct product of the component basis,

$$|\alpha_1^{(\ell)}, \alpha_2^{(\ell)}, \dots, \alpha_N^{(\ell)}\rangle \equiv |\alpha_1^{(\ell)}\rangle \otimes |\alpha_2^{(\ell)}\rangle \otimes \dots \otimes |\alpha_N^{(\ell)}\rangle. \quad (2.1)$$

After symmetrizing (for bosons) or antisymmetrizing (for fermions) and under

consideration of the correct normalization factor, one thereby obtains the basis states of the many-body system [18]. In the following, we will omit the state index ℓ . The set of all of these states constitutes a complete basis in which the total number of possible combinations and therefore the dimension of the resulting Hamiltonian matrix or state vector is $\prod_{j=1}^N s_j$. This exponentially increasing dimension of the basis of the system is the key problem to overcome when treating quantum many-body systems. In principle, a quantum computer would be needed to provide the full solution of an arbitrary quantum many-body problem [19, 20, 21]. However, a variety of numerical approaches exist to investigate such systems with a high precision on ordinary (or “classical”) computers. A number of different numerical methods for many-body systems have recently become available as parts of an open source project, the ALPS application library (Applications and Libraries for Physics Simulation) [22, 23], in which the author is one of the developers.

The behavior of a quantum mechanical system is, in general, governed by the time-dependent

$$i\hbar \frac{\partial}{\partial t} |\Psi(t)\rangle = H|\Psi(t)\rangle \quad (2.2)$$

or time-independent Schrödinger equation,

$$H|\Psi\rangle = E|\Psi\rangle . \quad (2.3)$$

One approach to treating quantum mechanical systems numerically is to solve (at least partially) the eigenvalue problem, Eq. (2.3), formed by the Hamiltonian for equilibrium situations, or numerically solve the ordinary differential equation (ODE), Eq. (2.2), for systems out of equilibrium. The eigenstates of such systems are many-body states, and the excited states cannot, in general, be mapped to single-particle excitations. In the following, we will focus on exact diagonalization (ED) and on the density matrix renormalization group method (DMRG), numerical methods which work in the many-body basis. These methods have been successfully applied to the investigation of equilibrium properties of strongly interacting quantum systems, especially in one spatial dimension. In this thesis, we develop extensions of these approaches for the treatment of such systems out of equilibrium which enable one to investigate the full time evolution of the systems.

2.1 Models

A regular solid is usually modelled assuming that the atomic nuclei are moving slowly enough so that they can be considered to be fixed on the relevant time

scale for the electronic problem. The simplest fermionic lattice model is the *tight-binding* model [17], which treats electrons as being localized to Wannier orbitals centered on a regular array of sites. Such a model would be appropriate for unfilled d or f orbitals in transition metals, for example. In the simplest case, one restricts the description to only a single band, although multi-band models can also be considered. Due to the finite overlap between nearby orbitals, the particles can “hop” from one site to another, i.e., tunnel between the corresponding Wannier orbitals, with an amplitude t . The mapping of unfilled strongly localized orbitals to the tight-binding model is sketched in Fig. 2.1.

In this thesis, we discuss fermionic as well as bosonic models. Fermionic models are usually considered when describing electronic properties of solids. However, the recent developments in the experimental realization of ultracold atom gases has spurred the theoretical interest in bosonic models since most of the experiments are performed with bosonic atoms.

We start describing the fermionic models. Since the overlap between strongly localized orbitals typically decreases exponentially with separation, in most cases one considers hopping only between nearest-neighbor sites, or at most hopping to next-nearest neighbor sites. The Hamiltonian for the simple tight-binding chain with nearest-neighbor hopping in second quantization is given by

$$H^{\text{tb}} = - \sum_j t_j (c_j^\dagger c_{j+1} + c_{j+1}^\dagger c_j) . \quad (2.4)$$

Throughout this thesis, we will choose units so that $\hbar = 1$. The quantity t_j is the tunneling matrix element between the sites j and $j + 1$ and corresponds to the kinetic energy of the particle “hopping” between these two sites. The operators c_j^\dagger (c_j) create (annihilate) fermions in the subsystem labeled by j , and obey the usual anticommutation relations, $\{c_i^\dagger, c_j\} = \delta_{ij}$ and $\{c_i^\dagger, c_j^\dagger\} = \{c_i, c_j\} = 0$. This model is a basic model and describes free “particles in a box” if fixed boundary conditions are selected (i.e., if the wavefunction is chosen to be zero at the boundaries). Below, we will discuss the formulation of this basic model for bosons, usually referred to as “hard-core bosons”.

It is possible to include the Coulomb interaction, which on a lattice is formulated in terms quadratic in the local particle number operators, $n_i = c_i^\dagger c_i$. Due to screening, usually only the interaction between particles sitting on nearest- or next-nearest-neighbor sites plays a role. If the spin is not relevant, or if it is polarized, e.g., as \uparrow , a simple extension of the tight-binding Hamiltonian, Eq. (2.4), including Coulomb interaction is

$$H^{\text{tV}} = - \sum_j t_j (c_{j+1}^\dagger c_j + c_j^\dagger c_{j+1}) + \sum_j V_j n_j n_{j+1} . \quad (2.5)$$

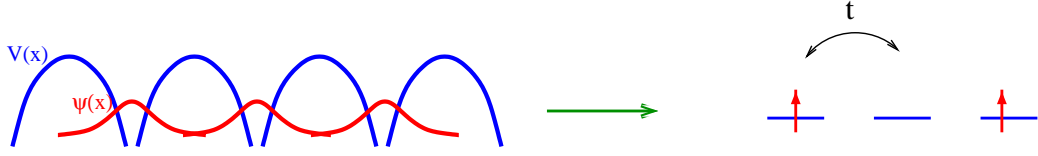


Figure 2.1: Left-hand side: sketch of the pseudo-potential for a chain of atoms and the corresponding localized Wannier orbital centered on the positions of the atoms, which are assumed to be fixed on a regular lattice. Right-hand side: sketch of the effective lattice model.

This model is usually referred to as “interacting spinless fermions” or the “ $t - V$ -model”. Due to the interaction term, strong correlations are present in the system and it is not possible to work in a single-particle basis anymore. However, in one spatial dimension, it is possible to solve this model exactly using the *Bethe Ansatz*; it is one of the few *integrable* quantum many-body systems. In analogy to classical systems, it is expected that integrable quantum systems should possess a time evolution which is qualitatively different from non-integrable systems (see, e.g., Ref. [24]), an issue that will be discussed in detail in Secs. 2.1.1 and 2.5. In chapter 8, a system of spinless fermions that is perturbed from equilibrium by a *quantum quench* is investigated in detail using the methods developed in this thesis. In particular, the question of whether non-integrable quantum systems, in contrast to integrable systems, reach an equilibrium state at a finite temperature is discussed in detail.

When spin is included, Pauli’s exclusion principle allows up to two fermions with opposite spin to occupy a Wannier orbital. The possible states on a site j are then $\{|\alpha_j^{(\ell)}\rangle\} = \{|0_j\rangle, |\uparrow_j\rangle, |\downarrow_j\rangle, |(\uparrow\downarrow)_j\rangle\}$. This is an appropriate site basis for modeling systems with a *local* Coulomb interaction, e.g., a repulsion between electrons localized at the same atom. The simplest model which can be formulated in this spirit is the well known *Hubbard model* (HM),

$$H^{\text{HM}} = -t \sum_{j,\sigma} (c_{j,\sigma}^\dagger c_{j+1,\sigma} + c_{j+1,\sigma}^\dagger c_{j,\sigma}) + U \sum_j n_{j,\uparrow} n_{j,\downarrow}, \quad (2.6)$$

with σ labeling the spin and $n_{j,\sigma} = c_{j,\sigma}^\dagger c_{j,\sigma}$ the local particle number operator. This model is named after John Hubbard, who introduced it in 1963 for modeling electronic correlations in narrow energy bands [25] (it was independently introduced by Gutzwiller [26] and Kanamori [27] at around the same time). It has been used to describe the Mott metal-insulator transition, band magnetism in iron, cobalt and nickel, and attempts have been made to characterize electronic properties of high- T_c superconductors, see Ref. [28] and references therein. For the HM and its variants, the dimension of the Hilbert space grows as 4^N , where N is the number

of lattice sites. Due to screening effects, it is usual to reduce the Coulomb interaction to the on-site term (the *Hubbard term*), or sometimes the nearest-neighbor term $V \sum n_i n_{i+r}$, in which case the model is called the *extended Hubbard model* (EHM). In chapter 5, the transition from a band insulator to a strongly correlated Mott insulator is studied for a variant of the HM with alternating external potential, the so-called *ionic Hubbard model* (IHM). A comprehensive overview of the HM and its physical properties in one spatial dimension is available in Ref. [28], where it is shown that the model is integrable using the Bethe Ansatz. However, its extensions like the EHM and the IHM can no longer be treated with exact analytic approaches. Therefore, it is necessary either to treat these problems using approximate analytical tools such as perturbation theory or using numerical methods, such as the ones described in this thesis.

An important class of models are spin models. If \mathbf{S}_i describes a localized quantum mechanical spin with magnitude $S = 1/2, 1, 3/2, \dots$, the possible states on a site j are $\{|\alpha^{(j)}\rangle\} = \{|-S\rangle, |-S+1\rangle, \dots, |S\rangle\}$, i.e., such models possess $(2S+1)^N$ degrees of freedom. A prominent example is the *Heisenberg Hamiltonian*,

$$H^{\text{Heis}} = \mathbf{J} \sum_{\langle j,m \rangle} \mathbf{S}_j \cdot \mathbf{S}_m. \quad (2.7)$$

The $S = 1/2$ Heisenberg model can be derived as the strong-coupling limit of the Hubbard model ($U/t \rightarrow \infty$) at half filling, i.e., average particle density $\langle n \rangle = 1$. The corresponding antiferromagnetic exchange coupling in second-order perturbation theory (see Fig. 2.2) is $J = 4t^2/U$ [29]. In chapter 5, we use the Heisenberg model for the description of some aspects of the strong-coupling phase of the IHM. In one spatial dimension, the Heisenberg model is solvable using the Bethe Ansatz, for which it was originally introduced by H. Bethe in 1931 [15]. When $J^z \neq J^{xy}$, it is termed the Heisenberg model with XY anisotropy, when $J^x = J^y$ it is referred to as the XXZ-model,

$$H^{\text{XXZ}} = J^z \sum_{\langle j,m \rangle} S_j^z S_m^z + \frac{1}{2} J^{xy} \sum_{\langle j,m \rangle} (S_j^+ S_m^- + S_j^- S_m^+), \quad (2.8)$$

with the usual spin ladder operators S^+, S^- . For $S = 1/2$, using a Jordan-Wigner transformation [30], the spinless fermion Hamiltonian, Eq. (2.5), can be mapped to the XXZ Hamiltonian Eq. (2.8), with $V = J^z$ and $J^{xy} = 2t$, showing that the Hamiltonian Eq. (2.5) is solvable using the Bethe Ansatz.

Recently, it has become possible to realize strongly correlated quantum systems in optical lattices [6]. Although some progress in experiments with ultracold fermions has been reached, in general the experiments are easier when bosonic atoms are utilized, since it is more difficult to cool down fermions due to Pauli

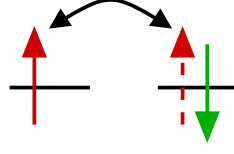


Figure 2.2: The second-order virtual exchange process in the Hubbard model which leads to the antiferromagnetic Heisenberg coupling, see Ref. [29].

blocking. The standard notation for the bosonic version of the Hubbard model is

$$H^{\text{BHM}} = -J \sum_{\langle i,j \rangle} (b_i^\dagger b_j + h.c.) + \frac{U}{2} \sum_i n_i (n_i - 1) , \quad (2.9)$$

with hopping amplitude J between neighboring sites and bosonic annihilation (creation) operators $b_i^{(\dagger)}$ on the lattice site i with the usual commutation relations $[b_i, b_j^\dagger] = \delta_{ij}$ and $[b_i^\dagger, b_j^\dagger] = [b_i, b_j] = 0$. The particle number operator is given by $n_i = b_i^\dagger b_i$. Particles described by this model are usually referred to as *soft-core bosons* (SCB), as there is no restriction to the number of particles on each lattice site. This model is not integrable using the Bethe Ansatz. The phase diagram was obtained in Ref. [31] using approximate analytical methods, and the extension with nearest-neighbor interaction was treated in Ref. [32] using the DMRG. In the limit $U \rightarrow \infty$, only one particle per site is possible. This can be modelled by additionally introducing the restrictions

$$b_i^{\dagger 2} = b_i^2 = 0, \quad \{b_i, b_i^\dagger\} = 1, \quad (2.10)$$

where $\{\cdot, \cdot\}$ denotes the anticommutator of the operators. The resulting model Hamiltonian

$$H^{\text{HCB}} = -J \sum_{\langle i,j \rangle} (b_i^\dagger b_j + b_j^\dagger b_i) \quad (2.11)$$

is usually referred to as the *hard-core boson* (HCB) model. In one spatial dimension, it can be mapped to the tight-binding Hamiltonian Eq. (2.4) using the Jordan-Wigner transformation [30]. Hard-core bosons and free fermions therefore have the same spectrum, but off-diagonal correlation functions behave differently due to the different algebra underlying the creation and annihilation operators. Using the Jordan-Wigner transformation, it is possible to efficiently compute the *exact* time-evolution of HCBs in out-of-equilibrium situations [33] for very large systems for all times of interest. This will be exploited in chapter 6 as a benchmark for analyzing the errors of the time-dependent extensions of the DMRG which are

developed in this thesis.

In Refs. [33, 13, 34], it was found that an initial Fock-state of HCBs evolves into a (quasi-)coherent matter wave. Although it has been possible to realize HCBs on an optical lattice [14], the experiments are rather difficult compared to the realization of SCBs, since this limit is only attainable in elongated traps for large positive three-dimensional scattering lengths, at low densities, or with very strong transversal confinement [35, 36, 37].

It is therefore of experimental relevance to compute a similar out-of-equilibrium situation for the complicated many-body problem with SCBs. Using the time-dependent extensions of the DMRG presented in chapter 6, it is possible to reach system sizes and times large enough to make predictions relevant for experiments. The results are described in detail in chapter 7.

2.1.1 Integrability of Quantum Systems

In contrast to classical systems, as discussed below, the concept of integrability of quantum systems needs to be changed. In this section, we summarize the discussion of the integrability of quantum systems presented in chapter 12 of Ref. [28]. To start with, we recall the definition of an integrable system in classical mechanics, which is provided by *Liouville's theorem* [38].

For N classical point particles whose dynamics is governed by a Hamiltonian $H(\mathbf{p}, \mathbf{q})$, the equations of motion are

$$\dot{\mathbf{p}} = -\frac{\partial H}{\partial \mathbf{q}}, \quad \dot{\mathbf{q}} = \frac{\partial H}{\partial \mathbf{p}}. \quad (2.12)$$

For a conservative system, $H(\mathbf{p}, \mathbf{q})$ is time-independent and thus a constant of the motion. Suppose that in total there are N constants of the motion $I_j(\mathbf{p}, \mathbf{q})$, $j = 1, \dots, N$, with $H(\mathbf{p}, \mathbf{q})$ among the $I_j(\mathbf{p}, \mathbf{q})$, and whose Poisson-brackets $\{\cdot, \cdot\}_P$ vanish,

$$\{I_l, I_m\}_P = 0. \quad (2.13)$$

Then, Liouville's theorem states that the equations of motion (2.12) are solvable by "quadrature", i.e., by solving the resulting integrals of motion. This is due to the fact that Eq. (2.13) allows us to construct a canonical transformation which leads to trivial equations of motion in the new action-angle variables. No further input for obtaining the dynamics of the system is needed.

One often considers integrable systems to possess a *regular* dynamics, whereas non-integrable systems are expected to be *chaotic*. This follows from the lack of constraints which allows the system to access every possible state with the same energy during the time evolution, while the trajectories of integrable systems are

restricted to (quasi-)periodic motion on so called “invariant tori” in phase space, see, e.g., Ref. [24]. As discussed in further detail in Sec. 2.5.1, non-integrable systems are assumed to end up in a state whose time average is equivalent to a statistical average at a finite temperature.

For quantum systems, no concept of integrability exists which is as general as Liouville’s theorem. If, by analogy, the same discussion as above is extended by simply replacing the Poisson brackets with commutators, there is no way to obtain the spectrum and eigenfunctions of the Hamiltonian operator \hat{H} – the construction of action-angle variables is not easily translated into quantum mechanics. A more general approach to find and solve integrable systems is found in the context of the Bethe Ansatz approach, whose general form is the quantum inverse scattering method. In this algebraic approach, the crucial prerequisite is the validity of the *Yang-Baxter equation*, see, e.g., chapter 12 of Ref. [28]. In contrast to classical systems, it is generally unknown if the dynamics of an integrable quantum many-body system should be qualitatively different from that of a non-integrable one. However, in analogy to the expectation for classical systems, non-integrable quantum systems are widely believed to thermalize, while integrable ones are expected not to thermalize. Thermalization is discussed in more detail in Sec. 2.5.1. In chapter 8, we discuss in detail the relaxation of an integrable quantum many-body system and a non-integrable variant of the same model, and compare the emergent quasi-stationary state with a state at a finite temperature.

2.2 One dimensional systems: Luttinger Liquids

It is well known that the low-energy properties of many metals are well described within Landau’s Fermi liquid theory [39, 40, 41, 18], whose key feature is the introduction of *quasiparticles*, i.e., the excitations of the interacting system are described by the same set of quantum numbers as the ones of the non-interacting system. These quasiparticles manifest themselves as peaks of finite width in the system’s Green function, i.e., they have only a finite lifetime. The jump in the momentum distribution function $\langle n_k \rangle$ of free fermions at temperature $T = 0$ at the Fermi momentum k_F is “weakened”, and is determined by the quasiparticle weight Z , with $0 < Z < 1$. However, in one dimension, Fermi liquid theory does not apply at all and is replaced by the *Luttinger liquid* (LL) concept. In this section, we follow the presentation in Refs. [42, 43]. We concentrate on the properties relevant for the discussion of the results presented in this thesis and therefore omit many interesting aspects of this peculiar class of quantum liquids.

The reason for the invalidity of the Fermi-liquid description in one spatial dimension is the breakdown of perturbation theory. The quasiparticle poles in the spectral function disappear and, therefore, no Fermi surface is found in $\langle n_k \rangle$. One

finds instead a *power-law* dependence for values of k asymptotically close to k_F ,

$$\langle n_k \rangle - \frac{1}{2} \sim |k - k_F|^\alpha \text{sign}(k_F - k), \quad (2.14)$$

with $\alpha < 1$ depending on the interaction strength. The jump at the Fermi surface is replaced by a power-law singularity at k_F . Formally, this is equivalent to a quasi-particle weight $Z = 0$, i.e., it is, in contrast to the Fermi liquid picture, not possible to ascribe a single-particle character to the excitations; instead, the excitations are *collective* ones. This form of the momentum distribution function is one of the properties of the *Tomonaga-Luttinger model* (TL) [44, 45],

$$\begin{aligned} H^{\text{TL}} &= \frac{2\pi\hbar}{L} \sum_{n>0} n \left\{ \left(v_F + \frac{g_4(k_n)}{2\pi\hbar} \right) (b_n^\dagger b_n + b_{-n}^\dagger b_{-n}) \right. \\ &\quad \left. + \frac{g_2(k_n)}{2\pi\hbar} (b_n^\dagger b_{-n}^\dagger + b_{-n} b_n) \right\} + \frac{\hbar\pi}{2L} \{ v_N \tilde{N}^2 + v_J \tilde{J}^2 \}. \end{aligned} \quad (2.15)$$

Here, L is the length of the system, v_F is the Fermi velocity, $g_2(k_n)$ and $g_4(k_n)$ are interaction parameters for “forward scattering” processes of particles in the vicinity of $\pm k_F$ with small momentum transfers. (“Umklapp” and “Backscattering” processes with parameters $g_1(k_n)$ and $g_4(k_n)$, respectively, are neglected in the TL model). Furthermore, $v_N = v_F + (g_4(0) + g_2(0))/2\pi\hbar$, $v_J = v_F + (g_4(0) - g_2(0))/2\pi\hbar$, \tilde{N} is the total particle number operator, and \tilde{J} is the “current operator”. A more general model including spin and Umklapp as well as Backscattering processes of particles is the so-called “g-ology” model [46, 47], which we do not discuss here. A renormalization group (RG) study of this model [46] shows that, for repulsive interactions, a fixed-point Hamiltonian of the TL-type is obtained, unless the metallic state is destroyed by the opening of a gap (as, e.g., for the Hubbard model at half filling [47]). This led Haldane to propose the concept of Luttinger liquids as a replacement for Fermi liquid theory for fermions in one spatial dimension [48, 49]. Note that, although we are dealing with fermions, the TL model, Eq. (2.15), is formulated in terms of *bosonic* operators $b_n^{(\dagger)}$. This is obtained when the TL model is derived starting from a general form of the interaction term,

$$\hat{V} = \frac{1}{2L} \sum_{n \neq 0} \tilde{v}(k_n) \hat{\rho}_n \hat{\rho}_{-n} + \frac{1}{2L} N^2 \tilde{v}(0), \quad (2.16)$$

with the Fourier components of the operator of the density $\hat{\rho}_n = \int dx \hat{\rho}(x) e^{-ik_n x}$. Tomonaga’s idea was to restrict himself to excitations with $|k_n| \ll k_F$, so that he could work with a *linearized spectrum* around the Fermi points, and then to split $\hat{\rho}_n$ into operators for “right moving” particles ($\hat{\rho}_{n,+}$ with $k \approx k_F$), and “left

moving” particles ($\hat{\rho}_{n,-}$ with $k \approx -k_F$) with particle velocities $\pm v_F$, respectively. If we restrict ourselves to the *low energy* sector and introduce

$$b_n \equiv \frac{1}{\sqrt{|n|}} \begin{cases} \hat{\rho}_{n,+} & \text{for } n > 0 \\ \hat{\rho}_{n,-} & \text{for } n < 0 \end{cases}, \quad (2.17)$$

we find that the b_n obey the usual bosonic commutation relations.

It is possible to extend the boson operators defined in Eq. (2.17) to include spin. It turns out that then the TL-Hamiltonian retains its form, but separates into a pure *charge* and a pure *spin* component,

$$H^{\text{TL, spinfull}} = H^{\text{TL, charge}} + H^{\text{TL, spin}}. \quad (2.18)$$

One can show that $[H^{\text{TL, charge}}, H^{\text{TL, spin}}] = 0$, i.e., charge and spin excitations are completely *independent*. This is the celebrated *spin-charge separation*. The elementary excitations are *bosonic collective modes* called *spinons* and *holons* for spin or charge excitations, respectively. These excitations are seen as power-law divergences in the one-particle spectral function [50, 51]. In general, spinon and holon excitations disperse with different velocities; therefore, it is, in principle, possible to observe them by calculating the system’s full time evolution after an electron is added. Using the time-dependent DMRG, this scenario has been investigated for the Hubbard model. As expected, independent spin and charge responses to the perturbation are obtained [52].

An experimental verification of LL behavior is difficult. The main difficulty lies in the fact that LL behavior is only to be expected for *strictly* one-dimensional systems at very low energies – i.e., already a small coupling to the environment might destroy the LL behavior. However, there are several candidates showing behavior which is very close to the predictions of the LL concept. The perhaps most promising experiments deal with electrons at the edges of a two-dimensional fractional quantum Hall system, describable by a so-called *chiral Luttinger liquid* [53]. The tunneling density of states found in the tunneling current-voltage characteristics shows power-laws of “extraordinary quality” [42, 54]. Another important class of systems are artificial quantum wires, as realized, e.g., in semiconductor heterostructures, on surface substrates, or as carbon nanotubes. Highly anisotropic quasi-one-dimensional conductors, like, e.g., the Bechgaard salts, are also candidates for LL behavior. Recently, in ARPES experiments on the quasi-one-dimensional organic conductor TTF-TCNQ (*tetrathiafulvalene tetracyanoquinodimethane*), significant differences from Fermi liquid theory and predictions from conventional electronic structure calculations have been found [55, 56]. The spectral function obtained in the experiments can be mapped onto separated spin and charge excitations of the one-dimensional Hubbard model away from half-

filling. The spectral function obtained by Benthien *et. al* [57, 58] using the dynamical DMRG shows very good agreement with the experimental data and reveals that, in this material, the elementary excitations are indeed spinons and holons. This is one of the strongest experimentally observed signatures of spin-charge separation and therefore of possible LL behavior.

Examples for fermionic lattice models with interaction showing Luttinger liquid behavior are the Hubbard model, Eq. (2.6), away from half filling, and the $t - V$ -model, Eq. (2.5), which, at half filling has a Luttinger liquid phase for $V < 2t$. In general, in a Luttinger liquid consisting of spinless particles, one finds that correlation functions can be parameterized by two constants, which depend only from the interaction strength and the Fermi velocity:

$$K = \left(\frac{1 + g_4/(2\pi v_F) - g_2/(2\pi v_F)}{1 + g_4/(2\pi v_F) + g_2/(2\pi v_F)} \right)^{1/2} \quad (2.19)$$

$$u = v_F \left[(1 + g_4/(2\pi v_F))^2 - (g_2/(2\pi v_F))^2 \right]^{1/2} . \quad (2.20)$$

Here, K is a dimensionless parameter, and u has the dimensions of a velocity. Note that, quite generally, for attractive interaction $g_2/(\pi v_F) < 0$ and $K > 1$, while for repulsive interaction $g_2/(\pi v_F) > 0$ and $K < 1$. In the spinfull case, it is possible to introduce similar, dimensionless parameters $K_{\rho, \sigma}$ and $u_{\rho, \sigma}$ for the charge (ρ) and spin (σ) degrees of freedom, respectively. Here we focus on the spinless case. For the long-distance behavior of the density-density correlation function one obtains (for details see [43])

$$\langle \hat{n}_i \hat{n}_j \rangle \sim \frac{\cos(2k_F|i - j|)}{|i - j|^{2K}} , \quad (2.21)$$

i.e., a power-law decay with an exponent that depends on the interaction strength and on the Fermi velocity v_F only. For the momentum distribution function one finds

$$\langle \hat{n}_k \rangle \sim |k - k_F|^{(K + \frac{1}{K} - 2)/2} \quad (2.22)$$

when $k \approx k_F$. The metallic behavior can be seen in the finite compressibility, which is found to be

$$\kappa = \frac{\partial n}{\partial \mu} = \frac{K}{u\pi} , \quad (2.23)$$

with the chemical potential μ .

In chapter 8, the time evolution of a Luttinger liquid state in a system of spinless fermions given by the Hamiltonian Eq. (2.5) on a *finite* lattice is investigated. Thus, finite-size effects are found in the correlation functions. In particular, a jump is visible in $\langle n_k \rangle$ at k_F . This jump does *not* signal a finite quasiparticle weight, but is rather due to the finite resolution when calculating $\langle n_k \rangle$ as the Fourier transform of the one-particle density matrix. Indeed, the power-law behavior can only be

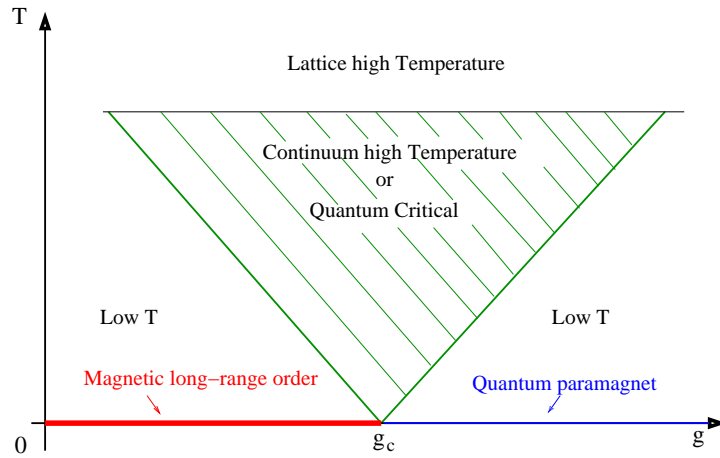


Figure 2.3: Phase diagram of the quantum Ising model with a transverse magnetic field whose strength is proportional to g . Quantum criticality is obtained at $T = 0$ by varying g .

seen for values of k asymptotically close to k_F ; that is, system sizes of thousands of lattice sites would be necessary to obtain the necessary resolution. However, we will see that, under certain circumstances, the initial $\langle n_k \rangle$ for the finite system is restored to a very high precision, showing that one can, indeed, obtain collapse and revival of the initial Luttinger liquid state.

2.3 Quantum Criticality

Phase transitions in classical statistical mechanics and thermodynamics are supported by thermodynamic fluctuations. In quantum systems at *zero temperature* it is also possible to obtain phase transitions which are, however, supported by *quantum fluctuations* alone. These transitions can be obtained by changing the system's *intrinsic* parameters, such as the value of the on-site Coulomb interaction U in the Hubbard model, Eq. (2.6).

The basic model used to introduce and discuss quantum criticality is the one-dimensional quantum Ising model in a transverse magnetic field [59]. The phase diagram of the system is sketched in Fig. 2.3. It is possible to map the one-dimensional quantum model to the classical two-dimensional model [59], hence, the model's quantum critical behavior belongs to the *same* universality class as the two-dimensional classical Ising model.

Similar to classical phase transitions, it is possible to identify *first-order* quantum phase transitions which are due to a level crossing in the ground state when

moving through the critical point, *second-order* transitions with “order parameters” that exhibit power-law behavior with characteristic *critical exponents* close to the critical point, and *infinite order* (or Kosterlitz-Thouless, KT-type) phase transitions with exponential change in a characteristic quantity (e.g., exponential closing of a gap). In order to investigate quantum criticality using numerical approaches, excitation gaps, order parameters, and their susceptibilities are calculated for finite system size L and extrapolated to the thermodynamic limit, i.e., the system size is extrapolated, $L \rightarrow \infty$, while the filling $N/L = \text{const.}$ with N the particle number for the system with size L . As in classical systems, *universal* behavior is found. In Tab. 2.1, the critical behavior of some observables and the corresponding critical exponents for the universality class of the classical 2d Ising model are listed, which in chapter 5 is discussed as the possible universality class at one of the critical points in the phase diagram of the ionic Hubbard model.

The critical exponents are connected via hyperscaling relations [60],

$$\alpha + 2\beta + \gamma \geq 2 \quad (2.24)$$

$$\alpha + \beta(1 + \delta) \geq 2 \quad (2.25)$$

$$\gamma \leq (2 - \eta)\nu \quad (2.26)$$

$$d\nu \geq 2 - \alpha \quad (2.27)$$

$$\gamma \geq \beta(\delta - 1), \quad (2.28)$$

where δ is an additional exponent determining the behavior of the critical isotherm in the classical 2d Ising model. Indeed, one finds by inserting the values for the critical exponents listed in Tab. 2.1 (and in addition with $\delta = 15$), that for the Ising universality class the scaling relations Eqs. (2.24) - (2.28) hold as equalities. It is possible to obtain ν by directly calculating the correlation length [61, 62]. For quantum systems, the *dynamical critical exponent* z influences the critical behavior of the associated gap; for a second-order transition,

$$\Delta \sim |g - g_c|^{z\nu}. \quad (2.29)$$

Thus, the scales of the energetic excitations (i.e., time-scales) and of the characteristic length in the system are related by $\xi \sim \Delta^z$; if $z = 1$, space and time are treated on the same footing, as in relativistic invariant theories. In these cases, ν can be determined by calculating the relevant gap around the critical point. Using the DMRG, this is usually much easier than direct calculation of the correlation length ξ . Note that for a KT-type transition, z is assumed to be one; the gap opens like

$$\Delta \sim e^{\frac{A}{(g-g_c)^\sigma}}, \quad (2.30)$$

i.e., it is characterized by some constant A and some exponent σ .

Observable	behavior at g_c	value for the Ising universality class
Specific heat	$C \sim g - g_c ^{-\alpha}$	$\alpha = 0$
Magnetization	$M \sim (g_c - g)^\beta$	$\beta = 1/8$
Susceptibility	$\chi \sim g - g_c ^{-\gamma}$	$\gamma = 7/4$
Correlation length	$\xi \sim g - g_c ^{-\nu}$	$\nu = 1$
Correlation function	$G(r) \sim 1/r^{d-2+\eta}$	$\eta = 1/4$

Table 2.1: Critical exponents and their values for the Ising universality class. [60].

The susceptibility associated with an order parameter \hat{O} and the corresponding external field h is given by

$$\chi_{\hat{O}} = \left. \frac{\partial \langle \hat{O} \rangle(h)}{\partial h} \right|_{h=0} \quad (2.31)$$

at zero temperature.

Relying on the *hyperscaling hypothesis*, a scaling analysis can be performed. In this approach, the ground-state energy of a finite system of size L in an external field h has a regular component E_0^{reg} independent of h and a component E_0^{sing} with singular behavior at g_c [61, 63],

$$E_0(g, h, L) = E_0^{\text{sing}}(g, h, L) + E_0^{\text{reg}}(g, L). \quad (2.32)$$

Assuming that $E_0^{\text{sing}}(g, h, L)$ is a homogeneous function, one can rewrite it as

$$\frac{E_0^{\text{sing}}(g, h, L)}{L^d} = L^{-(d+z)} Y(c_1 g^\nu L, c_2 h L^{1+z}), \quad (2.33)$$

with a universal, homogeneous function Y and some constants c_1, c_2 . The susceptibility for the field h at temperature $T = 0$ is obtained as $\chi_h = \frac{\partial^2 E_0}{\partial h^2}$, which is, due to the Hellman-Feynman theorem [64], equivalent to Eq. (2.31). Taking into account the scaling relations, Eqs. (2.24) - (2.28), for the Ising universality class lead to the general scaling form

$$\chi_h(g, L) = L^{2-\eta} \tilde{\chi}(L/\xi), \quad (2.34)$$

where $\tilde{\chi}$ is a universal function. This expression, in conjunction with Eq. (2.31), is used in chapter 5 to analyze the critical exponents of the ionic Hubbard model.

As we have seen in the previous section, in one spatial dimension, spin and charge degrees of freedom are decoupled. Therefore, in principle, it is possible to observe different critical behavior in the two sectors. A prominent example is the phase diagram of the repulsive Hubbard model at half filling, where spin excitations remain *gapless* for all values of the interaction, while an infinitesimal

value of the on-site repulsion U already leads to the opening of a charge gap. In chapter 5, the phase diagram of the ionic Hubbard model at half filling is shown to have two critical points – at the first one only the charge degrees of freedom become critical, while at the second one only the spin sector is affected.

Recently, the concept of quantum phase transitions has been extended to systems in a trap, as often encountered in experiments on optical lattices. In these *inhomogeneous* systems, Rigol *et al.* [33, 65, 66, 67] have investigated local observables, such as the *local compressibility*, which they define as

$$\kappa_i^\ell = \sum_{|j| \leq \ell(U)} \left(\langle \hat{n}_i \hat{n}_{i+j} \rangle - \langle \hat{n}_i \rangle \langle \hat{n}_{i+j} \rangle \right), \quad (2.35)$$

where ℓ is estimated by the correlation length of the correlation function in the unconfined system. For a one-dimensional fermionic Hubbard model in a trap, critical behavior *and* universality are obtained when entering Mott-insulating regions of the trapped system. Introducing an appropriate scaling form for the characteristic density, an $L \rightarrow \infty$ extrapolation is possible, and a *generic* phase diagram is obtained, with this behavior referred to as *local quantum criticality*. In chapter 8, we will discuss the use of Eq. (2.35) for characterizing the phases of a system out of equilibrium.

2.4 Experimental Realization in Optical Lattices

Cold atoms in optical lattices currently constitute one of the most promising ways to investigate quantum many-particle systems. The optical lattices can be considered to be stable, artificial crystals of light obtained by creating arrays of optical microtraps using interference of laser beams. The realization of these experimental setups has opened new control possibilities for many-body systems, making it possible to realize structures which are difficult or impossible to obtain in condensed-matter systems. The control possibilities are so pronounced that, in principle, quantum many-body Hamiltonians can be “implemented” in the experiment *at will*, so that the experiments are sometimes named “quantum simulator”^{*}.

The perhaps most notable realization of a strongly correlated quantum system on an optical lattice is the creation of a Mott insulator, i.e., one of the paradigms of strongly correlated quantum systems [6, 68]. Remarkably, this was achieved with bosonic atoms and not with fermions, which is rather unusual considering that one more frequently encounters electronic systems in condensed matter physics.

^{*}Not to be confused with a “quantum computer” – the experimental realization of a particular quantum-mechanical model situation does not yet enable one to perform complicated calculations, like, e.g., integer factorizations.

These systems are describable by the Bose Hubbard model, Eq. (2.9). Even the limit of very strong interactions, where the bosons can be considered to be impenetrable particles (hard-core bosons, Eq. (2.11), or a Tonks-Girardeau gas [69]) could be reached experimentally [14, 70]. More recently, controlled studies of the evolution of Bose gases prepared or pushed out of equilibrium have been performed, like the collapse and revival of an initial Bose condensate [7], or the realization of a “quantum” version of Newton’s cradle [8].

The basic technique for storing neutral atoms is the use of *optical dipole traps* which exploit the interaction between an induced dipole moment in an atom and an external electric field. In optical lattices, the external electric field is provided by the oscillating electric light field of the laser beam. This field induces an oscillating dipole moment in the atom and *at the same time* interacts with this dipole moment. In this way, the trapping potential [71, 5]

$$V_{\text{dip}}(\mathbf{r}) \sim \alpha(\omega_L) |\mathbf{E}(\mathbf{r})|^2 \quad (2.36)$$

is obtained, where $\alpha(\omega_L)$ is the polarizability of the atom and $|\mathbf{E}(\mathbf{r})|^2 \sim I(\mathbf{r})$ is the intensity of the laser light field induced by its electric field amplitude at position \mathbf{r} . In order to avoid spontaneous emission effects from resonant excitations and to obtain a purely conservative potential, the laser light is usually tuned far away from atomic resonance frequencies. For a frequency of the laser light ω_L smaller than the atomic resonance frequency ω_0 , one obtains an attractive potential, while for $\omega_L > \omega_0$ the potential is repulsive [5]. The periodic potential building the optical lattice is now simply obtained by overlapping two counter-propagating laser beams, leading to a standing wave with period $\lambda_L/2$ which becomes the lattice constant of the system. Thus, in principle, it is possible to obtain periodic potentials in arbitrary spatial dimensions $d \leq 3$. In this way, the geometry and the strength of the local potential are under complete control, and it is therefore also possible to push the system out of equilibrium by changing the properties of the optical lattice. Note that changing the strength of the trapping potential can be considered as a change in the tunneling probability J between two neighboring lattice sites. Thus, when working in a regime which can be modeled by the Bose Hubbard model, Eq. (2.9), changing the intensity of the laser beams is equivalent to changing the ratio U/J . However, due to the Gaussian profile of the laser beams, an additional harmonic confinement, which usually is quite weak and is expected to be negligible, arises. Nevertheless, the atoms are trapped in an inhomogeneous environment – when comparing experiments to theoretical results, care has to be taken.

The possibility to realizing out-of-equilibrium situations of strongly correlated systems on optical lattices has spurred theoretical interest in this field, our work is connected in various ways to these experiments. Inspired by the observation of

collapse and revival of a Bose Einstein condensate (BEC) on an optical lattice [7], we investigate in chapter 8 the possibility of obtaining the collapse and revival of a *Luttinger liquid* in a system of interacting *fermions*. In chapter 7, the possibility of obtaining an *atom laser* on an optical lattice using coherent matter waves of soft-core bosons is discussed. In the next section and in chapter 8 we discuss in detail the possible *thermalization* of a strongly correlated quantum system, which has been recently investigated experimentally on optical lattices for an integrable system of interacting bosons [8].

2.5 Strongly Correlated Systems out of Equilibrium

Only little is known about strongly correlated quantum systems out of equilibrium. Both the experimental as well as the theoretical investigation of the time evolution of the systems is difficult and has been hampered by the complexity of the possible situations. In this thesis, we focus on the simpler set of problems where the Hamiltonian operator is time-independent, although, with the methods developed, it is possible to also treat problems with a time-dependent Hamiltonian operator. We treat isolated systems and compute the time evolution of a pure initial state governed by the time-dependent Schrödinger equation, Eq. (2.2), i.e., at all instants of time the system remains in a pure state. We introduce three categories of non-equilibrium situations with a time-independent Hamiltonian operator, where the system is pushed out of equilibrium by some “sudden” change, and which correspond to different kinds of possible experiments:

- A. The initial state is *constructed* by applying *external fields* which are switched off at the beginning of the time evolution. In this way, the system can be prepared in an initial state with the desired properties, e.g., particles in a trap.
- B. *Quantum quench* situations, where *intrinsic parameters* of the system, e.g., the interaction strength, undergo a sudden change. This can be realized in experiments on optical lattices by suddenly changing the properties of the optical lattice.
- C. Apply a *bias* to the initial state. The resulting non-equilibrium steady state carries a permanent current. Such situations are realized in experiments, e.g., for quantum dot systems coupled to leads at different voltages.

Using the methods developed in this thesis, it is possible to treat problems of each of the three categories. In this work, we discuss out-of-equilibrium situations with

an initial state prepared by external fields in chapter 7, and a quantum quench situation in chapter 8.

The formal solution of the time-dependent Schrödinger equation, Eq. (2.2), with time-independent Hamiltonian H is

$$|\psi(t)\rangle = U|\psi_0\rangle, \quad (2.37)$$

where $U = \exp(-iHt)$ is the time evolution operator and $|\psi_0\rangle$ the initial state. Due to the oscillatory character of U , for systems with a small number of degrees of freedom, recurrences of the initial state on experimentally relevant time scales are expected. However, the large number of degrees of freedom in strongly correlated systems leads to *dephasing* and makes the time scales for such recurrences extremely large, so that, for experimentally relevant time scales, the systems can be considered to show *no* recurrence of the initial state. Independent from the recurrences, the systems can show “collapse and revival” of the initial state on short time scales, as, e.g., observed in Ref. [7]. In general, the amplitude decreases in time, so that a quasi-stationary state with oscillations of very small amplitude (compared to the oscillations at the beginning of the time evolution) around a “quasi-stationary state” is obtained. This phenomenon we refer to as “relaxation” to a quasi-stationary state, although the systems are not coupled to an external bath. However, for a general situation, it is unclear on which time scales this might happen, and how the eventually emerging “steady state” could be characterized.

2.5.1 Thermalization

A basic assumption in classical statistical mechanics is that *closed* systems pushed out of equilibrium can be described by a finite temperature state after long enough times. This expectation is due to Boltzmann’s *ergodic hypothesis* introduced in 1871, according to which, roughly speaking, the system will pass close to nearly all the states compatible with conservation of energy during the time evolution. (For a nice introduction to ergodic theory we refer to Ref. [72]). In this way, when taking the time average over times long enough, every state of the system with the same energy has been passed by with (nearly) the same probability, so that the situation can be described by a microcanonical ensemble. Thus, the time average of observables should be equal to a thermal expectation value in a canonical ensemble. However, this expectation is only valid if the portion of the phase space compatible to energy conservation is *completely* covered by the dynamics. If the system is integrable, the motion is restricted to parts of the phase space due to the constraints of the motion – the system can not thermalize. However, for

non-integrable models, the general expectation is that the complete phase space is covered by the dynamics, such that thermalization should occur.

The first numerical investigation of thermalization in a classical non-integrable system was done by Fermi, Pasta, and Ulam (FPU) in the 1950s who investigated the dynamics of a vibrating string with a non-linear term. According to the ergodic hypothesis, they expected the system to thermalize. However, they did not find relaxation to a thermal state; instead, they obtained a complicated quasi-periodic behavior. This numerical experiment inspired theoretical research and spurred the development of *chaos theory*. For an introduction to this theory we refer to Ref. [24]. Usually, the (quasi-)periodic motion found for integrable systems is referred to as “regular” dynamics. The motion is restricted due to constraints to so-called “invariant tori” in phase space (the notion “quasi”-periodic is due to the fact that trajectories on such topologies may not close). In contrast, non-integrable systems are considered to possess “chaotic” dynamics, because the complete phase space may be covered by the evolution [24] – therefore, FPU’s finding is indeed surprising. However, it was shown by Kolmogorov, Arnold, and Moser (KAM) that, under certain circumstances, adding a “small” perturbation to a system with regular dynamics does not automatically take the dynamics out of an invariant torus [24]. Thus, although non-integrable, the system remains non-ergodic. However, a perturbation “strong enough” can lead to a chaotic dynamic and hence to ergodicity, so that such systems are considered to relax to a thermal state. Note that ergodicity has been found to be *not* sufficient for a classical system to thermalize – in addition, it has to be “mixing”, as discussed in Ref. [72], i.e., the phase space has to be covered “completely” and reversible behavior should be impossible (like, e.g., the demixing of milk and coffee in a cup of cappuccino). However, chaotic systems are usually considered to be mixing [73], so that for classical chaotic many-body systems, relaxation to a thermal state should indeed take place.

In analogy to this discussion for classical systems, a qualitative difference between the time evolution and the emerging quasi-stationary state for integrable and non-integrable quantum many-body systems has been widely considered. However, as discussed in Sec. 2.1.1, the concept of integrability of a quantum system is different from the one for classical systems. Nevertheless, for some systems, in *quantum chaos* [24, 74], a distinction between quantum systems with a regular and a chaotic phase space is obtained by considering the dynamics of the system when taking the *classical limit* (i.e., formally taking the limit $\hbar \rightarrow 0$) [74]. For strongly correlated quantum many-body systems, this classical limit, in general, does not exist [75]. Therefore, characterization of the dynamics of strongly correlated systems in terms of regular or chaotic is not possible. Recently, however, for the one-dimensional Bose-Hubbard model in a certain parameter regime, the spectrum was found to obey the *Wigner-Dyson* statistics [75], which is a signature

of quantum chaotic behavior [74], indicating that concepts from quantum chaos might be helpful for characterizing the dynamics of strongly correlated systems. However, it is difficult to gain insight about possible differences of the dynamics of integrable or non-integrable quantum many-body systems from these considerations.

In recent work, Berges *et al.* have investigated the non-equilibrium dynamics of quantum fields in a low-energy quark-meson model [76]. Choosing two different initial states with the same energy density, the authors find that both states relax to the same quasi-stationary state on an *intermediate* time scale, while on a much larger time scale the quantities further relax to thermal expectation values. This phenomenon is referred to as *prethermalization*. Also, other authors have given voice to the expectation of a thermal finite state when a strongly correlated quantum system is non-integrable [77, 78]. However, it remains quite unclear if this relaxation behavior is only due to the non-integrability of the systems. In order to clarify this issue, we now consider the general form of a time average for an observable after a quantum quench and discuss the possible connection of the time average of observables to generalized statistical operators.

The time evolution of the expectation value of an observable O for systems with time-independent Hamiltonian H can be written as

$$\begin{aligned}\langle O \rangle(t) &= \langle \psi_0 | e^{iHt} O e^{-iHt} | \psi_0 \rangle \\ &= \sum_n |\langle n | \psi_0 \rangle|^2 \langle n | O | n \rangle \\ &\quad + \sum_{m \neq n} \langle m | \psi_0 \rangle \langle \psi_0 | n \rangle e^{-it(E_m - E_n)} \langle n | O | m \rangle,\end{aligned}\quad (2.38)$$

with initial state $|\psi_0\rangle$ and $|m\rangle, |n\rangle$ the eigenstates of H with energies E_m, E_n . In the following, we use the abbreviation $\varrho_n \equiv |\langle n | \psi_0 \rangle|^2$. If no degeneracies in the spectrum are present, i.e., if $E_m \neq E_n \forall m, n$, the time-independent part of the observable is

$$\langle O \rangle_{\text{static}} = \sum_n \varrho_n \langle n | O | n \rangle,\quad (2.39)$$

an expression which can be interpreted as a trace over the product of a statistical operator with the observable

$$\sum_n \varrho_n \langle n | O | n \rangle \equiv \text{Tr}(\varrho O),\quad (2.40)$$

with unknown statistical operator ϱ . In the general case with some degenerate energy levels, i.e., $E_m = E_n$ for some m, n , this can be easily generalized. If $E_m = E_n$, the corresponding term loses its time dependence, and the term contributes to

the time-independent part,

$$\begin{aligned} \langle O \rangle_{\text{static, degeneracies}} &= \sum_n \varrho_n \langle n | O | n \rangle \\ &+ \sum_{\substack{m>n \\ E_m=E_n}} (\langle m | \psi_0 \rangle \langle \psi_0 | n \rangle \langle n | O | m \rangle + c.c.) . \end{aligned} \quad (2.41)$$

Transforming to the basis $|\alpha\rangle$ in which the observable O is diagonal, we obtain

$$\begin{aligned} \langle O \rangle_{\text{static, degeneracies}} &= \\ &= \sum_{\alpha} \left(\sum_n \varrho_n |\langle n | \alpha \rangle|^2 + \sum_{\substack{m>n \\ E_m=E_n}} (\langle m | \psi_0 \rangle \langle \psi_0 | n \rangle \langle n | \alpha \rangle \langle \alpha | m \rangle + c.c.) \right) \langle \alpha | O | \alpha \rangle \quad (2.42) \\ &\equiv \sum_{\alpha} \varrho'_{\alpha} \langle \alpha | O | \alpha \rangle \equiv \text{Tr}(\varrho' O). \end{aligned} \quad (2.43)$$

Thus, the static part of the observables can *always* be identified with a statistical average with, however, an unknown statistical operator. Note that in the case without degeneracies, the static part of the expectation value of the observable is completely determined by the initial state and the trace is formally taken with the same statistical operator for *every* observable, while in the case of a degenerate spectrum, the statistical operator would depend on the eigenbasis $|\alpha\rangle$ of the observable.

Now we consider the time-dependent part of Eq. (2.38). After relaxation at time t_0 , $\langle O \rangle(t)$ starts to oscillate around a time average which is defined by

$$\overline{\langle O \rangle} := \lim_{T \rightarrow \infty} \frac{1}{T} \int_{t_0}^{t_0+T} dt \langle O \rangle(t) . \quad (2.44)$$

The time-dependent part in Eq. (2.38) is a sum of sinusoidal functions. Thus, taking the time average, Eq. (2.44), the contributions of the oscillatory part of $\langle O \rangle(t)$ cancel out and the time average is given by $\langle O \rangle_{\text{static}}$ [79]. This is confirmed by numerical calculations which we present in chapter 8. Therefore, the time average of observables can indeed be identified with the static part of the observable, and, hence, with an unknown statistical operator. At this point we can see that thermalization only takes place if

$$\varrho_n = \frac{1}{Z} e^{-\beta E_n} , \quad (2.45)$$

where $Z = \sum_n \exp(-\beta E_n)$ is the partition function and β is the inverse temper-

ature. This, in general, will not be the case – quantum systems after quenches do, therefore, *not* thermalize, independent of whether the systems are integrable or non-integrable. In particular, in case of a degenerate spectrum, the time average of the expectation values of different observables is associated with different density matrices, showing that in this case the term “thermalization” is not meaningful. However, from these considerations, we cannot exclude that the emerging quasi-stationary state can be close to a thermal state. In chapter 8 we will show that one can indeed find situations where the final state is very close to a thermal state.

When defining thermal equilibrium, one considers a small system coupled to a bath so that the interaction between both systems can be neglected (aside from the energy that is exchanged) and the total energy is given by the sum of the energy of both systems. In order to investigate this situation, Tasaki considered in Ref. [79] an isolated quantum system consisting of a heat bath and a subsystem with special requirements on the spectrum of both systems and to the coupling between both. When the “hypothesis of equal weights for eigenstates” proposed by him is valid, he derives that $\langle O_{\text{sub}} \rangle(t)$ for observables on the subsystem after large enough times are very similar to the thermal expectation values. In his proof, he finds that the time average is similar to a thermal expectation value if $|\langle n | \psi_0 \rangle|^2$ is non-negligible only for energies close to a certain energy E_n . This, however, is not the general case. From these considerations, it therefore remains open if, in the general case, thermalization can be found in a subsystem. However, note that the expectation values for *local* observables or correlation functions within the extension of the subsystem also follow Eq. (2.38). Therefore, if ϱ_n is non-thermal, the time average of expectation values for observables of the total system as well as of a subsystem will not be similar to a thermal expectation value, hence thermalization for the subsystem only is also not to be expected.

The considerations above leave the question of what nature the statistical operator ϱ could be open. A general framework for obtaining an appropriate statistical operator for a given system is the principle of *maximum statistical entropy* introduced by Jaynes in 1957 [80]. The basic idea is that, from all density operators compatible with the available information, the operator $\tilde{\rho}$ is chosen for which the statistical entropy

$$S = -\text{Tr}(\tilde{\rho} \ln \tilde{\rho}) \quad (2.46)$$

is maximized [81]. This is obtained by considering constants of the motion, which are required to satisfy the condition

$$\text{Tr}(\tilde{\rho} I_i) = \langle I_i \rangle . \quad (2.47)$$

With these constraints, the expression for the statistical entropy is generalized by

introducing Lagrangian multipliers λ_i ,

$$S_{\text{general}} = -\text{Tr}(\tilde{\rho} \ln \tilde{\rho}) - \sum_i \lambda_i \text{Tr}(\tilde{\rho} I_i) - \lambda_0 \text{Tr}(\tilde{\rho}) . \quad (2.48)$$

This leads to a generalized Gibbs-Boltzmann distribution,

$$\rho_{\text{gen}} = e^{-\sum_i \lambda_i I_i} , \quad (2.49)$$

where $I_0 = 1$, so that normalization is enforced via $\text{Tr}(\rho_{\text{gen}} I_0) = \langle I_0 \rangle$. Recently, this approach has been used to investigate the relaxation of hard-core bosons [82, 83] and the behavior of the Luttinger model [84]. For these integrable systems, it is possible to formulate the integrals of motion. However, for a general Bethe-Ansatz integrable many-body system, the constraints are unknown. We note that expectation values for all powers of the Hamiltonian $\langle H^n \rangle$ are time-independent. Therefore, we propose to formulate the generalized Gibbs ensemble using these constants of the motion. We concentrate on the case without degeneracies in the spectrum of the Hamiltonian. Reformulating the Hamiltonian in terms of projectors P_n on its eigenstates,

$$H = \sum_{i=1}^{\dim(H)} E_n P_n , \quad (2.50)$$

the density operator with all powers of H can be rewritten as

$$\begin{aligned} \rho &= \exp\left(-\sum_{m=0}^{\dim(H)} \lambda_m H^m\right) \\ &= \exp\left[-\sum_n \left(\sum_m \lambda_m E_n^m\right) P_n\right] , \end{aligned} \quad (2.51)$$

since $P_n^m = P_n$. Hence, one can consider the P_n as the set of constraints. Note that

$$\langle P_n \rangle = |\langle n | \psi_0 \rangle|^2 \quad (2.52)$$

$$\text{Tr}(\rho P_n) = e^{-\sum_m \lambda_m E_n^m} . \quad (2.53)$$

Since $\langle P_n \rangle = \text{Tr}(\rho P_n)$, Eqs. (2.52) and (2.53) show that *all* Lagrangian multipliers λ_m can be determined via

$$\sum_m \lambda_m E_n^m = -\ln |\langle n | \psi_0 \rangle|^2 , \quad (2.54)$$

since the number of coefficients $|\langle n|\psi_0\rangle|^2$ is $\dim(H)$. The statistical operator is, therefore, *completely determined*, and the time-average of all observables is, via Eqs. (2.39) and (2.40), identical to the statistical average with this density-matrix.

To conclude, in this section we have discussed the possibility of obtaining relaxation to a quasi-stationary state similar to a finite-temperature state when pushing a system with time-independent Hamiltonian out of equilibrium. According to Boltzmann's ergodic hypothesis, this should happen for most systems. Thermalization is not expected for integrable classical systems due to phase-space arguments. Non-integrable, chaotic classical systems are considered to be mixing and hence should thermalize. However, it is not clear if non-integrable quantum many-body systems should show a similar behavior. By analyzing the time evolution of an observable, we find, in the case of a non-degenerate spectrum, that the quasi-stationary state reached after relaxation is fully determined by the initial state, independent of whether the system is integrable or not. Hence, quantum systems after a quench, in general, do not thermalize. We find that the quasi-stationary state is described by a generalized Gibbs-Boltzmann ensemble when using $\dim(H)$ powers of H as constraints of the motion. This will be supported by the results presented in chapter 8.

Chapter 3

Krylov Space Approach to Calculating the Time Evolution

3.1 Iterative Diagonalization Methods

A number of approaches for (at least partially) solving eigenvalue problems up to machine precision or a desired tolerance are known as “Exact Diagonalization” methods. The simplest and most time- and memory- consuming approach is the *complete diagonalization* of the (Hamiltonian) matrix which enables one to calculate *all* desired properties. Usually, this is done by combining the Householder transformation and the QL or QR algorithm, as described, e.g., in Ref. [85]. However, as was shown in the introduction, the dimension of the basis for a strongly interacting quantum system grows exponentially with the system size, so that it is impossible to treat systems with more than a few lattice sites. If only properties of low- or high-lying eigenstates are required, it is possible to reach substantially larger system sizes using *iterative diagonalization* procedures, which, for the obtained eigenstates, yield results to almost machine precision in most cases. The iterative diagonalization methods allow for the calculation of ground-state properties, and (with some extra effort) some low-lying excited states are also accessible. In addition, it is possible to calculate dynamical properties (e.g., spectral functions, time-evolution) as well as behavior at finite temperature. Nearly every system and observable can be calculated in principle, although the convergence properties depend on the system under investigation. In the following, the *Lanczos* and the *Jacobi-Davidson* methods are presented, which are the most widely used iterative diagonalization procedures in physics and quantum chemistry. In particular, the density matrix renormalization group method (DMRG) presented in the next chapter relies on an efficient implementation of an iterative diagonalization procedure. Both algorithms are used in this context; because of its greater

stability we choose the Jacobi-Davidson algorithm for most applications. In the next section, an extension of the Lanczos method is presented which makes it possible to calculate the full time evolution of interacting many-body systems in out-of-equilibrium situations with a very high accuracy.

It is crucial to exploit the symmetries of the system of interest in order to be able to reach the largest possible system sizes – due to the block-diagonal structure of the Hamiltonian matrix, the dimension of the matrices which actually need to be diagonalized is then significantly reduced. An additional advantage is that the results obtained are resolved according to the quantum numbers associated with the symmetries. Useful introductions and discussions of the use of symmetries for specific example Hamiltonians can be found in Refs. [86, 87, 88]. A more general mathematical description in terms of group theory is presented in Ref. [89]. With present-day computers, system sizes can be treated which are large enough to provide insight into the physics of many systems of interest. Applying efficient implementations of iterative diagonalization procedures and maximally exploiting the systems' symmetries, it is possible to treat $S = 1/2$ spin models with up to about $N = 40$ sites. The t - J model on a checkerboard and on a square lattice with 2 holes have been treated on up to $N = 32$ sites. Hubbard models at half filling on a square lattice with up to $N = 20$ sites have been diagonalized; the same size was also reached for quantum dot structures. Models with phonon degrees of freedom such as the Holstein model are much harder to treat because the phonons are bosons, which, in principle, have an infinite number of degrees of freedom. By truncating the number of phonon states, it was possible to treat a chain with $N = 14 +$ phonon pseudo-sites. For these calculations, it was necessary to store between $1.5 - 30 \cdot 10^9$ basis states [90].

3.1.1 Implementation of Quantum Many Body Systems

When implementing the many-body problem on a computer, it is necessary to represent the basis and then to define the action of the Hamiltonian operator on the basis states. In order to have an efficient implementation, it is convenient to map the basis states of the site basis to a single bit or to a set of bits, which, e.g., in C/C++ can be represented by (unsigned) integer variables. The action of an operator on a single basis state can then be implemented by applying a sequence of bit-operators on the integer representing the basis state. However, for bosonic systems, it is necessary to first introduce a cut-off in the number of particles per site so that the site basis has a finite number of states. Typically, one only keeps a very small number of on-site bosons, which may depend on the desired system sizes and the parameter values.

As discussed above, in order to minimize the dimension of the Hamiltonian matrix, it is essential to exploit symmetries of the system, as described in more

full Hilbert space:	dim= $2^{40} = 10^{12}$
constrain to $S_z = 0$:	dim= 138×10^9
using spin inversion:	dim= 69×10^9
utilizing all 40 translations:	dim= 1.7×10^9
using all 4 rotations:	dim= 430, 909, 650

Table 3.1: The reduction of the dimension of the sector of the Hamiltonian containing the ground state for the $S = 1/2$ Heisenberg model on a tilted square lattice with $\sqrt{40} \times \sqrt{40}$ sites. The dimension of the Hilbert space is reduced by a factor of more than 2500 (from Ref. [90]).

detail in Ref. [89]. Given a symmetry group \mathcal{G} with generators g_p , if

$$[H, g_p] = 0, \quad (3.1)$$

the Hilbert space can be partitioned into sectors corresponding to irreducible representations of the symmetry group so that the Hamiltonian matrix \mathbf{H} becomes block diagonal. The solution of the eigenvalue problem for each block then yields the portion of the spectrum of the system associated with a particular conserved quantum number.

It is possible to exploit continuous symmetries, such as the conservation of the particle number or the conservation of the z projection of the spin, S^z . For these symmetries, all possible basis states preserving the symmetry can be obtained by calculating all possible permutations of the bits representing a suitable basis state. It is in principle also possible to implement non-Abelian symmetries like the conservation of the total spin, which is an $SU(2)$ symmetry. However, in general the treatment of these non-Abelian symmetries is more difficult than the treatment of the Abelian ones. When possible, one tries to use other symmetries instead, e.g., instead of using the $SU(2)$ symmetry of the total spin, the Z_2 symmetry related to spin inversion can be used. Space group symmetries include translational invariance, which is an Abelian symmetry, or point group symmetries such as reflections or rotations, which are non-Abelian in general. A set of representative basis states can be formed from symmetrized linear combinations of the original basis states generated by applying the appropriate generators [89].

As an example of how symmetries can reduce the dimension of the largest block of the Hamiltonian that must be diagonalized, we show the size of the sector containing the ground state in Table 3.1.1 for a $S = 1/2$ Heisenberg model on a $\sqrt{40} \times \sqrt{40}$ cluster. In this case, the dimension of the sector to be diagonalized is reduced by a factor of more than 2500.

After considering the symmetries, a set of basis states $\{|n\rangle\}$ is stored in an appropriate form such as a set of bit strings or linear combinations of bit strings. The

most important operation for all iterative diagonalization methods is the multiplication of the Hamiltonian with some wavefunction $|\psi\rangle$. When the Hamiltonian is applied to a basis state $|n\rangle$, the result is a linear combination of basis states

$$H|n\rangle = \sum_{n'} \langle n'|H|n\rangle |n'\rangle, \quad (3.2)$$

where there are typically only a few nonzero terms for a Hamiltonian with only short-ranged interaction or hopping terms. When the states $|n\rangle$ can be represented as bit strings, it is usually easy to identify the bit string corresponding to the set of states $\{|n'\rangle\}$ and to determine the coefficients $\langle n'|H|n\rangle$. However, the bit strings then have to be mapped back to an index into the vector of basis coefficients in order to calculate the coefficients $\langle n|\psi\rangle$. There exist various ways to implement the needed bookkeeping, e.g., by indexing the basis states or by using hash tables [85].

3.1.2 The Lanczos and the Jacobi-Davidson Algorithm

If only the ground state and the low-lying excited states of a system are required, the powerful iterative diagonalization procedures described in this section can handle systems with a Hilbert space dimension substantially (up to four or five orders of magnitude for short-range quantum lattice models) larger than complete diagonalization. Extensions of these methods exist which enable one to investigate dynamical properties, time evolution, and the finite-temperature behavior of the system. In addition, they form a key part of the DMRG algorithm, which carries out an iterative diagonalization in an optimal, self-consistently generated reduced basis for a system.

The basic common idea of the different iterative diagonalization algorithms is to project the matrix to be treated, H , onto a subspace of dimension $M \ll N$ (where N is the dimension of the Hilbert space in which the diagonalization is carried out). This subspace is cleverly chosen so that the extremal eigenstates within the subspace converge very quickly with M to the extremal eigenstates of the system. The most commonly used approach used in physics is the *Lanczos* method, while in quantum-chemistry the *Davidson* or its generalization the *Jacobi-Davidson* algorithm is more widely used.

In this section, we will discuss only the basic Lanczos and Davidson methods for handling hermitian eigenvalue problems. Standard References are Refs. [91, 92, 93], a nice overview and a compact representation of the algorithms can be found in Ref. [94]. The mathematical theory of the Lanczos algorithm has been worked out in Ref. [95].

The Power Method

The simplest iterative diagonalization procedure is the so called *power method*. In this approach, the eigenpair with the extremal eigenvalue is obtained by repeatedly applying the Hamiltonian to a random initial state $|v_0\rangle$,

$$|v_n\rangle = H^n |v_0\rangle . \quad (3.3)$$

Expanding in the eigenbasis $H|i\rangle = \lambda_i|i\rangle$ yields

$$\begin{aligned} |v_n\rangle &= \sum_i \langle i|v_0\rangle H^n|i\rangle \\ &= \sum_i \langle i|v_0\rangle \lambda_i^n|i\rangle . \end{aligned}$$

It is clear that the state with the eigenvalue with the largest absolute value will have the highest weight after many iterations n , provided that $|v_0\rangle$ has a finite overlap with this state. The convergence behavior is determined by the spacing between the extremal eigenvalue and the next one. Since the convergence of the power method is generally much poorer than other methods we will discuss below, it is generally not used in practice.

The subspace generated by the sequence of steps in the power method,

$$\{|v_0\rangle, H|v_0\rangle, H^2|v_0\rangle, \dots, H^n|v_0\rangle\} \quad (3.4)$$

is called *the n^{th} Krylov subspace* and is the starting point for the Lanczos method. Note that, in general, the vectors spanning the Krylov subspace are not orthogonal to each other and thus do not represent a basis. The iterative diagonalization methods discussed now partly rely on orthogonalizing the Krylov vectors. Also note that, if a basis is constructed using the Krylov vectors, and $n > \dim(H)$, the Krylov vectors with $n > \dim(H)$ are linear combinations of the previous $\dim(H)$ vectors.

The Lanczos Method

In the Lanczos method [96], the Hamiltonian is projected onto the Krylov subspace using a basis generated by orthonormalizing the sequence of vectors (3.4) to each other as they are generated. This results in a basis in which the matrix representation of the Hamiltonian becomes *tridiagonal*. The basic algorithm is as follows:

- 0) Choose an initial state $|u_0\rangle$ represented in the system's many-body basis $|n\rangle$ which has finite overlap with the groundstate of the Hamiltonian, but which

must not be an eigenstate of the Hamiltonian. This can be realized by taking $\{|n\rangle\}$ as a vector with random entries.

- 1) Generate the states of the Lanczos basis using the recursion relation

$$\begin{aligned}
 |u_{n+1}\rangle &= H |u_n\rangle - a_n |u_n\rangle - b_n^2 |u_{n-1}\rangle \\
 \text{where } a_n &= \frac{\langle u_n | H | u_n \rangle}{\langle u_n | u_n \rangle} \\
 \text{and } b_n^2 &= \frac{\langle u_n | u_n \rangle}{\langle u_{n-1} | u_{n-1} \rangle}
 \end{aligned} \tag{3.5}$$

with $b_0 \equiv 0$ and $|u_{-1}\rangle \equiv 0$.

- 2) Check if the stopping criterion $\langle u_{n+1} | u_{n+1} \rangle < \varepsilon$ is fulfilled.
 If yes: carry out step 4) and then halt.
 If no: continue.
- 3) Repeat starting with 1) until $n = \dim(H)$.
- 4) If the stopping criterion is fulfilled, diagonalize the resulting tridiagonal matrix

$$\mathbf{T}_n = \begin{pmatrix} a_0 & b_1 & & & \\ b_1 & a_1 & b_2 & \mathbf{0} & \\ & b_2 & a_2 & \ddots & \\ & \mathbf{0} & \ddots & \ddots & b_n \\ & & & b_n & a_n \end{pmatrix} \tag{3.6}$$

using the QL algorithm [85]. The diagonalization yields eigenvalues E_0, \dots, E_n , and eigenstates $|\psi_0\rangle, \dots, |\psi_n\rangle$ which are represented in the Lanczos basis.

- 5) Obtain the desired eigenvectors represented in the original many-body basis $|n\rangle$. This is necessary in order to calculate observables. In order to avoid storing all of the basis states $|u_0\rangle, \dots, |u_n\rangle$, the procedure is repeated starting with the same initial vector $|u_0\rangle$. One obtains the coefficients α_n of the eigenstate in the original basis $|n\rangle$ by carrying out the basis transformation

$$\begin{aligned}
 |\psi_m\rangle &= \sum_i c_i |u_i\rangle \\
 &= \sum_n \sum_i c_i \langle n | u_i \rangle |n\rangle,
 \end{aligned} \tag{3.7}$$

with $\alpha_n \equiv \sum_i c_i \langle n | u_i \rangle$.

The algorithm is memory-efficient, since only the 3 vectors $|u_{n-1}\rangle$, $|u_n\rangle$, and $|u_{n+1}\rangle$ need to be stored at once. As is typically the case in iterative diagonalization procedures, the most time-consuming step is carrying out the multiplication $H|u_n\rangle$, which should be implemented as efficiently as possible, either as described in Sec. 3.1.1, or using other sparse-matrix multiplication routines. The time needed to perform the other steps of the algorithm is generally negligible when N is realistically large. Therefore, optimizing the routine performing $H|\psi\rangle$ is crucial to the efficiency of the implementation.

The Lanczos procedure results in a variational approximation to the extremal eigenvalue which usually attains quite high accuracy after a number of iterations much smaller than the dimension of the Hilbert space. Typically, 100 recursion steps or less are sufficient to attain convergence to almost machine precision for ground state properties [97]. As is evident because the Lanczos method is based on the power method, convergence to extremal eigenvalues occurs first; additional iterations are then necessary to obtain converged excited states. The algorithm is generally considered to be a standard method which can be robustly applied to a wide spectrum of systems. Nevertheless, there are two technical problems which require some care to be taken. First, the convergence of excited states can be irregular; in particular, apparent convergence to a particular value can occur for some range of iterative steps, followed by a relatively abrupt change to another, substantially lower value. It is therefore important to carry out sufficient iterations for the higher excited states. Generally, the number of iterations required to obtain convergence becomes larger for higher excited states.

The second technical problem is the appearance of so-called “ghost” eigenvalues, i.e., spurious eigenvalues which cannot be mapped to eigenvalues of the original Hamiltonian. The origin of such “ghost” eigenvalues can be traced to the loss of the orthogonality of the Lanczos vectors $|u_n\rangle$ due to finite machine precision. It can be shown that the smaller the coefficients b_n , the larger the loss of orthogonality of the vector $|u_n\rangle$ to the other vectors [91, 92]. This is an intrinsic limitation of the algorithm, since, in general, the coefficients b_n become smaller with increasing n . For this reason, the much more stable Householder algorithm [85] rather than the Lanczos procedure is generally used to transform an entire matrix to tridiagonal form. However, because of the good convergence to the ground state and the algorithm’s memory efficiency, the Lanczos method is nevertheless widely used for the investigation of quantum lattice systems with short-ranged coupling.

With some extra effort, it is also possible to overcome the loss of orthogonality which is a basic drawback of the algorithm. The most straightforward solution is to *reorthogonalize* the Lanczos vectors relative to each other using a modified Gram-Schmidt procedure. However, this requires *all* vectors $|u_n\rangle$ to be stored in memory, so that the advantage of memory efficiency is lost. However, an appro-

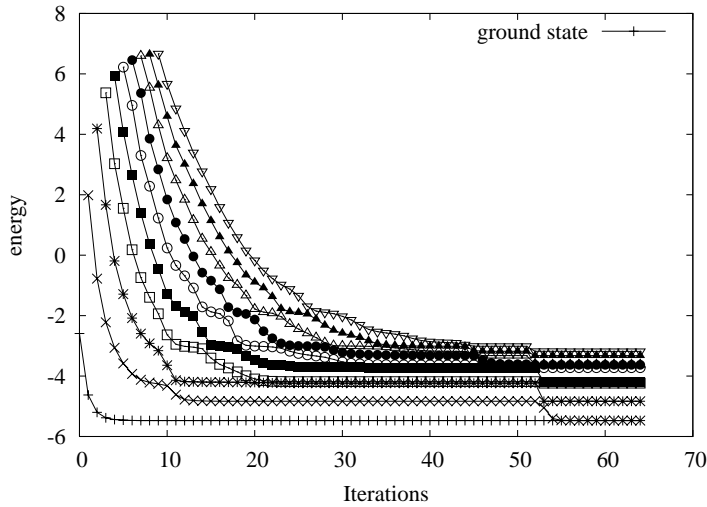


Figure 3.1: Typical convergence behavior of the Lanczos algorithm. In this example, convergence to the ground-state is already reached after approximately 10 iterations, while additional iterations are required to reach convergence for the excited states. “Ghost” eigenvalues appear and converge to a real eigenvalue as additional iterations are performed, leading to erroneous multiplicity at the completion of the calculation.

appropriately chosen partial reorthogonalization is also sufficient; for details see Refs. [92, 93, 94]. Cullum and Willoughby [95, 98] developed a method to eliminate ghost states without reorthogonalizing the Lanczos vectors. In their approach, the eigenvalues of the resulting tridiagonal matrix \mathbf{T}_n are compared to the ones of a similar matrix $\tilde{\mathbf{T}}_n$, which can be obtained by deleting the first row and column of \mathbf{T}_n . This gives a heuristic criterion for the elimination of spurious eigenvalues: since the ghost eigenvalues are generated by roundoff errors, they do not depend on the initial state $|v_0\rangle$ and will be the same for both matrices. After sufficiently many iterations, ghost eigenvalues will converge towards true eigenvalues of the original matrix \mathbf{H} . Thus, every multiple eigenvalue of \mathbf{T}_n is not a ghost and every unique eigenvalue which is not an eigenvalue of $\tilde{\mathbf{T}}_n$ is a true eigenvalue of H . This approach is as memory-efficient as the original Lanczos algorithm and approximately as fast, but generally yields the wrong multiplicity for the eigenvalues.

A number of variants exist like the *implicitly restarted Lanczos*, the *Band-* or the *Block-Lanczos* which can be better for certain problems or have a better treatment of degenerate eigenvalues. For details and for other variants of the Lanczos procedure, see, e.g., Ref. [94].

The generalization of the Lanczos method to non-hermitian operators is the *Arnoldi* method, see, e.g., Ref. [94]. For such problems, a Krylov-space approach

similar to the Lanczos procedure is used to reduce a general matrix to upper Hessenberg form.

A number of software packages are available which provide implementations of iterative diagonalization routines, such as ARPACK [99] or the IETL [100], a part of the ALPS-library [22, 23]. Parts of the results obtained in this thesis are built on the implementation of the Lanczos procedure in the IETL. In order to use this software, a routine which performs the multiplication $H|\psi\rangle$ must be defined by the user; as discussed above, an efficient implementation is crucial to the overall efficiency of the algorithm.

There has been a large number of investigations using the Lanczos procedure. Examples for recent work are the treatment of frustrated quantum magnets, Ref. [101], two-leg ladder systems, Ref. [102], transport through molecules and nanodevices [103], and atomic gases on optical lattices [104].

Davidson and Jacobi-Davidson

The common idea of iterative diagonalization methods is to project the matrix to be diagonalized onto a subspace much smaller than the complete Hilbert space. The subspace, spanned by a set of orthonormal states $\{|u_k\rangle\}$, is then expanded in a stepwise manner so that the approximation to the extremal eigenstates improves. At particular points in or at the end of the procedure, the representation of the Hamiltonian matrix in this subspace is diagonalized. The resulting extremal eigenvalue $\tilde{\lambda}_k$ is called the *Ritz-value* and the corresponding eigenvector the *Ritz-vector* $|\tilde{\psi}_k\rangle$. According to the Ritz variational principle, $\tilde{\lambda}_k$ is always an upper bound to the real ground-state energy, see, e.g., Ref. [64]. The error in applying H to the eigenvector $|\tilde{\psi}_k\rangle$ associated with the Ritz-value $\tilde{\lambda}_k$ is approximated by the *residual vector*

$$|r_k\rangle = H|\tilde{\psi}_k\rangle - \tilde{\lambda}_k|\tilde{\psi}_k\rangle . \quad (3.8)$$

This expression would be exact if $\tilde{\lambda}_k$ were replaced by the exact eigenvalue λ_k . In the Lanczos procedure, the recursion is formulated so that the subspace is expanded by the component of the residual vector $|r_k\rangle$ orthogonal to the subspace.

In 1975, Davidson formulated an alternate iterative algorithm in which the subspace is expanded in the following way [105]. The exact correction to the Ritz-vector is given by

$$|z\rangle = |\psi\rangle - |\tilde{\psi}_k\rangle$$

so that

$$(\mathbf{H} - \lambda_k \mathbf{1})|z\rangle = -(\mathbf{H} - \lambda_k \mathbf{1})|\tilde{\psi}_k\rangle . \quad (3.9)$$

Thus, solving

$$(\mathbf{H} - \lambda_k \mathbf{1})|z\rangle = -|r_k\rangle \quad (3.10)$$

would lead to the exact correction to $|\tilde{\psi}_k\rangle$. This amounts to *inverse iteration* (see, e.g., Ref. [85]). However, the exact eigenvalue λ_k is not known, and the numerical solution of this linear system is of comparable numerical difficulty to the entire diagonalization of the matrix. Davidson's idea was to approximate the correction vector $|z\rangle$ by

$$|z\rangle = -(\mathbf{D} - \tilde{\lambda}_k \mathbf{1})^{-1} |r_k\rangle, \quad (3.11)$$

where the diagonal matrix \mathbf{D} contains the diagonal elements of \mathbf{H} . This is a good approximation if \mathbf{H} is diagonally dominant. If \mathbf{D} were replaced by the unit matrix $\mathbf{1}$, the Davidson algorithm would be equivalent to the Block Lanczos procedure. Therefore, if the diagonal elements of \mathbf{H} were all the same, both methods would have the same performance. For many problems, however, this variation of the diagonal elements is important and the Davidson algorithm converges more rapidly.

In its original formulation, the Davidson algorithm follows the procedure [105]:

- 0) If the k th eigenvalue is to be obtained, choose a subspace of $l \geq k$ orthonormal vectors $|v_1\rangle, |v_2\rangle, \dots, |v_l\rangle$. In the following, the matrix \mathbf{B} is the matrix containing these vectors as columns.
 - 1) i) Form and save the vectors $H|v_1\rangle, H|v_2\rangle, \dots, H|v_l\rangle$. In the following, the matrix $\tilde{\mathbf{A}}$ is the matrix containing these vectors as columns.
 - ii) Construct the matrix $\mathbf{A} = \langle v_i | H | v_j \rangle$ and diagonalize it, obtaining the k th eigenvalue $\lambda_k^{(l)}$ and the corresponding eigenvector $|\alpha_k^{(l)}\rangle$. The upper index (l) denotes that this eigenpair was obtained by keeping l vectors for building the matrix \mathbf{A} .
 - 2) Form the residual vector corresponding to the k th eigenvector,
$$|q_l\rangle = (\tilde{\mathbf{A}} - \lambda_k^{(l)} \mathbf{B}) |\alpha_k^{(l)}\rangle.$$
 - 3) Calculate the norm $\| |q_l\rangle \|$. If $\| |q_l\rangle \| < \epsilon$, accept this eigenpair, otherwise continue.
 - 4) Compute the correction vector $|w_l\rangle = (\mathbf{D} - \lambda_k \mathbf{I})^{-1} |q_l\rangle$, where \mathbf{D} is a matrix containing the diagonal elements of \mathbf{A} and \mathbf{I} is the unit matrix. Orthonormalize $|w_l\rangle$ against $|v_1\rangle, |v_2\rangle, \dots, |v_l\rangle$ to form $|v_{l+1}\rangle$. Expand the the matrix B by adding $|v_{l+1}\rangle$ as an additional column.
 - 5) Form and save the vector $H|v_{l+1}\rangle$. Set $l = l + 1$ and continue with step 1).

Although the Davidson algorithm is somewhat more complicated to implement than the Lanczos algorithm, its convergence is usually of higher order than

the Lanczos method and it is more stable. In particular, spurious ghost eigenvalues do not appear. The disadvantages compared to Lanczos are that $\langle u_i | H | u_j \rangle$ is not tridiagonal, and *all* the $|u_i\rangle$ must be kept in order to carry out the explicit orthogonalization in step 4). Similarly to the Lanczos method, this algorithm can fail for particular choices of the initial vector, e.g., if $|u_0\rangle = |\psi_0\rangle$. In practice, one performs a small number of Davidson iterations and, if necessary, restarts the procedure using the outcome of the previous iteration as initial vectors $|v_1\rangle, \dots, |v_l\rangle$.

A generalization of the original Davidson approach is given by the Jacobi-Davidson method [106]. In this approach, one approximates the correction vector $|z\rangle$ by

$$(\mathcal{H} - \tilde{\lambda}_k \mathbf{1}) |\tilde{z}\rangle = -|r_k\rangle - \varepsilon |u_k\rangle, \quad (3.12)$$

where ε is chosen so that that $\langle u_k | \tilde{z} \rangle = 0$. Here the preconditioner \mathcal{H} is an easily invertible approximation to \mathbf{H} . The choice of an optimal preconditioner is non-trivial and must be tailored to suit the specific problem treated. The Jacobi-Davidson method is more general and flexible than the Davidson method and does not suffer from the lack of convergence when $|u_0\rangle = |\psi_0\rangle$. It is (almost) equivalent to the Davidson method when $\mathcal{H} = \mathbf{D}$. Therefore, it is now widely used instead of the Davidson algorithm, especially in quantum chemistry.

An additional advantage of the Jacobi-Davidson algorithm over the Davidson procedure is that it can be applied to generalized eigenvalue problems,

$$A |x\rangle = \lambda B |x\rangle, \quad (3.13)$$

where A, B are general, complex $n \times n$ matrices [106].

3.2 Time Evolution with the Lanczos Method

Using numerical diagonalization procedures, the most straightforward way to compute the time-evolution of an initial state $|\psi_0\rangle$ is to fully diagonalize the Hamiltonian and compute the wave function at the desired instant of time via

$$|\psi(t)\rangle = \sum_n e^{-iE_n t} \langle n | \psi_0 \rangle |n\rangle, \quad (3.14)$$

with E_n and $|n\rangle$ the eigenvalues and eigenstates of the Hamiltonian, respectively. Unfortunately, as we have seen before, this is only possible for small system sizes. However, generalizing the Lanczos method makes it possible to treat somewhat larger systems with a very high precision, while the additional effort remains comparable to the one when calculating ground states.

The time-dependent Schrödinger equation, Eq. (2.2), is a first-order ODE

which can be numerically solved directly by approximate explicit or implicit integration schemes. An example of an explicit scheme is the 4th order Runge-Kutta method [85], where the next time step is obtained via

$$\begin{aligned}
 |\psi(t + dt)\rangle &\approx |\psi(t)\rangle + \frac{1}{6} (|k_1\rangle + 2(|k_2\rangle + |k_3\rangle) + |k_4\rangle) \\
 |k_1\rangle &= dt \cdot (-i\hat{H}|\psi(t)\rangle) \\
 |k_2\rangle &= dt \cdot \left(-i\hat{H} \left(|\psi(t)\rangle + \frac{dt}{2}|k_1\rangle \right) \right) \\
 |k_3\rangle &= dt \cdot \left(-i\hat{H} \left(|\psi(t)\rangle + \frac{dt}{2}|k_1\rangle + \frac{dt}{2}|k_2\rangle \right) \right) \\
 |k_4\rangle &= dt \cdot \left(-i\hat{H} \left(|\psi(t)\rangle + \frac{dt}{2}|k_1\rangle + \frac{dt}{2}|k_2\rangle + dt|k_3\rangle \right) \right). \quad (3.15)
 \end{aligned}$$

These expressions rely on the operation $\hat{H}|\psi(t)\rangle$. Thus, in principle, an efficient implementation of an iterative diagonalization procedure can be easily expanded for computing time evolution of the system.

This integration scheme is a standard approach, with an error $\varepsilon \propto (dt)^4$, but does not conserve unitarity. An alternative, implicit integration scheme conserving unitarity is the Crank-Nicholson procedure [85]

$$|\psi(t + dt)\rangle \approx \frac{1 - i\hat{H}(t)\delta t/2}{1 + i\hat{H}(t)\delta t/2} |\psi(t)\rangle. \quad (3.16)$$

In this method, the most costly numerical step is the calculation of the inverse (the denominator in Eq. 3.16), which can be carried out using, e.g., a biconjugate gradient approach [107]. The accuracy of this operation also determines the error of this approach. In principle, other, more involved implicit and explicit integration schemes are known (see, e.g., Ref. [85]), but we refrain from discussing them here and turn to an algorithm which we find to work very accurately.

An alternative to the direct integration of the Schrödinger equation is to treat the formal solution

$$|\psi(t)\rangle = \hat{U}|\psi(t)\rangle \quad (3.17)$$

with the time evolution operator $\hat{U} = e^{-i\hat{H}t}$. Thus, it is necessary to treat the exponential of a, in our case usually sparse, matrix. In Ref. [108] a number of methods for computing this matrix exponential are discussed. As it turns out, when computing products of matrix exponentials with vectors, e.g., $e^A|\psi\rangle$, Krylov-space methods can be formulated which are considered to belong to the most efficient approaches.

By projecting the time evolution operator through one interval $[t, t + dt]$ onto

the basis of n Lanczos vectors, one obtains [108, 109]

$$|\psi(t + dt)\rangle = e^{-idt\hat{H}} |\psi(t)\rangle \approx \mathbf{V}_n(t) e^{-idt\mathbf{T}_n(t)} \mathbf{V}_n^T(t) |\psi(t)\rangle, \quad (3.18)$$

where \mathbf{V}_n is the matrix containing all the Lanczos vectors $\{|u_j\rangle\}$ and \mathbf{T}_n is the resultant tridiagonal matrix representation of the Hamiltonian in the same subspace. Again, an efficient implementation of an iterative diagonalization procedure can be easily extended to implement this algorithm. Compared to the Lanczos procedure in equilibrium, it is necessary to store the matrix \mathbf{V}_n , making the method less memory efficient, i.e., the maximum system size is somewhat restricted compared to the iterative diagonalization procedure. However, as discussed below, for typical situations, it is sufficient to keep only $n < 20$ Lanczos vectors, which is only a minor restriction considering the exponential increase of the memory needed when increasing the system size. The matrix exponential $e^{-idt\mathbf{T}_n}$ is then easily obtained by diagonalizing the small tridiagonal matrix \mathbf{T}_n .

It is possible to derive exact error bounds for this Lanczos approximation scheme [109, 11, 110]. For hermitian matrices, one finds

$$\begin{aligned} \varepsilon_n &:= \|\psi(t + dt)\rangle - |\psi(t + dt)\rangle_{\text{approx}}\| \\ &\leq 12 \exp\left\{-\frac{(\varrho dt)^2}{16n}\right\} \left(\frac{e\varrho dt}{4n}\right)^n, \end{aligned} \quad (3.19)$$

$$\text{with } n \geq \frac{1}{2}\varrho dt. \quad (3.20)$$

Here $\|\cdot\|$ represents the Euclidean norm and $\varrho = |E_{\max} - E_{\min}|$ is the width of the spectrum of the Hamiltonian. For typical situations one finds that $n < 20$ is sufficient.

However, in general, ϱ is unknown and the error can thus not be computed. It is necessary to formulate a stopping criterion for the Lanczos iteration. Based on a generalization of the bound for a residual usually used for iterative solvers, a useful stopping criterion, which has been found to work reliably [109], can be formulated [110]. Following Refs. [109, 110], we use the stopping criterion

$$\beta_n \left| [\exp(-idt\mathbf{T}_n)]_{1,n} \right| \| |u_n\rangle \| < \text{tol} \quad (3.21)$$

in our calculations. Putting these steps together, as proposed in Ref. [109], the algorithm for the Lanczos time evolution method is

1. Obtain V_n and T_n by performing the Lanczos iteration scheme with $|\psi(t)\rangle$ as starting vector. Stop the iteration if the stopping criterion, Eq. (3.21), is fulfilled. Orthogonalize the Lanczos vectors to each other so that numerical round-off errors are avoided.

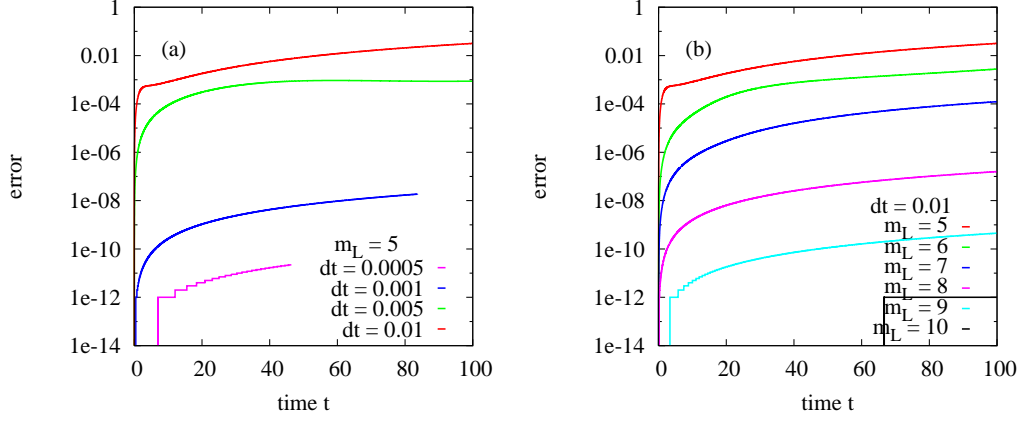


Figure 3.2: Error of the Lanczos time evolution method computed for a system of spinless fermions with $L = 16$ lattice sites, which is accessible to full diagonalization of the Hamiltonian matrix. The error shown is $1 - |\langle \psi_{\text{Lanczos}} | \psi_{\text{FD}} \rangle(t)|^2$. (The displayed data shows results obtained within a calculation time of 24 h on a NEC SX-8).

2. Compute $|\psi(t + dt)\rangle = \mathbf{V}_n(t) e^{-idt \mathbf{T}_n(t)} \mathbf{V}_n^T(t) |\psi(t)\rangle$.
3. If of interest, calculate observables at this time step.
4. Continue starting with step 2 and replacing $|\psi(t)\rangle$ by $|\psi(t + dt)\rangle$ until t_{max} is reached.

For the systems discussed in this thesis and with the present code, it is possible to calculate the time-evolution for up to $L = 26$ sites for spinless fermions, or $L = 16$ sites for soft-core bosons, respectively, using this Krylov-space approach. Using a highly optimized code, somewhat larger system sizes can be reached, but, as discussed above, they would still be quite small. Using the extension of the DMRG to treat time-dependent problems, it is possible to treat the same system sizes much faster and to reach larger systems, as discussed in the next chapters. Nevertheless, it is crucial to have exact, reliable results for smaller systems for testing the various variants of the t-DMRG.

In Fig. 3.2, the evolution of the error with time is shown. The error displayed is the error in the overlap between the state at time t obtained with full diagonalization, $|\psi_{\text{FD}}\rangle(t)$, and with the Lanczos method, $|\psi_{\text{Lanczos}}\rangle(t)$. The plots display $1 - |\langle \psi_{\text{Lanczos}} | \psi_{\text{FD}} \rangle(t)|^2$. (Note that this quantity is roughly the square of the error defined in Eq. (3.19)). As can be seen, the error is very small.

In Fig. 3.2 (a), the number of Lanczos vectors m_L used during the time evolution is kept fixed to $m_L = 5$ and the time step is changed. In Fig. 3.2 (b), the time step is fixed to $dt = 0.01$ and the number of Lanczos vectors is varied from 5 to 10. Since we are treating the system with complete diagonalization, ϱ is known and the error bound (3.19) can be computed. The error estimate obtained in this way is much higher than the error obtained in the simulation. When using $m_L = 5$ and $dt = 0.01$, the error estimate from Eq. (3.19) for one time step is $\| |\psi_{\text{Lanczos}}\rangle - |\psi_{\text{FD}}\rangle \| \approx 0.09$. After 10000 time-steps at time $t = 100$, the error in the overlap is $\approx 3.5\%$, a number which is of the order of the error estimate, Eq. (3.19), for a *single* time step. For more complicated situations when ϱ is not accessible, the stopping criterion, Eq. (3.21), is used. The parameters used for the calculations presented are $\text{tol} < 10^{-13}$, $dt = 0.0005$ and the minimum number of Lanczos vectors $m_{L,\text{min}} = 10$. For the systems of interest with sizes accessible to full diagonalization, we find that these quite strong restrictions lead to an error of the order of the machine precision for all times computed. Thus, results for the time evolution obtained using the Lanczos method are considered to be *exact* in the following. This is particularly important when testing the accuracy of the time-dependent DMRG presented in chapter 6.

Chapter 4

The Density Matrix Renormalization Group Method for Systems in Equilibrium

The basic idea of the density-matrix renormalization group method is to represent one or more states of a finite system approximately by dividing the system in two and retaining only the m most highly weighted eigenstates of the reduced density matrix of the partial system. The combination of the *numerical renormalization group* approach (NRG) developed by Wilson [16] and the superbloc algorithms developed by White and Noack [111] leads to a very powerful and efficient tool for the investigation of one-dimensional strongly correlated quantum systems on a lattice. Reviews can be found in Refs. [2, 3, 4, 112].

As depicted in Fig. 4.1, the key steps are to *increase* the number of degrees of freedom of the partial system by adding sites, then to *decrease* the number of degrees of freedom by retaining states above a cutoff. In this way, the method carries out a renormalization group procedure closely related to Wilson's NRG, who was awarded the Nobel prize in physics in 1982 for his renormalization group theory for critical phenomena. The key idea of the NRG is to work in a restricted basis composed of the lowest lying eigenstates of the Hamiltonian. It is then possible to formulate a renormalization group (RG) transformation and to find the fixed points of the RG flow. The NRG can be applied successfully to impurity systems (e.g., to the Kondo problem) and is still being actively developed. In particular, extensions for time-dependent problems have been formulated recently [113]. An introduction to the NRG can be found in Ref. [4] and references therein.

As it turns out, the approach used by the NRG can only treat a restricted class of systems accurately. The main reason for this is that the basis of energy eigenstates is not always appropriate for representing all features of the system while performing the renormalization group procedure. As a simple test system for

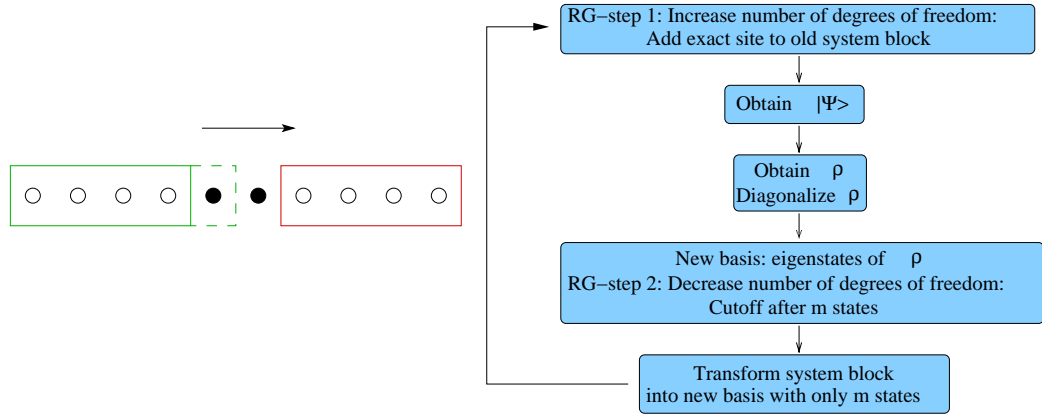


Figure 4.1: Sketch of the lattice and flowchart of the DMRG iteration scheme. The lattice is shown in the usual “superblock” configuration, where the left part of the lattice is the subsystem which is used to compute the basis of density matrix eigenstates. At the ‘dividing’ bond, two “exact” sites are added; the “sweep” proceeds from left to right. The flowchart at the right shows the relevant steps of the DMRG procedure as described in the text.

renormalization group methods, Wilson suggested treating a single quantum particle in a box. The NRG procedure is not able to find the real ground state. When working in real space, adding the energy eigenstates of two subsystems will lead to a wave function which differs significantly from the wave function of the full system, as demonstrated in Fig. 4.2. In the following, we discuss how algorithms for the solution of this basic problem have been formulated which, when extended to interacting systems, lead to the DMRG.

4.1 RG-like methods for a particle in a box

For a single particle on a lattice modelled by the tight-binding model,

$$H^{\text{tb}} = - \sum_j t_j (c_j^\dagger c_{j+1} + c_{j+1}^\dagger c_j) . \quad (4.1)$$

the basic idea of the NRG, i.e., to work in an effective basis obtained by retaining only a part of the energy eigenstates, can be improved by applying a more general set of boundary conditions to the subsystems building up the complete system. When putting two subsystems (referred to as “blocks”) together, one can apply fixed (vanishing wave function in the continuum limit) or free boundary

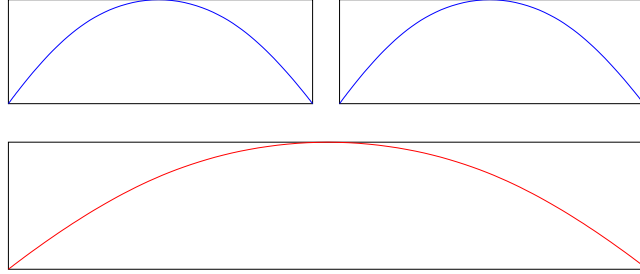


Figure 4.2: Failure of the NRG procedure for a single quantum particle confined in a box. Adding the energy eigenstates of two subsystems leads to a state significantly different to the real eigenstate of the combined system.

conditions (vanishing first derivative) by forming the matrix

$$\mathbf{H}_{2L}^{bb'} = \begin{pmatrix} \bar{\mathbf{H}}_L^{b,\text{fixed}} & \bar{\mathbf{T}}_L \\ \bar{\mathbf{T}}_L^\dagger & \bar{\mathbf{H}}_L^{\text{fixed},b'} \end{pmatrix}. \quad (4.2)$$

Here, $\bar{\mathbf{H}}$ is the Hamiltonian matrix on one of the blocks and $\bar{\mathbf{T}}$ contains the terms connecting both blocks. Both operators are, in the course of the iteration, represented in an appropriate, effective basis, as discussed below. The boundary condition b can be fixed or free [111], and the Hamiltonian $\mathbf{H}_{2L}^{bb'}$ can then be diagonalized for all 4 combinations of boundary conditions to obtain a more general set of basis functions. A transformation matrix \mathbf{O}_L is now constructed by taking a small number of eigenstates from each set $\{b, b'\}$ and orthogonalizing them numerically using the Gram–Schmidt procedure, thus obtaining an undercomplete set of basis states, resulting in an orthogonal transformation in an undercomplete basis, as in the NRG. The new operators, $\bar{\mathbf{H}}$ and $\bar{\mathbf{T}}$, are obtained by transforming to this new basis in order to prepare for the next step. This “combination of boundary conditions” method works astoundingly well, producing the first few eigenvalues to almost machine accuracy for a 2048-site lattice, keeping only $m = 8$ states [111]. Unfortunately, no good method has been found to extend these “combination of boundary conditions” methods to the general case of an interacting many-particle system. The reason is that it is not clear that an appropriately general set of boundary conditions can be found for a many-particle wave function, which is a complicated function of the coordinates of all the particles. However, another method developed in Ref. [111], called the *superblock* method, can be generalized to interacting systems, leading to the DMRG. Rather than applying a general set of boundary conditions to a block of size L , in the superblock method a new basis for $\bar{\mathbf{H}}_{2L}$ and $\bar{\mathbf{T}}_{2L}$ is formed based on the idea that these blocks will eventually make up part of a larger system. In order to do this, a “superblock” (with periodic

boundary conditions) made up of $p > 2$ blocks is formed and diagonalized. For example,

$$\mathbf{H}_{2L}^{p=4} = \begin{pmatrix} \bar{\mathbf{H}}_L & \bar{\mathbf{T}}_L & 0 & \bar{\mathbf{T}}_L^\dagger \\ \bar{\mathbf{T}}_L^\dagger & \bar{\mathbf{H}}_L & \bar{\mathbf{T}}_L & 0 \\ 0 & \bar{\mathbf{T}}_L^\dagger & \bar{\mathbf{H}}_L & \bar{\mathbf{T}}_L \\ \bar{\mathbf{T}}_L & 0 & \bar{\mathbf{T}}_L^\dagger & \bar{\mathbf{H}}_L \end{pmatrix}. \quad (4.3)$$

The transformation matrix \mathbf{O}_{2L} is then obtained by projecting the m lowest-lying eigenstates of \mathbf{H}_{2L}^p onto the coordinates of the first two blocks, and then orthonormalizing the resulting vectors. In other words, if u_j^α (with $j = 1, \dots, 4m$) is an eigenvector of the superblock Hamiltonian \mathbf{H}_{2L}^4 , then projecting onto the coordinates of the first two blocks means considering the first $2m$ elements $j = 1, \dots, 2m$ of u_j^α , assuming $\bar{\mathbf{H}}_L$ is an $m \times m$ matrix. The resulting vectors are then orthonormalized and give the column vectors of the transformation matrix \mathbf{O}_{2L} . This new basis is used to transform the block-operators, $\bar{\mathbf{H}}_{2L} = \mathbf{O}_{2L}^\dagger \mathbf{H}_{2L} \mathbf{O}_{2L}$ and $\bar{\mathbf{T}}_{2L} = \mathbf{O}_{2L}^\dagger \mathbf{T}_{2L} \mathbf{O}_{2L}$, used as a starting point to build up the superblock in the next iteration step.

The superblock method yields good results for the single-particle tight-binding chain, albeit not as accurate as the fixed-free variant of the combination of boundary conditions method [111]. In the subsequent sections we describe how DMRG algorithms for interacting systems building on the superblock method can be formulated.

It is worth mentioning that it is possible to treat the single particle on a tight-binding chain, Hamiltonian (4.1), using an algorithm that is a direct adaptation of the DMRG for interacting systems [114]. This algorithm is linear in the system size L and involves diagonalizing only a 4×4 matrix at each DMRG step [115], since the effective basis obtained for each block can be shown to consist of only one number for the non-interacting problem [114, 115]. Since the single-particle algorithm contains the essential ingredients of the DMRG algorithm for interacting systems, understanding the single-particle algorithm is useful in gaining insight into the algorithm for interacting systems. Example implementations of this algorithm can be found in [114], and as part of the ALPS application library [22, 23].

4.2 Density Matrix Projection for Interacting Systems

The density matrix renormalization group method is one of the most efficient numerical methods for one-dimensional strongly correlated quantum systems. By now, the method has been discussed in a number of review articles [2, 3, 4, 116]. In addition, a collection of papers using the DMRG or treating subjects connected to the DMRG can be found in Ref. [117]; a survey is presented in Ref. [118].

As we have seen in Sec. 4.1, the crucial step of the superblock method is a projection of the wave function of the superblock onto a subsystem, consisting of two identical blocks in the algorithm for the noninteracting particle. Here we consider how to carry out such a projection for a many-body wave function in an optimal way. In order to do this, we briefly review the general quantum mechanical description of a system divided into two parts.

The density matrix is the most general description of a quantum mechanical system because, in contrast to a description in terms of the wave function, it can be used to describe a system in a mixed state as well as in a pure state [119, 120]. For a general, mixed state, the density matrix of a system is given by

$$\rho = \sum_{\alpha} C_{\alpha} |\Psi_{\alpha}\rangle\langle\Psi_{\alpha}|, \quad (4.4)$$

where the coefficients C_{α} are the weights of the states in the mixed ensemble and are normalized so that $\text{Tr} \rho = 1$. The density matrix for a system in a pure state would have just one term in the sum. Given ρ , a subsystem A can be described by tracing out the degrees of freedom $|j\rangle$ of the rest of the system, yielding the *reduced density matrix*

$$\rho_A = \text{Tr}_{|j\rangle} \rho. \quad (4.5)$$

The eigenstates of ρ_A form a complete basis for the subsystem A ; its eigenvalues w_{α} give the weight of state α in the ensemble and carry the information about the entanglement of the subsystem with the rest of the system. The amount of entanglement can be quantified by the mutual quantum information (or *von Neumann*) entropy

$$\begin{aligned} S(\rho) &= -\text{Tr}_{|j\rangle} (\rho \log \rho) \\ &= -\sum_{\alpha} w_{\alpha} \log w_{\alpha}. \end{aligned} \quad (4.6)$$

This feature makes a connection between the DMRG and quantum information theory, which is an active topic of current research. If a system in a pure state $|\psi\rangle$ is divided into two parts (A and B), $|\psi\rangle$ can be expressed in terms of the eigenstates

of the reduced density matrices of part A, $|\phi_\alpha\rangle$, and part B, $|\chi_\alpha\rangle$ using the *Schmidt decomposition* [121, 122]

$$|\psi\rangle = \sum_{\alpha} \sqrt{w_{\alpha}} |\phi_{\alpha}\rangle |\chi_{\alpha}\rangle. \quad (4.7)$$

Here the sum is over the nonzero eigenvalues w_{α} of the density matrices of either part, which can be shown to be the same. The dependence of the eigenvalues w_{α} on α relies on the wave function considered and on how the two subsystems are chosen. If only a small number (i.e., substantially less than the dimension of the smallest of the two density matrices) of the w_{α} are nonzero, $|\psi\rangle$ can be represented exactly by the sum over the corresponding states. If the w_{α} fall off sufficiently rapidly with α , $|\psi\rangle$ can be well approximated by truncating the sum in Eq. (4.7) to the m eigenstates of the density matrix with the largest eigenvalues. This is the case for, e.g., one-dimensional quantum many-body systems with a gapped spectrum, i.e., away from a quantum critical point, for which w_{α} falls off exponentially. The behavior of the w_{α} for various quasi one-dimensional and two dimensional systems is discussed in Ref. [3]. A useful approximation can be achieved if m can be taken to be much smaller than the dimension of the eigenbasis of the density matrix. This approximation can be shown to be optimal in the sense of a least-squares minimization of the differences between the exact $|\psi\rangle$ and the approximate one [123] and is equivalent to the singular value decomposition [85]. Finally, if the w_{α} fall off too slowly or not at all, a truncation of the Schmidt decomposition becomes a bad approximation for $|\psi\rangle$. The worst case is when all the w_{α} are equal, which occurs for a maximally entangled state. A representation optimized for multiple states rather than just $|\psi\rangle$ can be constructed by including additional states (called “target states”) in the density matrix, Eq. (4.4) with appropriate weights C_{α} . However, the density-matrix eigenstates now have to be selected such that all target states can be represented well; a rough estimate is that for each target state the same number of density-matrix eigenstates is needed in order to obtain the same accuracy, so that, roughly, m is expected to grow proportionally with the number of target states. Now, we focus on the case with only one target state. A measure for the error of this approximation is the sum over the weights of the discarded density-matrix eigenstates,

$$\mathcal{E}_{\text{discard}} = \sum_m^N w_{\alpha}, \quad (4.8)$$

with N the dimension of the system’s Hilbert space. This is called the *discarded weight*. In typical DMRG runs, after having reached convergence, one obtains $\mathcal{E}_{\text{discard}} \sim 10^{-6} - 10^{-9}$ by keeping only $m = 1000$ or less density matrix eigenstates.

Thus, using the basis of density matrix eigenstates, an “optimal” description for a quantum many-body system can be found (for details, see Ref. [114]). In the usual case, the calculation is performed in order to obtain the ground state of the system in a particular symmetry sector of the Hilbert space. Thus, only one target state is kept and the density matrix, Eq. (4.4), has just one term in the sum. Here and in the following, we will therefore discuss the procedure for a calculation with a single target state; the generalization to multiple target states is straightforward. The basic procedure to carry out the truncation is then:

1. Obtain the ground state $|\psi\rangle$ of a finite lattice system using an iterative diagonalization procedure (e.g., the Lanczos or Davidson algorithms).
2. Divide the system in two and obtain the m most important eigenstates of the reduced density matrix of one of the subsystems.
3. Transform the system block into the new (approximate) basis with only m states.

In the following, the implementation of the DMRG is discussed. For pedagogical example implementations for the noninteracting case, we refer the reader to Refs. [23, 114].

4.3 DMRG Algorithms

The goal in formulating DMRG algorithms is to embed an NRG-like iterative buildup and truncation of a system, termed “system block”, in a larger system, the superblock. As described in the previous section, an iterative diagonalization is carried out on the superblock to obtain the ground state and possibly some other states, and the eigenstates of the corresponding reduced density matrix with the largest weights are used to form a new truncated basis for the system block. In order to construct DMRG algorithms, two elements of the procedure must still be formulated: how the system block is built up, i.e., how degrees of freedom are added, and how the remainder of the superblock, termed “environment” or “environment block”, is chosen. In the NRG a single site at a time is added to the system, allowing a substantial fraction of the energy eigenstates ($1/N_\ell$, where N_ℓ is the number of states on site ℓ) to be kept at each step. In the DMRG, it is also important to minimize the number of degrees of freedom, especially since the system to be diagonalized, the superblock, contains many additional degrees of freedom in the environment block. Therefore, a single site is added to the system block at each step in almost all variants of the DMRG algorithm. There is more freedom to choose how the environment block is constructed: the algorithms generally fall

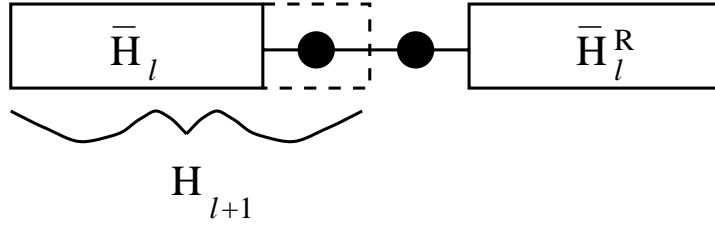


Figure 4.3: Typical superblock configuration for DMRG algorithms.

into two classes, depending on how the superblock evolves with iteration. In the infinite system procedure, the size of the superblock increases at each step in a fashion reminiscent of the NRG, and in the finite system procedure, the environment block is chosen so that the size of the superblock remains constant, allowing an iterative improvement of the wave function or wave functions for one particular finite system.

4.3.1 Infinite System Algorithm

In the infinite system algorithm, the environment block is chosen to be a reflection of the system block, (usually) including the added site. Therefore, the superblock grows by two sites at each iteration (as opposed to one site in the NRG) and the algorithm can be used to scale towards the infinite system fixed point, or, as we will see, can be used to build up an initial approximation to a system of a particular size, which can then be further improved with the finite system procedure. Such additional finite system iteration is necessary for most systems because the infinite system algorithm is not guaranteed to achieve variational convergence with the number of states kept, see Refs. [114, 124].

The infinite system algorithm for the calculation of the ground state of a one-dimensional reflection symmetric lattice proceeds as follows.

1. Form a superblock containing L sites which is small enough to be exactly diagonalized.
2. Diagonalize the superblock Hamiltonian H_L^{super} numerically, obtaining *only* the ground state eigenvalue and eigenvector ψ using the Lanczos or Davidson algorithm.
3. Form the reduced density matrix $\rho_{i' i'}$ for the current system block from ψ using $\rho_{i' i'} = \sum_j \psi_{i' j}^* \psi_{i' j}$, where $|i\rangle$ is the basis of the system block of size $\ell + 1$, $|j\rangle$ the basis of the corresponding environment block, and $\psi_{i' j} = \langle i' | \langle j | \psi \rangle$. Note that $\ell' = \ell = L/2 - 1$.

4. Diagonalize $\rho_{ii'}$ with a dense matrix diagonalization routine to obtain the m eigenvectors with the largest eigenvalues.
5. Construct the Hamiltonian matrix $\mathbf{H}_{\ell+1}$ of the new system block (i.e., the left block $A + s$) and other operators needed in the course of the iteration (e.g., observables). Transform them to the reduced density matrix eigenbasis using $\bar{\mathbf{H}}_{\ell+1}^\alpha = \mathbf{O}_L^\dagger \mathbf{H}_{\ell+1}^\alpha \mathbf{O}_L$, $\bar{\mathbf{A}}_{\ell+1} = \mathbf{O}_L^\dagger \mathbf{A}_{\ell+1} \mathbf{O}_L$, etc., where the columns of \mathbf{O}_L contain the m eigenvectors of $\rho_{ii'}$ with the highest eigenvalues, and $\mathbf{A}_{\ell+1}$ is an operator in the system block.
6. Form a superblock of size $L + 2$ using $\bar{\mathbf{H}}_{\ell+1}$, two single sites and $\bar{\mathbf{H}}_{\ell+1}^R$.
7. Repeat starting with step 2, substituting H_{L+2}^{super} for H_L^{super} .

The implementation details for the individual steps will be described in Sec. 4.3.3. In order to obtain an efficient program, bases and operators should be decomposed according to the symmetries of the Hamiltonian whenever possible. For an introduction to the use of symmetries within the DMRG framework, see Ref. [88].

This procedure has been formulated to obtain only the ground state, but it is easy to extend it to multiple target states by constructing additional states during step 2, either by continuing the diagonalization to obtain excited states or by applying operators to $|\psi\rangle$. These additional states are then mixed into the reduced density matrix in step 3 with appropriate weights, as discussed in Sec. 4.2.

Here a reflection-symmetric one-dimensional system has been assumed. It is possible to generalize the infinite system algorithm to non-reflection-symmetric lattices by building up the left half and the right half of the system alternately. However, such algorithms have not been particularly important because the finite system algorithm, discussed below, can treat such cases and can be generalized to systems that are not one-dimensional chains.

The results of the procedure are the energies and wave functions obtained in step 2. At this point, matrix elements of operators within a state and between states can be calculated, provided that the operators have been formed in the appropriate basis, i.e., the same basis in which $|\psi\rangle$ is represented in step 2.

4.3.2 Finite System Algorithm

The infinite system method has the weakness that the wave function targeted at each step is different because the lattice size is different. This can lead to poor convergence or complete lack of convergence with m if the wave function changes qualitatively between steps. This can occur for states with some incommensuration with the lattice caused by, for example, fermions with a non-integral filling or excited states characterized by a particular wavevector.

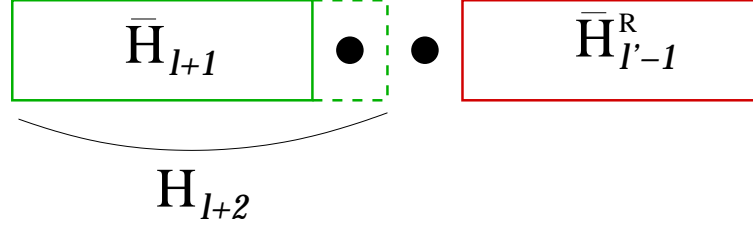


Figure 4.4: A schematic depiction of a step in the finite system algorithm.

Therefore, an algorithm in which the same finite system is treated at each step is very useful. Instead of convergence to an infinite-system fixed point with iteration, there is variational convergence to the wave function or set of wave functions for a particular finite system. Such an algorithm can be formulated by choosing a block of appropriate size from a previous step as the environment block.

The finite system algorithm for finding the ground state on a one-dimensional lattice proceeds as follows:

0. Carry out the infinite system algorithm or another buildup procedure until the superblock reaches size L , storing \bar{H}_ℓ and the operators needed to connect the blocks at each step.
1. Carry out steps 3-5 of the infinite system algorithm to obtain $\bar{H}_{\ell+1}$. Store it. (Now $\ell \neq \ell'$.)
2. Form a superblock of size L using $\bar{H}_{\ell+1}$, two single sites and $\bar{H}_{\ell'-1}^R$. The superblock configuration is shown in Fig. 4.4 where $\ell' = L - \ell - 2$.
3. Repeat steps 1-2 until $\ell = L - 3$ (i.e. $\ell' = 1$). This is the *left to right* phase of the algorithm.
4. Carry out steps 3-5 of the infinite system algorithm, reversing the roles of \bar{H}_ℓ and $\bar{H}_{\ell'}^R$, i.e. switch directions to build up the right block and obtain $\bar{H}_{\ell'+1}^R$ using the stored \bar{H}_ℓ as the environment. Store $\bar{H}_{\ell'+1}^R$.
5. Form a superblock of size L using $\bar{H}_{\ell-1}$, two single sites and $\bar{H}_{\ell'+1}^R$.
6. Repeat steps 4-5 until $\ell = 1$. This is the *right to left* phase of the algorithm.
7. Repeat starting with step 1.

This procedure is illustrated schematically in Fig. 4.4.

One iteration of the outermost loop is usually called a finite system iteration or finite system sweep. If the lattice is reflection symmetric, the procedure can be shortened by reversing direction at the reflection symmetric point, $\ell = L/2 - 1$, i.e., by using the reflection symmetry to interchange the role of the left and right blocks at this point. In this formulation, we have assumed that the infinite system algorithm can be carried out to build up the lattice to the desired size and to generate an initial set of environment blocks. If this is not the case, the finite system method can still be applied if a reasonable approximation is used for the environment block in the first finite system sweep. The simplest such approximation is to use a null environment block, which is equivalent to the Wilson NRG procedure; a better one is to use a few exactly treated sites as the environment. As long as this initial procedure does not lead to a system block basis that is too bad, convergence is reached after a relatively small number of finite system iterations for most systems, typically between 2 and 10 for one-dimensional systems.

Note that, as in the infinite system algorithm, it is also possible to obtain results for several target states by mixing additional states into the density matrix in step 3.

We show an example of the behavior of the ground-state energy in the course of a DMRG run for the half-filled one-dimensional Hubbard model in Fig. 4.5. Note that the convergence is clearly variational and that there is a significant downwards jump in the energy when the direction is changed at the middle of the chain in the finite system algorithm. This is due to a qualitative improvement in the representation of the system at the point where the reflected system block can also be used as the environment block.

Since its introduction in 1992, the DMRG has become a standard method for obtaining the ground-state properties of one-dimensional short-range quantum lattice models. Among the first and most extensive areas of application have been spin chains with half-integral and integral spin [1, 123, 125], as well as frustrated spin chains [126]. One-dimensional fermionic systems [127, 128, 129] have been treated in many variations. Since the amount of work done on such models is quite large, a comprehensive survey is beyond the scope of this thesis; we refer the reader to [2, 116, 3, 112] for further references.

4.3.3 Programming Details

In this section, we discuss the details of implementing the DMRG algorithm, paying particular regard to efficiency. We follow Ref. [2] in that we take the one-dimensional Heisenberg model with nearest-neighbor exchange term

$$\mathbf{S}_\ell \cdot \mathbf{S}_{\ell+1} = S_\ell^z S_{\ell+1}^z + \frac{1}{2} (S_\ell^+ S_{\ell+1}^- + S_\ell^- S_{\ell+1}^+) \quad (4.9)$$

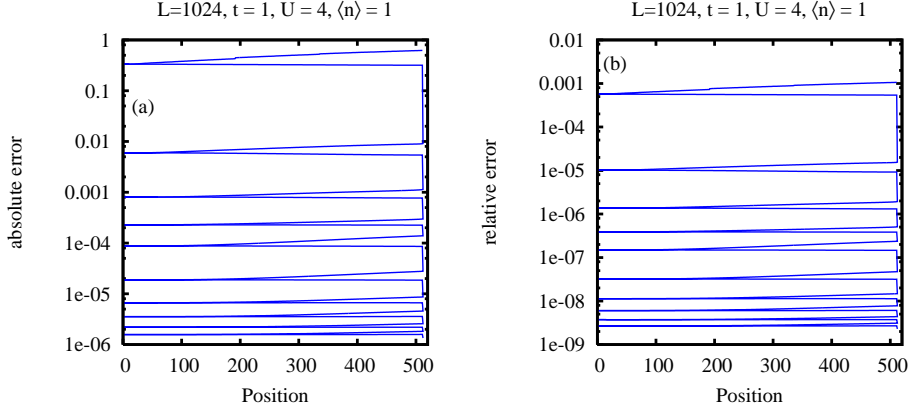


Figure 4.5: Convergence of the DMRG for a one-dimensional Hubbard model of length $L = 1024$ with $U/t = 4$ at half-filling. The absolute error in the ground-state energy when comparing to the exact ground state energy obtained from the Bethe Ansatz is shown in (a), while in (b) the relative error is displayed. “Position” refers to the position at which a site is added. The infinite system algorithm (not shown) followed by ten sweeps of the reflection-symmetric version of the finite system algorithm are carried out.

as an example. Generalization to other short-range Hamiltonians is straightforward. Any DMRG program will contain the following three crucial elements:

1. The addition of two blocks (usually the system block and a site).
2. The multiplication $H^{\text{super}}|\psi\rangle$.
3. The basis transformation of relevant operators on a block to the truncated basis of density matrix eigenstates.

When two blocks are added, the part of the Hamiltonian internal to each block as well as all terms connecting the two blocks must be constructed. For the example, the terms that must be constructed are

$$\begin{aligned}
 [H_{12}]_{i'v;jj'} = & [H_1]_{i'v} \delta_{jj'} + \delta_{i'v} [H_2]_{jj'} + [S_\ell^z]_{i'v} [S_{\ell+1}^z]_{jj'} \\
 & + \frac{1}{2} \left([S_\ell^+]_{i'v} [S_{\ell+1}^-]_{jj'} + [S_\ell^-]_{i'v} [S_{\ell+1}^+]_{jj'} \right) . \quad (4.10)
 \end{aligned}$$

Note that the matrix representation of each operator appearing in Eq. (4.10) must be available in the current basis; such operators must be constructed and transformed at each appropriate previous step.

The multiplication $H^{\text{super}}|\psi\rangle$ is the most time-consuming operation in the DMRG algorithm. The following is an efficient procedure to perform this operation within the framework of the DMRG; it should be regarded as the standard method. Assuming that the system is bipartite, the superblock Hamiltonian can be constructed using

$$[H^{\text{super}}]_{ij;i'j'} = \sum_{\alpha} A_{ii'}^{\alpha} B_{jj'}^{\alpha}, \quad (4.11)$$

where the \mathbf{A}^{α} are the matrix representations of the appropriate operators on the left block, and the \mathbf{B}^{α} on the right block. The index α iterates over all pairs of operators that are needed to construct the superblock Hamiltonian, as given in Eq. (4.10), for the example system. The product with the wave function in the appropriate superblock configuration is then

$$\sum_{i'j'} [H^{\text{super}}]_{ij;i'j'} \psi_{i'j'} = \sum_{\alpha} \sum_{i'} A_{ii'}^{\alpha} \sum_{j'} B_{jj'}^{\alpha} \psi_{i'j'}. \quad (4.12)$$

For each α , this expression is equivalent to the multiplication of three matrices

$$H^{\text{super}}\psi = \sum_{\alpha} \mathbf{A}^{\alpha} (\mathbf{B}^{\alpha} \psi^T)^T, \quad (4.13)$$

which can be carried out in order m^3 operations. Note that when using complex arithmetics the same expression is valid.

In the course of the DMRG procedure, all of the above matrices as well as the operators required to calculate desired observables must be transformed into the new truncated basis given by the m density-matrix eigenvectors with largest weight. If the transformation matrix $O_{ij;\alpha}$ is composed of m basis vectors u_{ij}^{α} , the operator $A_{ij;i'j'}$ is transformed as

$$A_{\alpha\alpha'} = \sum_{i,j,i',j'} O_{ij;\alpha}^* A_{ij;i'j'} O_{i'j';\alpha'}, \quad (4.14)$$

leading to a reduction of the dimension of the matrix representing A from $(m_1 m_2) \times (m_1 m_2)$ to $m \times m$.

In order to make the above procedures as efficient as possible, it is necessary to exploit the symmetries of the system, like, e.g, conservation of the particle number. The sums over sets of states can be divided up into sectors corresponding to different quantum numbers. Once this is done, only the nonzero parts of the matrix representations of the operators which connect particular quantum numbers must be stored and the multiplications can be decomposed into sums over multiplications of these non-vanishing pieces. Use of non-Abelian symmetries is also possible, but is substantially more difficult [130, 131, 132]. In order to treat large

systems and make m as large as possible, it is also important to minimize the use of main memory. This can be done by storing the matrix representations of operators not currently needed on secondary storage. In particular, relevant operators for blocks that are not needed in the superblock configuration at a given step of the finite system procedure, but which will be needed in a subsequent step, need not be retained in primary storage.

4.3.4 Measurements

What are termed “measurements” in the DMRG framework are expectation values of operators calculated within a state or between states of the superblock, which are obtained in the iterative diagonalization step. The procedure is straightforward, provided that the necessary operators are available in the appropriate basis. Given a state ψ_{ij} of the two-block system, the single-site expectation value $\langle \psi | S_\ell^z | \psi \rangle$ is given by

$$\langle \psi | S_\ell^z | \psi \rangle = \sum_{i,i',j} \psi_{ij}^* [S_\ell^z]_{i'i'} \psi_{i'j}. \quad (4.15)$$

The matrix representation $[S_\ell^z]_{i'i'}$ is constructed when the site ℓ is added to the system block, and must be transformed at each subsequent step so that it is available in the basis $|i\rangle$.

For expectation values of operators on two different sites, such as the correlation function $\langle \psi | S_\ell^z S_m^z | \psi \rangle$, how the operators are constructed depends on whether the two sites ℓ and m are on the same or on different blocks. If they are located on different blocks, then the expectation value can be formed using

$$\langle \psi | S_\ell^z S_m^z | \psi \rangle = \sum_{i,i',j,j'} \psi_{ij}^* [S_\ell^z]_{i'i'} [S_m^z]_{j'j} \psi_{i'j'}, \quad (4.16)$$

where $[S_\ell^z]_{i'i'}$ and $[S_m^z]_{j'j}$ are the individual single-site operators. However, if ℓ and m are on the *same* block, the expression

$$\langle \psi | S_\ell^z S_m^z | \psi \rangle \approx \sum_{i,i',i'',j} \psi_{ij}^* [S_\ell^z]_{i'i'} [S_m^z]_{i''i'} \psi_{i''j} \quad (4.17)$$

is *incorrect* within the approximation for ψ_{ij} because the sum over i' extends over the current truncated basis rather than a complete set of states. The correct way to calculate the two-site expectation value is to use the relation

$$\langle \psi | S_\ell^z S_m^z | \psi \rangle = \sum_{i,i',j} \psi_{ij}^* [S_\ell^z S_m^z]_{i'i'} \psi_{i'j}, \quad (4.18)$$

where the operator $[S_\ell^z S_m^z]_{i'i'}$ has been calculated at the appropriate step; this is

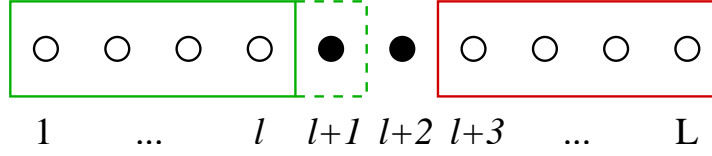


Figure 4.6: Superblock configuration relevant for the wave function transformation.

correct within the variational approximation for ψ_{ij} . The general rule is that compound operators internal to a block must be accumulated as the calculation proceeds. In this way, almost all correlation functions as well as more complicated equal-time expectation values can be calculated.

Recent developments have made the calculation of dynamical correlation functions possible. These extensions of the DMRG are usually referred to as *dynamical* DMRG (DDMRG), see Refs. [58, 133, 134, 135, 136]. In chapter 6 we discuss the extension of the DMRG for time-dependent quantities.

4.3.5 Wave Function Transformations

The most time-consuming part of the DMRG algorithm is the iterative diagonalization of the superblock Hamiltonian. Here we discuss how to optimize this procedure significantly by reducing the number of steps in the iterative diagonalization, in some cases by up to an order of magnitude.

As discussed in Sec. 3.1.2, the key operation and most time-consuming part of any iterative diagonalization procedure is the multiplication of the Hamiltonian and an arbitrary wave function, i.e., the operation $H^{\text{super}}\psi$ in the DMRG. Typically, of the order of 40-100 such multiplications are required to reach convergence. Reducing this number would thus directly lead to a proportional speedup of the diagonalization. If the Davidson or Lanczos procedure were started with a wavevector that is a good approximation to the desired wavevector, much fewer iterations would be required. Since an approximation to the same system is treated at each step of the finite system algorithm, an obvious starting point is the result $|\psi_0^\ell\rangle$ of a previous finite system step. However, this wave function is not in an appropriate basis for H^{super} because it was obtained using a different superblock configuration. In order to be able to perform the multiplication $H_{\ell+1}^{\text{super}}|\psi_0^\ell\rangle$, the wave function must be transformed from the basis at step ℓ to a basis suitable to describe the system configuration at step $\ell + 1$.

At step ℓ , a state in the superblock basis is given by

$$|\alpha_\ell s_{\ell+1} s_{\ell+2} \beta_{\ell+3}\rangle = |\alpha_\ell\rangle \otimes |s_{\ell+1}\rangle \otimes |s_{\ell+2}\rangle \otimes |\beta_{\ell+3}\rangle, \quad (4.19)$$

where $|\alpha_\ell\rangle$ is the basis of the left block containing sites $1, \dots, \ell$, $|s_{\ell+1}\rangle, |s_{\ell+2}\rangle$ are the bases of the single sites, $\ell + 1$ and $\ell + 2$, and $|\beta_{\ell+3}\rangle$ is the basis of the right block in the four-block description of the superblock, as depicted in Fig. 4.3.5. Assuming the algorithm is building up the system block from left to right, these states must be transformed to the configuration of the superblock at step $\ell + 1$ with basis

$$|\alpha_{\ell+1} s_{\ell+2} s_{\ell+3} \beta_{\ell+4}\rangle . \quad (4.20)$$

This transformation is performed in two steps. The left block is transformed from the original product basis $\{|\alpha_\ell\rangle \otimes |s_{\ell+1}\rangle\}$ to the effective density-matrix basis obtained at the end of the previous DMRG step, $\{|\alpha_{\ell+1}\rangle\}$ using

$$|\alpha_{\ell+1}\rangle = \sum_{s_{\ell+1}, \alpha_\ell} L^{\ell+1}[s_{\ell+1}]_{\alpha_{\ell+1}, \alpha_\ell} |\alpha_\ell\rangle \otimes |s_{\ell+1}\rangle . \quad (4.21)$$

The transformation matrix $L^{\ell+1}[s_{\ell+1}]_{\alpha_{\ell+1}, \alpha_\ell}$ contains the density-matrix eigenvectors $u_{s_{\ell+1} \alpha_\ell}^{\alpha_{\ell+1}}$ and is a simple rearrangement of the matrix elements of the transformation matrix $O_{s_{\ell+1} \alpha_\ell; \alpha_{\ell+1}}$ used in Eq. (4.14) for the transformation of operators to the new (truncated) density matrix basis. Similarly, for the right basis one defines

$$|\beta_{\ell+3}\rangle = \sum_{s_{\ell+3}, \beta_{\ell+4}} R^{\ell+3}[s_{\ell+3}]_{\beta_{\ell+3}, \beta_{\ell+4}} |s_{\ell+3}\rangle \otimes |\beta_{\ell+4}\rangle . \quad (4.22)$$

Transformation matrices similar to $L^{\ell+1}[s_{\ell+1}]_{\alpha_{\ell+1}, \alpha_\ell}$ and $R^{\ell+3}[s_{\ell+3}]_{\beta_{\ell+3}, \beta_{\ell+4}}$ were introduced by Östlund and Rommer in Ref. [137], where they show that the resultant wave function is a so called *matrix product state*.

To perform the wave function transformation needed for the left-to-right part of the DMRG, we expand the superblock wave function at step ℓ as

$$|\psi\rangle = \sum_{\alpha_\ell, s_{\ell+1}, s_{\ell+2}, \beta_{\ell+3}} \psi(\alpha_\ell, s_{\ell+1}, s_{\ell+2}, \beta_{\ell+3}) |\alpha_\ell s_{\ell+1} s_{\ell+2} \beta_{\ell+3}\rangle . \quad (4.23)$$

The basis transformation is formally performed by inserting $\sum_{\alpha_{\ell+1}} |\alpha_{\ell+1}\rangle \langle \alpha_{\ell+1}|$. Since there is a truncation, this is only an approximation,

$$\sum_{\alpha_{\ell+1}} |\alpha_{\ell+1}\rangle \langle \alpha_{\ell+1}| \approx 1 . \quad (4.24)$$

The coefficients of the wave function in the new basis therefore become

$$\begin{aligned} \psi(\alpha_{\ell+1}, s_{\ell+2}, s_{\ell+3}, \beta_{\ell+4}) &\approx \\ &\sum_{\alpha_\ell, s_{\ell+1}, \beta_{\ell+3}} L^{\ell+1}[s_{\ell+1}]_{\alpha_{\ell+1}, \alpha_\ell} \psi(\alpha_\ell, s_{\ell+1}, s_{\ell+2}, \beta_{\ell+3}) R^{\ell+3}[s_{\ell+3}]_{\beta_{\ell+3}, \beta_{\ell+4}} . \end{aligned}$$

It is convenient to perform the procedure in two steps:

1. Form the intermediate result

$$\psi(\alpha_{\ell+1}, s_{\ell+2}, \beta_{\ell+3}) = \sum_{\alpha_{\ell}, s_{\ell+1}} L^{\ell+1}[s_{\ell+1}]_{\alpha_{\ell+1}, \alpha_{\ell}} \psi(\alpha_{\ell}, s_{\ell+1}, s_{\ell+2}, \beta_{\ell+3}) . \quad (4.25)$$

2. Then form

$$\psi(\alpha_{\ell+1}, s_{\ell+2}, s_{\ell+3}, \beta_{\ell+4}) = \sum_{\beta_{\ell+3}} \psi(\alpha_{\ell+1}, s_{\ell+2}, \beta_{\ell+3}) R^{\ell+3}[s_{\ell+3}]_{\beta_{\ell+3}, \beta_{\ell+4}} . \quad (4.26)$$

An analogous transformation is used for a step in the right-to-left sweep.

The wave function transformations are relatively inexpensive in CPU time and in memory compared to other steps of the DMRG procedure. In addition to leading to faster convergence in the iterative diagonalization due to the good starting vector, wave function transformations also allow the convergence criterium of the Davidson or Lanczos algorithm to be relaxed so that the variational error in the iterative diagonalization is comparable to the variational error of the DMRG truncation, saving additional iterations. Normally such a relaxation would lead to the strong possibility of convergence to a qualitatively incorrect state. However, since the initial state comes from a diagonalization of the same finite lattice, there is little danger of this occurring.

Implementing this transformation requires saving the transformation matrices $\mathbf{L}[s_{\ell}]$ and $\mathbf{R}[s_{\ell}]$ at every finite-system step, which was not necessary in the original formulation of the algorithm. In an efficient implementation of the DMRG algorithm, the transformation matrices (as well as the matrices needed to describe blocks not currently needed) are stored on hard disk. This additionally makes it possible to reconstruct all operators *after* the final ground state wave function $|\psi_0\rangle$ has been obtained, which saves memory during the DMRG run when many measurements are made.

Chapter 5

Applying the DMRG: Susceptibilities and Correlation Functions of the Ionic Hubbard Model

5.1 Introduction

In this chapter, we apply the DMRG method discussed in the previous chapter and use it to clarify controversial issues on the quantum critical behavior of the so-called *ionic* Hubbard model (IHM). In particular, we focus on the strong-coupling phase. As discussed below, the phase is expected to be a Mott insulator, but, as the numerical calculation using the DMRG shows, with unexpected properties such as a *diverging* electrical susceptibility.

Theoretical studies of the IHM date back as far as the early seventies (see Ref. [138] and references therein). The model consists of the usual Hubbard model with on-site Coulomb repulsion U , Eq. (2.6), supplemented by an alternating one-particle potential of strength δ . It has been used to study the neutral to ionic transition in organic charge-transfer salts [139, 138] and to understand the ferroelectric transition in perovskite materials [140]. Based on results obtained from numerical [141, 142] and approximate methods [143, 144], it was generally believed that, at temperature $T = 0$ and for fixed δ , a single phase transition occurs if U is varied. This quantum phase transition was also interpreted as an insulator-insulator transition from a band insulator ($U \ll \delta$) to a correlated insulator ($U \gg \delta$). In 1999, Fabrizio, Gogolin, and Nersesyan used bosonization to derive a field-theoretical model which they argued to be the effective low-energy model of the one-dimensional IHM [12]. Surprisingly, the authors found, us-

ing various approximations, that the field-theoretical model displays *two* quantum critical points as U is varied for fixed δ . For $U < U_{c1}$ the system is a band insulator (with finite bosonic spin and charge gaps), as expected from general arguments. At the first transition point U_{c1} , they found Ising critical behavior as well as metallic behavior in the sense that the gap to the bosonic charge modes goes to zero at the critical point only. In the intermediate regime, $U_{c1} < U < U_{c2}$, a spontaneously dimerized insulator phase (in which the bosonic spin and charge gaps are finite) was found. In this phase, the bond order (BO) parameter, which is the ground-state expectation value of the staggered kinetic energy per bond (for details see below), is finite. The authors argued that the system goes over into a correlated insulator phase (in which the bosonic charge gap is finite) with vanishing bond order and spin gap at a second critical point U_{c2} which is of Kosterlitz-Thouless (KT) type. Several groups have attempted to verify this phase diagram for the IHM using mainly numerical methods. Variational and Green function Quantum Monte Carlo (QMC) data obtained for the BO parameter, the electric polarization, and the localization length were interpreted in favor of a scenario with a single critical point U_c and finite BO for $U > U_c$ [145]. In a different calculation using auxiliary-field QMC, data for the one-particle spectral weight were argued to show two critical points with an intermediate metallic phase [146]. Exact diagonalization studies of the Berry phase [147] and energy gaps [148, 149, 150] have been interpreted as favoring one critical point [149] or two points [147]; in two investigations this issue was left unresolved [148, 150]. Several DMRG studies have been performed focusing on different energy gaps, the localization length, the BO parameter, the BO correlation function, different distribution functions, and the optical conductivity [151, 152, 150, 153]. Some of the results have been interpreted to be consistent with a two-critical-point scenario [151, 152, 153]. In Ref. [150] the signature of only one phase transition was found and the possible existence of a second transition was left undetermined. The phase diagram of the IHM has also been studied using approximate methods such as the self-consistent mean-field approximation [154, 155, 156], the slave-boson approximation [154], and a real space renormalization group method [155]. Although these studies led to interesting insights, the validity of the approximations in the vicinity of the critical region can be questioned on general grounds.

In this chapter, we discuss the $T = 0$ phase diagram of the one-dimensional IHM as discussed in detail in Ref. [129]. The results presented are mainly based on DMRG calculations on systems with both open and periodic boundary conditions (OBC's and PBC's).

We have calculated a number of different energy gaps, including the spin gap, the one-particle gap (the energy difference of ground states with $N + 1$, N , and $N - 1$ electrons), and the gaps to the first (in the literature sometimes referred to as “excitonic gap”) and second excited states. As discussed in Refs. [129, 157],

different gaps associated with charge degrees of freedom do not coincide in the thermodynamic limit, although they are often believed to in the literature (see also Refs. [150] and [152]). In order to obtain a comprehensive picture of the ground-state phase diagram, we have studied the different phases (as a function of U) for different δ 's which cover a wide range of the parameter space. We consider the limit of large Coulomb repulsion $U \rightarrow \infty$ (for fixed δ and hopping matrix element t) and show that some aspects of the physics of the model in this limit can be understood in terms of an effective Heisenberg model, as has been suggested earlier [138] but has been questioned in Ref. [150]. As a result of our investigations, we are able to resolve many of the controversial issues discussed in the literature and present indications in favor of a scenario with two quantum critical points and a strong coupling phase with peculiar properties.

5.1.1 Model and exactly solvable limits

The one-dimensional IHM is given by the Hamiltonian

$$H = -t \sum_{j,\sigma} (c_{j\sigma}^\dagger c_{j+1\sigma} + \text{h.c.}) + U \sum_j n_{j\uparrow} n_{j\downarrow} + \frac{\delta}{2} \sum_{j,\sigma} (-1)^j n_{j\sigma}, \quad (5.1)$$

where $c_{j\sigma}$ ($c_{j\sigma}^\dagger$) destroys (creates) an electron with spin σ on lattice site j and $n_{j\sigma} = c_{j\sigma}^\dagger c_{j\sigma}$. We set the lattice constant equal to 1 and denote the number of lattice sites by L . Here we study the properties of the half-filled system with $N = L$ electrons. The system corresponds to the usual Hubbard model with an additional local alternating potential. It is useful to consider various limiting cases in order to gain insight into possible phases and phase transitions. For $U = 0$ and $\delta > 0$, the model describes a conventional band insulator with a band gap δ . Since the alternating one-particle potential explicitly breaks the one-site translational symmetry, the ground state has finite ionicity. The one-dimensional half-filled Hubbard model without the alternating potential ($\delta = 0$) and with $U > 0$ describes a correlated insulator with vanishing spin gap $\Delta_s^{\text{HM}}(U)$ and critical spin-spin and bond-bond correlation functions [158]. All gaps associated with the charge degrees of freedom, such as the one-particle gap $\Delta_1^{\text{HM}}(U)$, are finite [47]. The ionicity and the dimerization are zero for all values of U . These two limiting cases suggest that the system will be in two qualitatively different phases in the limits $U \ll \delta$ and $U \gg \delta$.

In the atomic limit, $t = 0$, for $0 < U < \delta$ and at temperature $T = 0$, every second site of the lattice with on-site energy $-\delta/2$ (A sites) is occupied by two electrons, while the sites with energy $\delta/2$ (B sites) are empty. The energy difference between the ground state and the highly degenerate first excited state is $\delta - U$.

For $U > \delta$, both the A and B sites are occupied by one electron and the energy gap is $U - \delta$. Thus for $t = 0$ a single critical point $U_c(\delta) = \delta$ with vanishing excitation gap can be found. One expects similar critical behavior with at least one critical point to persist for the full problem with finite t .

To describe the physics of the IHM in the limit $U \gg t, \delta$, an effective Heisenberg Hamiltonian

$$H_{\text{HB}} = J \sum_j \left(\mathbf{S}_j \cdot \mathbf{S}_{j+1} - \frac{1}{4} \right), \quad J = \frac{4t^2 U}{U^2 - \delta^2} \quad (5.2)$$

was derived in Ref. [138] analogously to the strong-coupling perturbation expansion of the usual Hubbard model [29]. It has been pointed out that this strong-coupling mapping does not take into account an explicitly broken one-site translational symmetry [150]. However, it was shown in Ref. [138] that the strong-coupling expansion preserves the one-site translation symmetry in the effective spin Hamiltonian to *all* orders in the strong-coupling expansion. In addition, the ionicity can be derived directly from the effective spin Hamiltonian as follows. The symmetry of the Hamiltonian [Eq. (5.1)] implies that, after taking the thermodynamic limit, $n_{j\sigma} = n_{j+2\sigma}$ for $\sigma = \uparrow, \downarrow$ and all j . Using the Hamiltonian Eq. (5.1) and the Hellman-Feynman theorem [64], the ionicity

$$\langle n_A - n_B \rangle = -\frac{2}{L} \sum_{j,\sigma} (-1)^j \langle n_{j\sigma} \rangle \quad (5.3)$$

can be determined via

$$\langle n_A - n_B \rangle = -\frac{4}{L} \left\langle \frac{\partial H}{\partial \delta} \right\rangle = -\frac{4}{L} \frac{\partial E_0}{\partial \delta}. \quad (5.4)$$

The ground-state energy E_0 of the effective Heisenberg model [Eq. (5.2)] is known analytically [15] and, in terms of U and δ , is given by

$$E_0^{\text{HB}} = L \frac{4Ut^2}{U^2 - \delta^2} \left(\ln 2 - \frac{1}{4} \right) \quad (5.5)$$

in the thermodynamic limit. In the limit $U \gg \delta$, we can thus derive an analytic expression for the ionicity

$$\langle n_A - n_B \rangle = 32 \ln 2 \frac{U\delta t^2}{(U^2 - \delta^2)^2}. \quad (5.6)$$

Eq. (5.6) implies that for any $U < \infty$, the ionicity of the IHM is nonzero and, for

large U , vanishes as $1/U^3$. Since CDW order is explicitly favored by the Hamiltonian, it is not surprising that the ionicity is non-vanishing for all finite U . As will be shown in Sec. 5.3, this expression shows excellent agreement with our DMRG data for the IHM. This gives us confidence that the effective Heisenberg model indeed gives correctly at least certain aspects of the low-energy physics. Since the Heisenberg model [Eq. (5.2)] has a vanishing spin gap [159], the mapping suggests that the spin gap also vanishes in the large- U limit of the IHM.

Although the alternating potential breaks the one-site translational symmetry explicitly, the model remains invariant to a translation by two lattice sites. This leads to a site-inversion symmetry for closed-chain geometries with periodic or antiperiodic boundary conditions, a symmetry which is not present for open boundary conditions (OBC). As pointed out in Ref. [148], the ground state of the effective Heisenberg model with periodic boundary conditions for systems with $4n$ lattice sites or antiperiodic boundary conditions for systems with $4n + 2$ sites has a parity eigenvalue of -1 whereas the ground state for $U = 0$ has a parity eigenvalue of $+1$. This suggests that the IHM undergoes at least one phase transition with increasing U for fixed δ . This level crossing will be replaced by level repulsion and approximate symmetries for other boundary conditions [160]. In the thermodynamic limit, the effect of the boundaries will disappear and the level repulsion becomes vanishingly small. It is important to point out, however, that a level crossing on small finite systems does not necessarily lead to a first-order transition in the thermodynamic limit; careful finite-size scaling must be carried out in order to determine the critical behavior.

From these considerations, one expects to find at least one quantum phase transition from a phase with physical properties similar to those of a non-interacting band insulator to a phase with properties similar to those of the strong-coupling phase of the ordinary Hubbard model. However, the details of the transition and the physical properties of the different phases remain unclear from these arguments. In particular, as will be demonstrated below, the strong coupling phase in some aspects differs significantly from the expected behavior. Furthermore, the magnitude of the BO parameter in the critical region cannot be estimated from these simple limiting cases. Therefore, a detailed and careful calculation of the characterizing gaps and order parameters is necessary. Since no direct analytic approach is known to be able to treat the parameter values in the critical regime, we restrict ourselves to numerical calculations using the DMRG method, with the details described in the next section.

In the following, we measure energies in units of the hopping matrix element t , i.e., set $t = 1$. In order to be able to cover a significant part of the parameter space, we have carried out calculations with $\delta = 1$, $\delta = 4$, and $\delta = 20$ for weak interaction values $U \ll \delta$, for strong coupling $U \gg \delta$ and in the intermediate critical regime $U \approx \delta$. Results for $\delta = 1$ have been discussed in Ref. [157]. Here,

we will mostly focus on $\delta = 20$, where the results are much clearer to interpret than for $\delta = 1$. The results presented are generic to all three δ -regimes.

5.1.2 Details to the Application of the DMRG

We have carried out our calculations using the finite-system DMRG algorithm discussed in Sec. 4.3.2. Our investigation focuses on the ground-state properties for systems with OBC's, i.e., we have performed DMRG runs mostly with OBC's and one target state, the case in which the DMRG algorithm is most efficient. In order to perform the demanding finite-size scaling necessary, we have performed calculations for systems with up to $L = 768$ sites.

In order to investigate the low-lying excitations, we have also performed calculations targeting up to three states simultaneously on systems with OBC's. These numerically more demanding calculations were carried out for systems with up to $L = 256$ sites for three target states and with up to $L = 450$ sites for two target states. In order to compare with exact diagonalization calculations and to extend its finite-size scaling to larger systems, we have performed calculations for PBC's with up to $L = 64$ sites and one to three target states. In this case, the maximum system size is limited by the relatively poor convergence.

The DMRG calculations for OBC's with one target state were carried out by performing up to six finite-system sweeps keeping up to $m = 800$ states. For calculations with multiple states and with PBC's up to 12 sweeps were performed, keeping up to $m = 900$ states. In order to test the convergence of the DMRG runs, the sum of the discarded density-matrix eigenvalues and the convergence of the ground-state energy were monitored. For OBC's, the discarded weight was of order 10^{-6} for the worst case, and the ground-state energy was converged to an absolute error of 10^{-3} , but in most cases the absolute error was 10^{-5} or better. This accuracy in both the energy and the discarded weight gives us confidence that the wave function is also well-converged and that local quantities are quite accurate.

For PBC's, the discarded weight was of the order 10^{-5} in the worst case, and the ground-state energy for most runs was converged up to an absolute error of 10^{-3} or better, but for extreme cases such as $L = 64$ and three target states for parameter values near the phase transition points, the convergence in the energy was sometimes reduced to an absolute error of only 10^{-1} . However, we believe that this accuracy is high enough for the purposes of the discussion sketched in the following sections.

In general, we find that our data are sufficiently accurate so that extrapolation in the number of states m kept in the DMRG procedure does not bring about significant improvement in the results (at least for OBC's). Details of the extrapolations and error estimates for particular calculated quantities are given in the

corresponding sections.

5.2 Energy gaps

One important way to characterize the different phases of the IHM is via the energy differences between many-body eigenstates. Gaps to excited states can be used to characterize phases by making contact with the gaps obtained in bosonization calculations and also form the basis for experimentally measurable excitation gaps, found, for example, in inelastic neutron scattering, optical conductivity, or photoemission experiments. In addition to the gaps themselves, however, matrix elements between ground and excited states as well as the density of excited states are important in forming the full experimentally relevant dynamical quantities. An example is the matrix element of the current operator that comes into calculations of the optical conductivity. The behavior of the matrix elements for the dynamical spin and charge structure factors and for the optical conductivity using exact diagonalization on systems with both PBC's and OBC's has been investigated and discussed in Ref. [157] and is not part of this thesis.

In this section, we study excitations between a non-degenerate $S = 0$ ground state and various excited states. In the numerical calculations, we have found that for OBC's the ground state is non-degenerate with total spin $S = 0$ for all parameter values studied here. We define the ‘‘exciton’’ gap (following the nomenclature of Ref. [152])

$$\Delta_E = E_1(N, S) - E_0(N, S = 0) \quad (5.7)$$

as the gap to the first excited state in the sector with the same particle number N and with *arbitrary* spin S , but with the z -component of the total spin $S_z = 0$. We also calculate the expectation value of the total spin operator $\langle \mathbf{S}^2 \rangle$ so that S is known.

The spin gap is defined as the energy difference between the ground state and the lowest lying energy eigenstate in the $S = 1$ subspace

$$\Delta_S = E_0(N, S = 1) - E_0(N, S = 0). \quad (5.8)$$

The first excited state $E_1(N, S)$ in the $S_z = 0$ subspace is a spin triplet with $S = 1$, $\Delta_S = \Delta_E$. Within the DMRG, this gap can be calculated by determining the ground-state energies in different S_z subspaces in two different DMRG runs.

If $\Delta_E < \Delta_S$, we *call* the lowest excitation a charge excitation. In fact, exact diagonalization calculations for system with PBC's suggest that the gap Δ_E corresponds to the gap in the optical conductivity [150]. We have carried out additional exact diagonalization calculations that show that the corresponding matrix ele-

ments of the current operator are also nonzero for OBC's. We therefore expect that Δ_E (for excitations with $S = 0$ and when $\Delta_E < \Delta_S$) corresponds to the optical gap in the thermodynamic limit [157].

In the literature, gaps to excitations which can be classified as charge excitations are often calculated by considering differences in the chemical potential when changing the particle number. This can be obtained by calculating differences between ground-state energies in sectors with different numbers of particles (this gap is commonly called the “charge gap”). In particular, one can define a p -particle gap

$$\Delta_p = \left[E_0(N + p, S_{\min}^z) + E_0(N - p, S_{\min}^z) - 2E_0(N, S = 0) \right] / p \quad (5.9)$$

which is essentially the difference in chemical potential for adding and subtracting p particles to the system with N particles. The spin S_{\min}^z is the minimal value, $1/2$ or 0 for p odd and even, respectively. Either the one-particle gap Δ_1 or the two-particle gap Δ_2 are commonly used. The calculation of Δ_1 or Δ_2 is numerically less demanding than that of Δ_E since it is sufficient to calculate the ground-state energies in the subspaces with the corresponding particle numbers. However, since these gaps involve changing the particle number and, for $p = 1$, the spin quantum number, it is not a priori clear if they can be used to characterize possible phase transition points of the N -particle system. Consider, e.g., $p = 1$; in this case, the gap considers simultaneously charge excitations and excitations to states with $S_z = 1/2$. Thus, it can not be used to analyze if, at a certain critical point, only spin or only charge degrees of freedom become critical, a phenomenon that, however, is predicted for the IHM by the bosonization calculation presented in Ref. [12]. In addition, it is, indeed, found that in many cases of interest the difference between Δ_1 , Δ_2 , and Δ_E vanishes for $L \rightarrow \infty$, but in other systems (an example is the Hubbard chain with an attractive interaction), their behavior differs. As we shall see, Δ_1 and Δ_E do behave differently near U_{c1} .

Gaps are also used to characterize the phase diagram within the bosonization approach [12, 150]. It is generally believed that the bosonic charge gap defined there can be identified with the gap to the first excited state with spin quantum number $S = 0$, i.e. the exciton gap Δ_E , Eq. (5.7), as long as $\Delta_E < \Delta_S$, and the bosonic spin gap with Δ_S , Eq. (5.8), although a formal proof is missing. Based on Δ_E , Δ_S , and Δ_{SE} and the very limited knowledge about matrix elements due to the small system sizes available to exact diagonalization, no reliable characterization of the metallic or insulating behavior of different phases and transition points can be given.

The finite size extrapolation of the gaps is discussed in detail in Refs. [157, 129] and is not further considered here. Fig. 5.1 summarizes our findings. The plot shows the extrapolated spin gap for $\delta = 20$ presented together with the extrap-

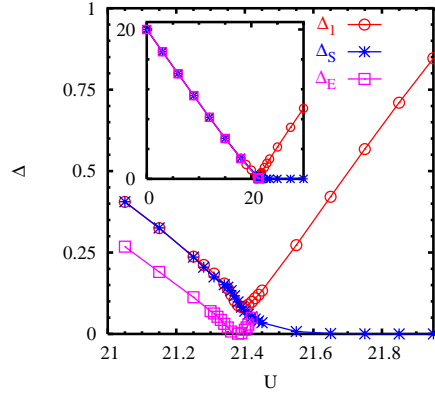


Figure 5.1: The exciton gap Δ_E , the spin gap Δ_S , and the one-particle gap Δ_1 for $\delta = 20$ after extrapolating to the thermodynamic limit $L \rightarrow \infty$. The inset shows the result for a larger range of U .

olated values for Δ_1 and Δ_E . All three gaps are approximately equal for $U \ll U_{c1}$ (see the inset). Close to the transition, as can be seen on the expanded scale in the main plot, Δ_E goes to zero at U_{c1} , while Δ_S and Δ_1 stay finite and are (almost) equal. We find a region of $U > U_{c1}$ in which $\Delta_S(L = \infty)$ has a value that is clearly nonzero, well above the accuracy of the data, which is of the order of the symbol size. The behavior is similar for $\delta = 4$ (not shown). For even smaller values of δ , Δ_S close to U_{c1} becomes significantly smaller. As a consequence, the region in which Δ_S is non-vanishing for $U > U_{c1}$ is less pronounced at $\delta = 1$. In this case, Δ_S at U_{c1} is only a factor of six larger than the estimated accuracy of our data (this should be compared to the factor of 20 for $\delta = 4$ and 40 for $\delta = 20$) with a fast decrease for $U > U_{c1}$. We take the estimate of accuracy from comparison of DMRG calculations for the one-particle gap of the usual 1D Hubbard model with Bethe ansatz results. We find that as obtained in Ref. [157], the difference is about $|\Delta_1^{\text{HM,DMRG}} - \Delta_1^{\text{HM,exact}}| = 0.003$ in the worst case. We therefore interpret this small spin gap to be finite for $\delta = 1$ and in a small region of $U \geq U_{c1}$. For δ substantially smaller than 1, it is impossible to resolve a non-vanishing Δ_S at $U \geq U_{c1}$ using the DMRG.

The spin gap data in Fig. 5.1 indicate that Δ_S goes to zero very smoothly between 21.55 and 21.8 and remains zero from there on. We here define U_{c2} as the coupling at which Δ_S goes to zero. As we have argued in Sec. 5.1.1, the mapping onto a Heisenberg model at strong coupling [Eq. (5.2)] suggests that the spin gap should vanish at sufficiently large U . However, we cannot strictly speaking exclude that $U_{c2} = \infty$ from the spin-gap data. However, we will give

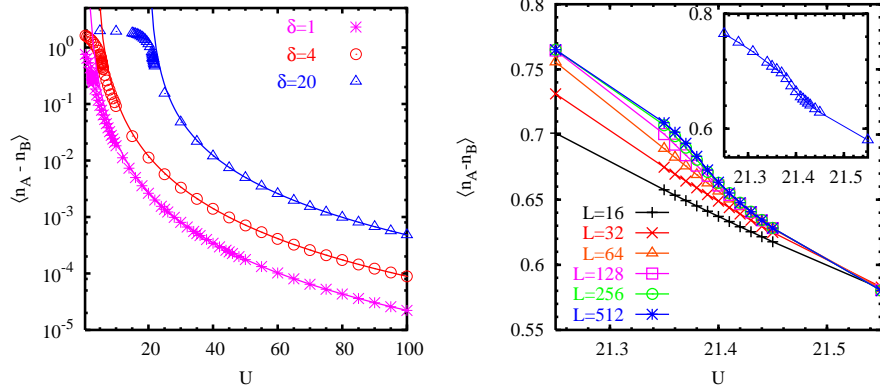


Figure 5.2: Left plot: the ionicity $\langle n_A - n_B \rangle$ for $\delta = 1, 4, 20$. The solid lines indicate analytical results from Eq. (5.6) and the symbols numerical DMRG results for $L = 32$ sites. Right plot: The ionicity for finite systems with $L = 16, 32, \dots, 512$ for $\delta = 20$. The inset shows the $L \rightarrow \infty$ extrapolated value.

further evidence in support of two transition points at finite U below.

To summarize the behavior of the finite-size extrapolated gaps, we find that for $U \ll U_{c1}$, $\Delta_E = \Delta_S = \Delta_1$ as in a non-interacting band insulator. As U_{c1} is approached, the gaps to two (or more) $S = 0$ excitations drop below Δ_S and at least one of them goes to zero at U_{c1} . The one-particle gap Δ_1 reaches a finite minimum around U_{c1} and then increases (linearly for large U), and the spin gap Δ_S goes to zero smoothly at $U_{c2} > U_{c1}$. This smooth decay of the spin gap makes it difficult to quantitatively estimate U_{c2} . Since the above behavior is similar for the widely different potential strengths studied here, $\delta = 1, 4$, and 20 , we believe that it is generic for *all* δ .

5.3 Ionicity

As argued in Sec. 5.1.1, the effective strong-coupling model (5.2) predicts that the ionicity $\langle n_A - n_B \rangle \sim 1/U^3$ for large U . For $t = 0$, on the other hand, one expects a discontinuous jump from $\langle n_A - n_B \rangle = 2$ to $\langle n_A - n_B \rangle = 0$ at the single transition point U_c . Here we explore the behavior of $\langle n_A - n_B \rangle$ for all U calculated within the DMRG.

In Fig. 5.2 we compare Eq. (5.6) for $\delta = 1, 4, 20$ and various U to results obtained from DMRG with OBC's and $L = 32$. By also considering larger system sizes (up to $L = 512$) and PBC's (up to $L = 64$), we have verified that the $L = 32$

results shown are already quite close to the thermodynamic limit for $U \gg \delta$. On the scale of the figure the difference between $L = 32$ and $L = \infty$ is negligible. For large U , the DMRG data agree quite well with the analytical prediction, Eq. (5.6). This gives a strong indication that the large- U mapping of the IHM onto an effective Heisenberg model [138] is applicable at large but finite U . It is therefore tempting to conclude that $U_{c2} < \infty$. One should nevertheless keep in mind that the excellent agreement of the numerical data with the analytical prediction for the ionicity does not constitute a proof of this statement.

The DMRG data for $\langle n_A - n_B \rangle$ for $L = 32$ shown in Fig. 5.2 are continuous as a function of U for all U . We examine $\langle n_A - n_B \rangle$ more carefully as a function of system size in the vicinity of the first phase transition at U_{c1} for $\delta = 20$ in the right plot of Fig. 5.2. The main plot shows DMRG data for various L as a function of U for $\delta = 20$. While the data are continuous as a function of U for all sizes, there is significant size dependence between $U = 21.2$ and 21.5 , near the first critical point at U_{c1} . We have extrapolated the data to the thermodynamic limit using a second order polynomial in $1/L$ and have checked that other extrapolation schemes do not lead to significant differences in the extrapolated values. The $L = \infty$ extrapolated curve is shown in the inset. While the curve is still continuous, an inflection point can be observed close to U_{c1} . This might be related to non-analytic behavior at U_{c1} . For $\delta = 1$ and 4 , we find that $\langle n_A - n_B \rangle$ behaves similarly.

5.4 Order parameters and susceptibilities

5.4.1 The bond order parameter and susceptibility

The energy gaps have given us indications for two critical points. To study the nature of the intervening phase and the possibility of dimerization in more detail, we calculate the BO parameter

$$\langle B \rangle = \frac{1}{L-1} \sum_{j,\sigma} (-1)^j \langle c_{j+1\sigma}^\dagger c_{j\sigma} + c_{j\sigma}^\dagger c_{j+1\sigma} \rangle . \quad (5.10)$$

This quantity has been used to characterize dimerized phases in other models, e.g., the frustrated Heisenberg chain investigated in Ref. [126]. Since the OBC's break the symmetry between even and odd bonds, $\langle B \rangle \neq 0$ for all finite systems. Therefore, a spontaneous dimerization can be obtained directly by extrapolating $\langle B \rangle$ to $L \rightarrow \infty$, i.e., without adding a symmetry-breaking field explicitly. One can form the corresponding BO susceptibility χ_{BO} by adding a term

$$H_{\text{dim}} = \rho \sum_{j,\sigma} (-1)^j (c_{j+1\sigma}^\dagger c_{j\sigma} + c_{j\sigma}^\dagger c_{j+1\sigma}) \quad (5.11)$$

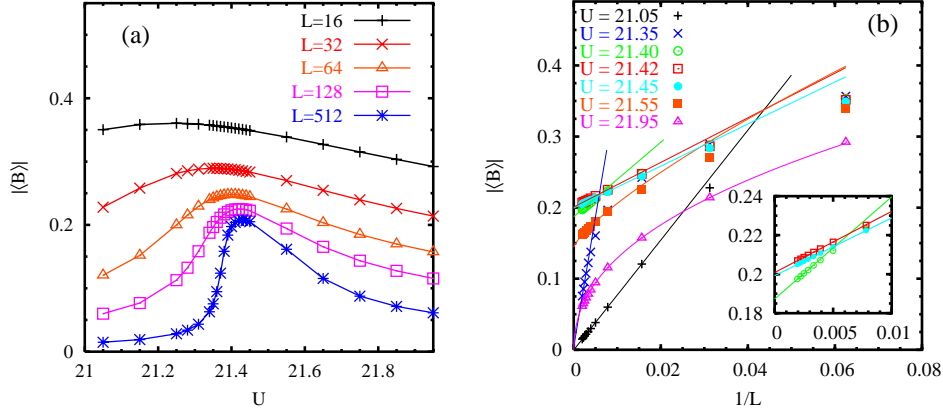


Figure 5.3: (a) The bond order parameter $\langle B \rangle$ for $\delta = 20$ for finite systems as a function of U for various system sizes. (b) The scaling of the data as a function of the inverse system size $1/L$. The solid lines are least-squares fits to the data as described in the text. The inset shows an expanded view of the scaling for U values near the critical point.

to the Hamiltonian (5.1) and taking

$$\chi_{\text{BO}} = \left. \frac{\partial \langle B \rangle(\rho)}{\partial \rho} \right|_{\rho=0}. \quad (5.12)$$

In practice, the derivative is discretized as $[\langle B \rangle(\rho) - \langle B \rangle(-\rho)]/(2\rho)$ where ρ is taken to be small enough so that the system remains in the linear response regime (close to a critical point, the linear response regime shrinks and very small amplitudes of the external field are required).

Fig. 5.3(a) shows $\langle B \rangle$ as a function of U for $\delta = 20$ and different L . The same detailed analysis for $\delta = 1$ was performed in Ref. [157]. A similar picture was found, but the situation remains less clear than for the case with $\delta = 20$. Thus, we focus in this section on the latter case. The data develop a well-defined maximum near U_{c1} for large L . The width of the “peak” for $L = 512$ gives a first indication that there is a region in which the dimerization is non-vanishing. Typical results for the finite-size scaling of $\langle B \rangle$ are presented in Fig. 5.3(b). For $U \ll U_{c1}$, the data extrapolate linearly to zero in $1/L$. In the opposite limit, $U \gg U_{c1}$, we find $\langle B \rangle \sim 1/L^\kappa$ with $\kappa \approx 0.5 - 0.6$. A similar slow decay of the BO parameter has also been found in the standard and extended Hubbard models at half-filling [161]. The substantial finite-size corrections thus require very large systems to distinguish between scaling to zero with a slow power-law and scaling to a finite $L \rightarrow \infty$ limit. Below, but close to U_{c1} , the data for small L initially

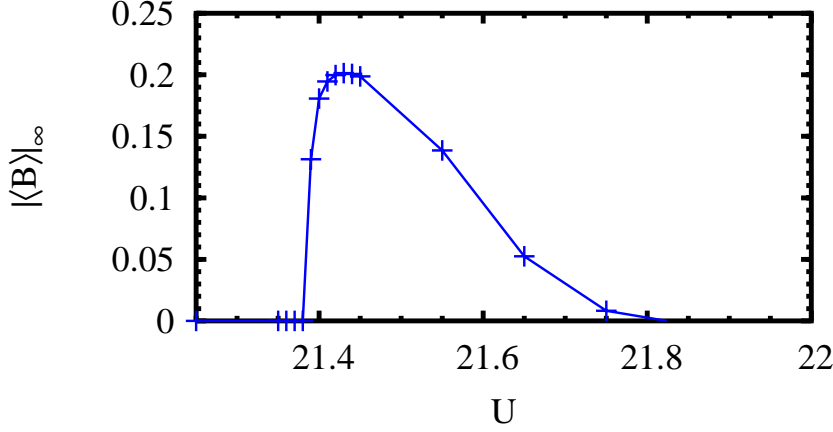


Figure 5.4: The bond-order parameter $\langle B \rangle_\infty$ in the thermodynamic limit $\delta = 20$ plotted as a function of U near the transition points.

display power-law-like finite-size scaling with $\kappa < 1$, but for larger system size, one finds a crossover to a linear scaling of the BO parameter (to zero) as $L \rightarrow \infty$. There is also a crossover in the behavior for U -values near, but above U_{c1} . One again finds a crossover from a power law with $\kappa < 1$ for smaller system sizes to linear behavior that can be extrapolated to finite values of $\langle B \rangle_\infty$ for larger system sizes. The crossover length scale increases as U approaches U_{c1} until it becomes larger than the largest system size considered here. This length scale L_c can be used to estimate the correlation length, which diverges at the first (continuous) critical point. We have been able to calculate L_c for U values on both sides of U_{c1} and find that it diverges approximately linearly in $|U - U_{c1}|$. This implies $\nu_1 = 1$ (see also below). Taking into account that $z_1 \nu_1 = 1$, as extracted from the linear closing of Δ_E [129], one finds $z_1 = 1$ for the dynamical critical exponent.

This diverging crossover length scale makes it essential to treat system sizes that are significantly larger than the scale L_c (which we associate with the correlation length); especially when close to the critical point U_{c1} , one has to consider in detail results for system sizes much larger than treated before. In order to obtain reliable results, we have calculated $\langle B \rangle_L$ for a number of system sizes $L > 200$. In carrying out the finite-size extrapolation, we fit to a linear form for the largest system sizes if it is clear that L_c has been reached, as can be seen in the inset of Fig. 5.3(b).

In Fig. 5.4, the finite-size extrapolation $\langle B \rangle_\infty$ is shown as a function of U for $\delta = 20$. As can be seen, $\langle B \rangle_\infty = 0$ to well within the error of the extrapolation for $U < U_{c1}$. For $U > U_{c1}$, we find a region of width ≈ 0.4 in U in which

$\langle B \rangle_\infty$ is distinctly finite. We find that the onset of finite $\langle B \rangle_\infty$ at U_{c1} is rather steep for all three values of δ , but seems to be continuous [129]. This steep onset suggests a critical exponent β of the order parameter that is substantially smaller than 1. Within bosonization the first critical point was predicted to be Ising-like with $\beta_1 = 1/8$ [12]. The fall-off to zero as U increases, on the other hand, is slow, with a small or vanishing slope. This behavior would be consistent with a second critical point at which the critical exponent for the order parameter is larger than one or at which a higher order phase transition such as a Kosterlitz-Thouless transition takes place [12]. As discussed in Ref. [129], the height of the maximum increases with increasing δ . For δ significantly smaller than 1, the BO parameter is so small that it cannot be concluded to be finite within the numerical accuracy of the DMRG. For the couplings at which the finite dimerization sets in we obtain $U_{c1}(\delta = 20) \approx 21.39$ and $U_{c1}(\delta = 4) \approx 5.61$, which are in excellent agreement with the results obtained from the vanishing of Δ_E . The value obtained for $\delta = 1$, $U_{c1}(\delta = 1) \approx 2.67$, is also in reasonably good agreement with the results obtained from the analysis of the gaps.

While our data suggest that a critical coupling \tilde{U}_{c2} , with $\langle B \rangle_\infty = 0$ for $U > \tilde{U}_{c2}$, exists, no reliable quantitative estimate of \tilde{U}_{c2} can be given based on the DMRG data for the BO parameter. Due the close proximity of the two critical points, we were not able to obtain quantitative results for the critical exponents β_1 and β_2 at the critical points, either by a direct fit of the $L = \infty$ results or by a scaling plot of the finite-size data. As discussed next, accurate exponents at U_{c1} can be extracted from both the BO and the electric susceptibilities, and a more accurate estimate of \tilde{U}_{c2} can be obtained from the BO susceptibility.

In order to understand the behavior of the BO susceptibility, it is useful to first examine the behavior of the BO parameter $\langle B \rangle$ as a function of the applied dimerization field ρ . From the ρ -dependence of $\langle B \rangle$ it becomes also apparent that following the standard procedure of first applying a finite ρ , then taking $L \rightarrow \infty$, and afterwards $\rho \rightarrow 0$ will lead to the same results for the BO parameter as presented in Fig. 5.4. In Fig. 5.5 $\langle B \rangle(\rho)$ is shown for $\delta = 20$, three representative values of U , and different system sizes. For $U = 19 < U_{c1}$, the system is in a phase with vanishing BO parameter, and the slope at $\rho = 0$ remains finite for all system sizes, corresponding to a finite susceptibility. The value $U = 21.42$ is in the intermediate regime where we have found a finite BO parameter in the thermodynamic limit. As can be seen in the main part of the figure, a jump in $\langle B \rangle(\rho)$ then develops. As the system size increases, the absolute value of dimerization field at which the jump occurs becomes smaller. This is the behavior expected in a dimerized phase in a system with OBC's. Therefore, the jump in $\langle B \rangle(\rho)$ provides additional evidence in support of an intermediate phase with finite dimerization. For the approximate calculation of the susceptibility $\chi_{BO} \approx [\langle B \rangle(\rho) - \langle B \rangle(-\rho)]/(2\rho)$, we have taken $\rho = 10^{-4}$, which is small enough to stay to the right of the jump for

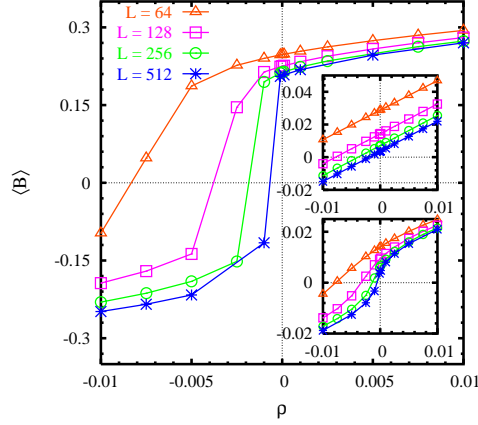


Figure 5.5: The BO parameter $\langle B \rangle$ as a function of applied dimerization field ρ for $\delta = 20$ and $U = 21.42$. The upper inset shows data for $U = 19$ and the lower inset data for $U = 50$.

all system sizes considered. Finally, for $U = 50 \gg U_{c2}$, $\langle B \rangle(\rho)$ goes to zero for $|\rho| \rightarrow 0$ and increasing system size consistent with the behavior in a phase without spontaneous dimerization. However, the slope at small $|\rho|$ becomes steeper with increasing system size, indicating a divergence of χ_{BO} .

In Fig. 5.6, the BO susceptibility as a function of U is shown for $\delta = 1, 4, 20$ and different L . For all δ values, one observes a two-peak structure that becomes progressively better defined with increasing system size. There is a narrow peak at a U -value that agrees well with U_{c1} determined earlier, and whose height grows rapidly with system size. It signals the onset of spontaneous dimerization. For somewhat larger U there is a minimum in χ_{BO} , surrounded by a narrow region in which its value saturates with system size. To demonstrate this more clearly, the finite-size scaling for a representative U located in the dip region is shown for each δ in Fig. 5.6(d). For still larger U values, a second, broad peak develops. The position of this second maximum is roughly at \tilde{U}_{c2} , the U -value at which the BO parameter vanishes. We argue that the second peak is related to the second phase transition from the dimerized phase into an undimerized phase. To the right of the second peak, χ_{BO} does not seem to saturate for increasing system size, implying that χ_{BO} is divergent for all $U \geq U_{c2}$. One can understand this divergent behavior by studying the BO susceptibility for the ordinary Hubbard model $\chi_{\text{BO}}^{\text{HM}}$. One finds that $\chi_{\text{BO}}^{\text{HM}}$ is divergent for all $U > 0$ because the bond-bond correlation function is critical [158]. A finite-size extrapolation of χ_{BO} is shown in Fig. 5.7 for large U values for both $\delta = 0$ and $\delta = 20$. We find a power-law divergence, $\chi_{\text{BO}}(L) \sim L^\zeta$, with $\zeta \approx 0.68$ for the ordinary Hubbard model and $\zeta \approx 0.65$ for the IHM. These

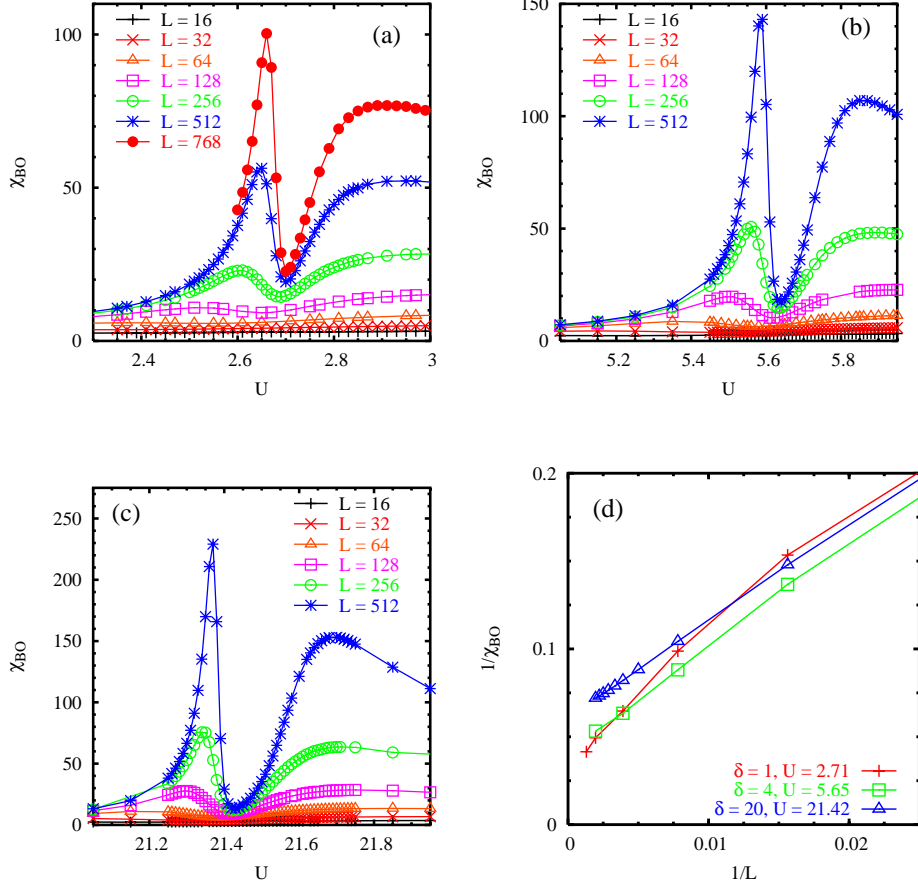


Figure 5.6: The BO susceptibility χ_{BO} as a function of U for (a) $\delta = 1$, (b) $\delta = 4$, and (c) $\delta = 20$ and different L . (d) Finite-size scaling of χ_{BO} for a U located in the dip region of (a)-(c).

values are in good agreement with each other, considering the accuracy of the fit and additional finite-size effects. This similarity between the strong coupling phase of the ordinary HM and of the IHM indicates that one is confronted with a critical phase for $U \geq U_{c2}$, in agreement with the expectations for a KT-type transition at U_{c2} .

Since χ_{BO} diverges for all U to the right of the second peak, it is difficult to accurately determine the critical coupling \tilde{U}_{c2} . However, two different ways of estimating $\tilde{U}_{c2}(\delta)$ under- and overestimate its value. In the first method, \tilde{U}_{c2} is estimated as the lowest U value for which χ_{BO} seems to diverge for increasing L and the available system sizes. It is then still possible that a crossover occurs at a length scale larger than those that can be treated, and χ_{BO} scales to a finite

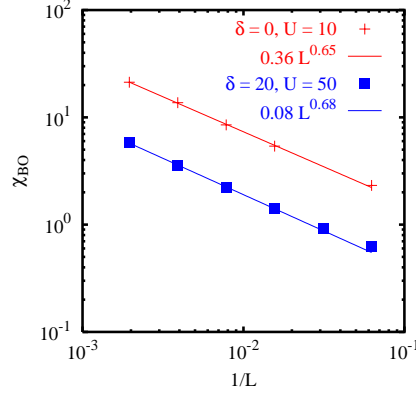


Figure 5.7: The BO susceptibility χ_{BO} as a function of $1/L$ for the ordinary Hubbard model ($\delta = 0$) and $U = 10$ and the ionic Hubbard model for $\delta = 20$ and $U = 50$. DMRG data are indicated by the corresponding symbols and the solid curves represent a least-squares fit to the indicated forms.

value. This tends to underestimate \tilde{U}_{c2} . In the second method, \tilde{U}_{c2} is taken to be the position of the second peak at fixed L , extrapolated to $L \rightarrow \infty$. Since the peak position decreases for increasing L , this method tends to overestimate \tilde{U}_{c2} . From these two procedures, we obtain the bounds $21.55 < \tilde{U}_{c2}(\delta = 20) < 21.69$. For the other values of δ , it is very difficult to accurately determine the lower bound with the data available. We therefore only give the upper bound $\tilde{U}_{c2}(\delta = 1) < 2.95$ and $\tilde{U}_{c2}(\delta = 4) < 5.86$.

A quantum critical point is accompanied by a vanishing characteristic energy scale [59]. At \tilde{U}_{c2} the most obvious candidate is Δ_S , consistent with our numerical data [129] and implying that $\tilde{U}_{c2} = U_{c2}$. This is assumed in the following discussion.

Since the peak in χ_{BO} at U_{c1} is well-defined and has a clear growth with system size, it is reasonable to perform a finite-size scaling analysis. We use a scaling ansatz of the form

$$\chi(U, L) = L^{2-\eta} \tilde{\chi}(L/\xi), \quad (5.13)$$

with $\xi \sim |U - U_c|^{-\nu}$. As can be seen in Fig. 5.8, data for $\delta = 20$ and system sizes of $L = 128$ and greater collapse onto one curve. The best fit is obtained with $U_{c1} = 21.385$ and the critical exponents $\eta_1 = 0.45$ and, relying on the value obtained from the closing of the gap, choosing $\nu_1 = 1$. The latter value is consistent with the value $\nu_1 = 1$ extracted from the divergence of the length scale discussed above.

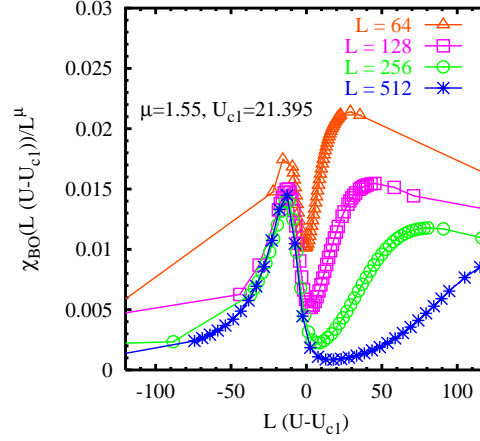


Figure 5.8: A scaling analysis of χ_{BO} for $\delta = 20$.

We have also applied the scaling ansatz for $\delta = 1$ and 4. For decreasing δ , the quality of the collapse of the data for the available systems sizes becomes poorer and the extracted exponents therefore become less reliable. The best fit is again obtained with $\nu_1 = 1$ for both δ , $\eta_1(\delta = 4) \approx 0.55$ and $\eta_1(\delta = 1) \approx 0.65$. For the critical coupling, we obtain $U_{c1}(\delta = 1) \approx 2.7$ and $U_{c1}(\delta = 4) \approx 5.6$, in excellent agreement with the values found by other means. The differences in the η_1 obtained for different U is most likely due to the limited accuracy in extracting the exponent. Since the scaling works better for larger δ we conclude that $\eta_1 \approx 0.5$. Note that this value of η_1 is not in agreement with the value expected in the two-dimensional Ising transition, $\eta = 1/4$ [12].

It is also possible to collapse the finite-size data onto one curve at the second transition point using the scaling ansatz (5.13). We find that the best results are obtained for $\xi \sim \exp(A/(U - U'_{c2})^B)$, indicating that the divergence of the susceptibility at U_{c2} may indeed be exponential as expected for a KT-like transition. However, fitting the limited amount of data available to this form does not produce completely unambiguous results for all fit parameters. Therefore, we have not further attempted to obtain results for A , B , U'_{c2} , and η_2 with this method.

5.4.2 The electric susceptibility and the density-density correlation function

In order to further investigate the physical properties of the different phases and transition points, we calculate the electric polarization and susceptibility [62]. The

polarization is given by

$$\langle P \rangle = \frac{1}{L} \sum_j x_j \langle n_{j\uparrow} + n_{j\downarrow} \rangle, \quad (5.14)$$

where $x_j = j - L/2 - 1/2$ is the position along the chain, measured from the center. The polarization is the response due to a linear electrostatic potential

$$H_{\text{el}} = -E \sum_j x_j (n_{j\uparrow} + n_{j\downarrow}) \quad (5.15)$$

which is added to the Hamiltonian (5.1). The electric susceptibility

$$\chi_{\text{el}} = \left. \frac{\partial \langle P \rangle(E)}{\partial E} \right|_{E=0} \quad (5.16)$$

is the susceptibility associated with this field.

The electric susceptibility has been used to investigate the metal-insulator transition in the t - t' -Hubbard model [62]. In this model, both a phase in which χ_{el} diverges as L^2 (a perfect metal) and a phase in which for increasing system size χ_{el} scales to a finite value (an insulator) were found when varying U for fixed nearest-neighbor hopping t and next-nearest-neighbor hopping t' .

In contrast to the ordinary Hubbard model, the polarization does not always vanish at field $E = 0$ in the IHM. For $U = 0$, $\delta > 0$, one finds $\langle P \rangle = -1/2$. This is due to the alternating ionic potential which induces a charge displacement to the sites with lower potential energy. Due to the OBC's, a chain with even length L starts and ends with a different potential, inducing a dipole moment. This is a boundary effect. In the strong coupling limit, $U \gg \delta$, we find that $\langle P \rangle \rightarrow 0$, as expected. The electric susceptibility χ_{el} can be calculated by discretizing the derivative as $[\langle P \rangle(E) - \langle P \rangle(E = 0)]/E$. The field E must be taken to be small enough so that the system remains in the linear response regime (as discussed for χ_{BO} , close to a critical point, the linear response regime shrinks and very small amplitudes of the external field are required). Note that it is necessary to subtract $\langle P \rangle(E = 0)$ since it is nonzero in general.

A plot of χ_{el} as a function of U for various system sizes is shown in Fig. 5.9(a) for $\delta = 20$. For $U \ll U_{\text{c1}}$ and increasing L , χ_{el} converges to a finite value, similar to the behavior in a non-interacting band insulator and in the correlated insulator phase of the t - t' -Hubbard model [62]. The data clearly develop a maximum at U_{c1} whose height increases markedly with system size, indicating a divergence at the first critical point. The finite-size scaling of this height is consistent with a power-law increase, $L^{2-\eta}$, with $\eta_1 \approx 0.46$. This increase is weaker than the L^2 divergence (which implies $\eta = 0$) found in Ref. [62] and associated with a

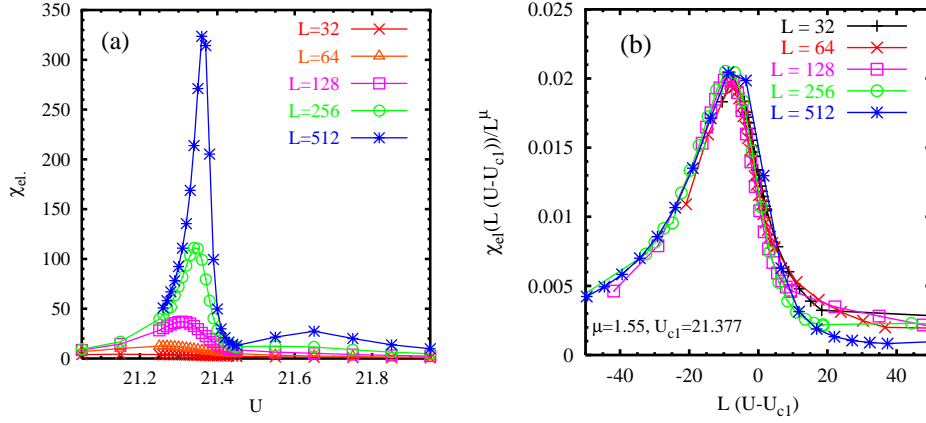


Figure 5.9: (a) The electric susceptibility χ_{el} for $\delta = 20$ plotted as a function of U . (b) A scaling analysis of the data of (a).

perfect metal. For U slightly larger than U_{c1} , the data again seem to saturate with system size. Assuming the scaling form of Eq. (5.13), the data close to U_{c1} can be collapsed on a single curve as demonstrated in Fig. 5.9(b). The best fit is obtained for $\nu_1 = 1$ and $\eta_1 \approx 0.45$. Both of these exponents are in excellent agreement with those found in the scaling analysis for χ_{BO} . We have carried out a finite-size scaling analysis for $\delta = 4$ and $\delta = 1$ and also find diverging peaks at U_{c1} , as well as collapse of the data onto a single curve using the scaling form (5.13) with exponents $\eta_1(\delta = 1) = 0.52$, $\eta_1(\delta = 4) = 0.45$, and $\nu_1 = 1$ (for both δ). The critical U values obtained from this scaling procedure are $U_{c1}(\delta = 1) = 2.68$, $U_{c1}(\delta = 4) = 5.59$, and $U_{c1}(\delta = 20) = 21.38$, which compare well to the values for the critical coupling obtained from the gaps and from the BO parameter and susceptibility.

The data for $\delta = 20$ and $\delta = 4$ for the largest system sizes, $L = 256$ and $L = 512$, suggest that a second peak may develop around U_{c2} . In order to investigate the behavior of $\chi_{el}(L)$ more precisely in this region, we fit a quadratic polynomial to $\langle P \rangle(E)$ through several data points and then take the derivative of this fit function at $E = 0$. This procedure should eliminate errors caused by a small linear response regime. Results obtained from this procedure for $\delta = 20$ indicate a weak divergence at $U = 21.65$, corresponding to a U -value near U_{c2} . In addition, we find an even weaker divergence for *all* $U > 21.65$. The larger the U -value, the smaller the coefficient of the diverging part, so that the divergence is very difficult to observe numerically deep in the strong-coupling-phase. One generally expects the divergence of χ_{el} to be connected to the closing of a gap to excited states which possess at least some ‘‘charge character’’ (in the sense dis-

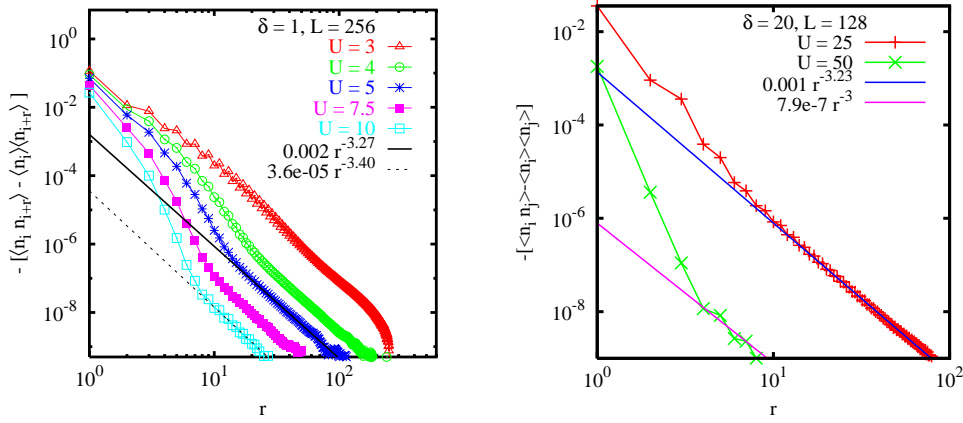


Figure 5.10: The negative of the density-density correlation function $-[\langle n_i n_{i+r} \rangle - \langle n_i \rangle \langle n_{i+r} \rangle]$ for $U > U_{c2}$. The indicated lines are least-squares fits over a range of r in which the behavior is linear on the log-log scale.

cussed below). At U_{c1} the divergence is accompanied by the closing of the exciton gap, leading to a consistent picture.

The strong coupling phase $U \geq U_{c2}$ can further be investigated by examining the behavior of the density-density correlation function

$$C_{\text{den}}(r) = \langle n_i n_{i+r} \rangle - \langle n_i \rangle \langle n_{i+r} \rangle, \quad (5.17)$$

shown in Fig. 5.10 for $\delta = 1$, $\delta = 20$, and different $U > U_{c2}$. Here we have averaged over a number of i -values (typically six) for each r . For each value of U , it is evident that the correlation function behaves linearly on the log-log scale above some value of r , indicating that the dominant long-distance behavior is a power law. (For r close to the system size, finite-size effects from the open boundaries also appear.) Note that the sign of the correlation function is negative for $r > 0$, so that the negative is plotted. A least-squares fit to the linear portion of the curve yields an exponent of approximately 3 – 3.5 for all values of $U > U_{c2}$. This behavior is markedly different from the behavior for $U < U_{c1}$, where we find a clear exponential decay as in a non-interacting band insulator, and from the behavior at U_{c1} , where we find a power law decay with an exponent of ≈ 2 . Note that if the decay were exponential for $U > U_{c2}$, we would expect the correlation length to change quickly with U , leading to a marked variation in the slope. We have ruled out finite-size effects as an origin of the power-law tails as well as possible symmetry breaking due to the OBC's by comparing calculations for $L =$

128 and $L = 256$ with OBC's and $L = 64$ with PBC, which yield identical values except for distances r near the lattice size (or half the lattice size for PBC's).

As demonstrated in Fig. 5.10, similar behavior is obtained for $\delta = 1$ and $\delta = 20$. It therefore seems justified to conclude that this power-law decay is a generic feature of the strong-coupling phase for all δ .

Our findings for χ_{el} and $C_{den}(r)$ are consistent with a scenario in which there is a continuum of gapless excitations for $U > U_{c2}$, where matrix elements of charge operators such as the density $n_j = n_{j\uparrow} + n_{j\downarrow}$, are nonvanishing for some of the states belonging to this continuum. These are the states mentioned above which possess charge character. To further confirm this idea, we have calculated matrix elements $\langle m | n_j | 0 \rangle$, where $|m\rangle$ denotes the m -th excited state and $|0\rangle$ the ground state, for up to $m = 4$, $\delta = 20$, $U > U_{c2}$, and $L = 32$. We find that the third excited state is the first $S = 0$ state, both for the ordinary Hubbard model and the IHM (the fourth state as well as the $m = 1, 2$ states have $S = 1$). For the ordinary Hubbard model, $\langle 3 | n_j | 0 \rangle$ vanishes for all j to within the accuracy of our data and this $S = 0$ state can be classified as a spin excited state since its excitation energy is well below the charge gap. In contrast, $\langle 3 | n_j | 0 \rangle$ is nonvanishing for the IHM and shows a non-trivial dependence on j which has a wavelength of approximately the lattice size, implying that the wave vector characterizing the excitation is near $q = 0$.

As a consequence, this state contributes to the dynamical charge structure factor in the IHM but not in the ordinary Hubbard model. This shows that although several similarities between the strong coupling phase of the IHM and the Hubbard model were found, low-lying excitations in both models are of quite different nature. As we have verified, the energy of $|3\rangle$ becomes smaller for increasing U , in contrast to the behavior of the one-particle gap which increases linearly with U . Due to the numerical effort necessary to target such a large number of states, we were unable to perform these calculations on larger lattices in order to carry out a finite-size scaling analysis of the matrix elements.

In Ref. [162], Aligia finds, using a canonical transformation, that for the IHM the charge operator n_i can be (approximately) expressed in terms of spin operators. Basing on this finding, using a bosonization Ansatz, he concludes that the density-density correlation function decays as

$$C_{den}(r) \approx 48 \frac{U^2 \delta^2 t^4}{(U^2 - \delta^2)^4} r^{-3} \ln^{-3/2} r. \quad (5.18)$$

This expression is in good agreement with the data presented in Fig. 5.10, and supports our surmise that in the strong-coupling regime of the IHM charge and spin degrees of freedom are not completely decoupled, in contrast to the ordinary Hubbard model.

5.5 Summary

In this chapter, we have applied the DMRG introduced in the previous chapter in order to investigate the quantum critical behavior in the ionic Hubbard model at half filling. Our results elucidate the nature of the phase diagram. By carrying out extensive and precise numerical calculations and by carefully choosing the quantities used to probe the behavior, we have been able to investigate the structure of the transition more accurately than in previous work. This has allowed us to resolve a number of outstanding uncertainties and ambiguities. We have worked at three different strengths of the alternating potential δ covering a significant part of the parameter space and find the same qualitative behavior for all three δ -values. In particular, we have carried out extensive finite-size scaling analyses of three different kinds of gaps: the exciton gap, the spin gap, and the one-particle gap. This detailed analysis can be found in Refs. [129, 157]. We find that for fixed δ and in the thermodynamic limit, the exciton gap goes to zero as a function of U at a first critical point U_{c1} , the spin gap goes to zero at a distinct second critical point $U_{c2} > U_{c1}$ and is clearly nonzero at U_{c1} . While U_{c2} for the spin gap is finite to within our resolution, we cannot completely rule out an unresolvably small spin gap for large U , i.e., $U_{c2} \rightarrow \infty$. The one-particle gap (the two-particle gap behaves similarly) reaches a minimum close to U_{c1} , but never goes to zero and never becomes smaller than the spin gap. Due to the explicitly broken one-site translational symmetry, the ionicity is finite for all finite U . For $U \gg \delta$ the ionicity found numerically agrees very well with the one obtained analytically from the strong-coupling mapping of the ionic Hubbard model onto an effective Heisenberg model.

We have also studied the bond-order parameter, the order parameter associated with dimerization, as well as the associated bond-order susceptibility. The result of the delicate finite-size extrapolation indicates that there is a finite bond-order parameter in the intermediate region between U_{c1} and U_{c2} . Here we again cannot strictly rule out $U_{c2} \rightarrow \infty$ on the basis of the bond-order parameter. There is a divergence in the bond-order susceptibility at both U_{c1} and at U_{c2} , as one would expect from two continuous quantum phase transitions. However, the bond-order susceptibility diverges, albeit more weakly than at U_{c1} , in the entire strong-coupling phase, $U \geq U_{c2}$, in agreement with the expectation for a KT-type transition at U_{c2} . We have pointed out that this is in accordance with the behavior found in the strong coupling phase of the ordinary Hubbard model.

We find that the electric susceptibility is finite for $U < U_{c1}$ but diverges roughly as $L^{1.5}$ at U_{c1} . This divergence is weaker than the one found for non-interacting electrons (with $\delta = 0$) and in the metallic phase of the t - t' -Hubbard model [62]. A finite-size scaling analysis of both the bond-order susceptibility and the electric susceptibility yield the same critical exponents at U_{c1} . However,

the value, $\eta_1 \approx 0.5$, is not consistent with the critical exponents of the classical two-dimensional Ising model, listed in Tab. 2.1, in contradiction to the findings of Ref. [12].

The electric susceptibility also shows a divergence, albeit quite weakly, for $U \geq U_{c2}$. Correspondingly, the density-density correlation function has a long-distance decay which is of power-law form, but with a small prefactor which becomes smaller with increasing U , and a relatively large exponent of approximately 3–3.5. We surmise that this behavior is related to mixed spin and charge character of excitations present in the strong coupling phase of the ionic Hubbard model, in contrast to the ordinary Hubbard model. Using a bosonization Ansatz, the power-law decay of the correlation function has been confirmed [162]. The analytical and numerical results agree quite well with each other.

We point out that the divergence of the electric susceptibility at U_{c1} and for $U \geq U_{c2}$ does not necessarily imply a finite Drude weight. Based on our results for various energy gaps and the electric susceptibility, we therefore cannot unambiguously classify all different phases and transition points as being metallic or insulating.

The behavior of all of the quantities we have presented here supports a scenario with two transition points at finite U_{c1} and U_{c2} , with a dimerized phase in the intermediate region. One might nevertheless ask the question whether other scenarios are consistent with our data.

One possibility would be that there is no dimerization for $U > U_{c1}$. However, this is inconsistent with our results for the spin gap, the bond order parameter, and the divergence of the bond-order susceptibility at U_{c1} . Thus, such a scenario is not supported by our calculations.

Another possibility would be that there is a single dimerized phase for $U > U_{c1}$, i.e., that $U_{c2} \rightarrow \infty$. While an unresolvably small gap and dimerization at large U cannot be strictly ruled out by a numerical calculation with finite resolution, we can put quite strong limits on the spin gap and dimerization for a value of U that is only a fraction of t greater than U_{c1} . In addition, we have made arguments involving the strong-coupling limit that support the plausibility of a finite U_{c2} . Together with the divergence of the susceptibilities at two distinct parameter values, we feel that an interpretation of our numerical results in favor of a scenario with an intermediate dimerized phase and a finite value for U_{c2} is compelling.

Chapter 6

Adaptive Time-Dependent Density Matrix Renormalization

As we have discussed in Sec. 3.2, the time evolution of a quantum system is obtained either by directly integrating the time-dependent Schrödinger equation, Eq. (2.2), or by applying a suitable approximation for the time-evolution operator $\hat{U} = \exp(-iHt)$. In the context of the DMRG, both approaches have been utilized. Recent developments are recapitulated in Ref. [163].

The first attempt to calculate the time evolution using the DMRG was to integrate the Schrödinger equation by applying a fourth-order Runge-Kutta scheme [85] using the result of a standard DMRG ground state calculation as the initial state $|\psi_0\rangle$ [164]. However, note that both $|\psi_0\rangle$ and the Hamiltonian \hat{H} determining the time evolution are represented within the restricted basis obtained from the ground-state DMRG calculation. As pointed out in Ref. [165], the main difficulty in calculating the time evolution using the DMRG is that this effective basis determined at the beginning of the time evolution is not able, in general, to represent the state well at later times because it covers only a small subspace of the system's total Hilbert space. In general, this subspace is not suited to represent the system's state at later times $|\psi(t)\rangle$ since the dynamics will lead the state out of this subspace. Even though the discarded weight might seem to be sufficiently small, the error of the time-evolution $\varepsilon = \|\psi(t)\rangle_{\text{DMRG}} - |\psi(t)\rangle_{\text{exact}}\|$ grows continuously. The question of how to control and minimize this error arises. The first suggested improvement was to take into account *all* desired time steps when calculating the restricted basis by adding them to the density matrix [165, 166]. The expectation is that, if at the end of the calculation convergence is achieved, the error for each time step should be of the order of the discarded weight, since the only difference with standard DMRG calculations with more than one target state is that the diagonalization of the Hamiltonian is replaced by the calculation of the time steps. (The error of each target state is expected to be of the order of the discarded

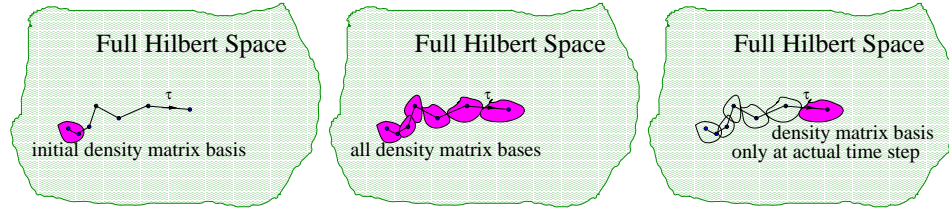


Figure 6.1: Schematic representations of the “static”, “enlarging”, and “adaptive” variants of the t-DMRG.

weight, see Sec. 4.3.2). However, this approach is very expensive with regard to usage of memory and CPU-time, due to the fact that the huge number of target states requires a large number of density matrix eigenstates to be kept in order to have a sufficiently small discarded weight.

A more efficient approach is to try to *adapt* the restricted basis at every time step. Roughly speaking, one determines the restricted basis not by taking all time steps into account, but only the ones relevant for the calculation of the next time-step, e.g., the time steps $|\psi(t)\rangle$ and $|\psi(t + dt)\rangle$. Fig. 6.1 summarizes the three approaches. The way in which the next time-step is obtained is, for now, secondary. However, the two most promising schemes use approximations to the time-evolution operator. In the following, we discuss two candidates for an efficient adaptive time-evolution DMRG method and compare them with each other: In the first approach, the Lanczos time-evolution method discussed in Sec. 3.2 is combined with the DMRG. For the second variant, an approach relying on the second order Trotter-Suzuki [10] decomposition of \hat{U} is used. These approaches have been applied successfully to various systems, and an error analysis shows that the basis adaption works well [167]. However, a detailed comparison of both approaches has not yet been carried out. To do this, we calculate the error in the time evolution by comparing expectation values for observables obtained using the t-DMRG with “exact” results, either from the Lanczos time evolution method, or from exact calculations with hard-core bosons [33]. We use a very small dt for the Lanczos time-evolution method, so that the error can be regarded as negligible at the time scales treated. We also discuss the efficiency and the applicability of both approaches to different systems and situations.

6.1 Time-Evolution Schemes

As discussed above, the basic idea of the basis adaption is to take into account only states relevant for the calculation of the next time step, so that the dimension of the restricted basis becomes as small as possible and the efficiency of the calculation is maximized. The key idea is that the portion of the Hilbert space

covered by the restricted basis is changed so that the representation of the state $|\psi(t + dt)\rangle$ is optimized. One measure for the error is the discarded weight. However, as discussed above, there is a second source of error which is related to the capability of the restricted basis to represent the states $|\psi(t)\rangle$ so that expectation values would have (up to the error that comes from the basis truncation) the same values as when the full Hilbert space is used. Note that, in principle, this error is also relevant for DMRG calculations in equilibrium systems. However, the iterative diagonalization carried out at every step of the DMRG procedure corrects the target state(s), and, therefore, the restricted basis is improved at every step of the iteration procedure, so that the method is variational in the energies. A similar correction step is missing when performing the finite-system sweeps in the calculation of the time evolution. However, as discussed below, for appropriate sets of parameters, the results agree very well, up to errors of the order of 10^{-3} , to exact results. As discussed below, the error is strongly determined by the size of the time step and the number of DMRG steps used to reach a certain time.

In the basis adaption schemes, the subspace of the Hilbert space is modified by adding, e.g., the two time-steps $|\psi(t)\rangle$ and $|\psi(t + dt)\rangle$. In this way the restricted basis is ensured of being capable of representing these states well. This would be exact if the representation of the starting state, $|\psi(t)\rangle$, and of the (approximation to the) time-evolution operator \hat{U} were exact. Both, in general, are not. Thus, at every time-step, four sources of error are present:

1. Error due to the *approximation* of the time-evolution operator.
2. Error in the *representation* of \hat{U} in the present density-matrix basis.
3. Error in the representation of the *target states* (e.g., $|\psi(t)\rangle$, $|\psi(t + dt)\rangle$) due to the cut-off in the density-matrix basis.
4. Non-optimal density-matrix *basis*; if the basis does not cover the “relevant” parts of the Hilbert space, even for a small discarded weight, expectation values can be, in the worst case *qualitatively* wrong.

The last item, in principle, is also relevant for ground-state calculations. There, the calculations can get stuck in local minima and might not converge to the “true” ground state. Usually, by repeating runs with different parameter sets, this error can be controlled. However, for the time evolution, this is more difficult.

Every basis adaption scheme must minimize these errors. In general, this is done by “appropriately” choosing the time step dt , the sweeping procedure, and the target states, as will be discussed in detail in the next sections. One important parameter to control the calculation is the number of states m kept in the restricted basis. The simplest approach is to keep m sufficiently high and keep it fixed during

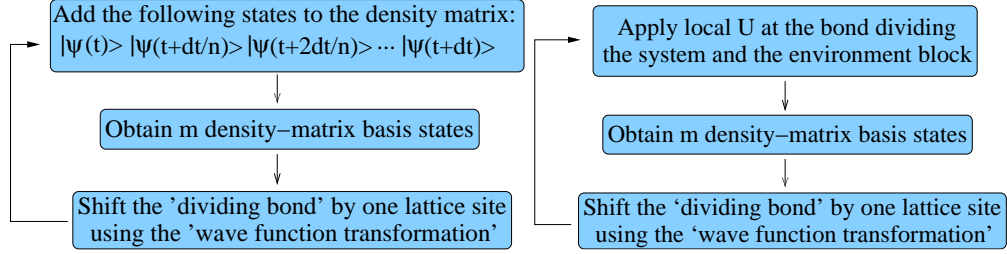


Figure 6.2: Flowcharts for the Lanczos (left scheme) and the Trotter (right scheme) adaptive t-DMRG algorithms.

the whole time evolution. The second possibility is to keep the discarded weight fixed and to change m during the time evolution. We find this approach to be preferable. Especially at the beginning of the time evolution, we find that only a small m is needed to reach a small error in the observables, so that calculations by adapting m become faster. Note that, in principle, there is also the possibility of changing the time step dt during the time evolution. We refrain from doing so and leave this issue open for future investigations.

The basis adaption schemes for the Lanczos and for the Trotter adaptive t-DMRG are sketched in Fig. 6.2 and are discussed in more detail below. Note that errors under points 3 and 4 are immanent to every known basis adaption scheme - the difference in the behavior, and in the details of the sweeping are thus solely determined by the approximation to the time-evolution operator used.

6.1.1 Lanczos t-DMRG

To formulate the basis adaption scheme applied to the Lanczos t-DMRG, we follow a suggestion of Feiguin and White in Ref. [168]. In their approach, an adaption scheme for a Runge-Kutta integration of the Schrödinger equation is developed. The idea is to use the time steps $|\psi(t)\rangle, |\psi(t + dt)\rangle$ as well as additional, intermediate time steps within the interval $[t, t + dt]$ as target states. This is expected to be a better approximation to the density matrix during one time step,

$$\rho(t, t + dt) = \int_t^{t+dt} d\tau |\psi(\tau)\rangle\langle\psi(\tau)|. \quad (6.1)$$

On the same grounds, we expect that this scheme should enable one to perform a suitable basis adaption for the Lanczos t-DMRG. However, it remains unclear how many intermediate time-steps are needed, what the optimal value for dt is, and how many sweeps should be performed. In addition, it might well be that using additional target states, e.g., the Lanczos vectors, could improve the quality

of the time evolution.

First, we analyze the number of sweeps needed. As depicted in Fig. 6.2, the wave-function transformation is needed in order to perform the basis updates. Each of these transformations is a projection to the restricted basis belonging to the current superblock configuration. The error of each projection is the discarded weight ε_l at the current configuration. Thus, performing a series of wave function transformations from $l = 1$ to $l = L$ leads to an error which increases with every step. It is therefore evident that the error during the time evolution is minimized if the number of wave-function transformations is minimized. In order to update the representations of the local observables, it is necessary to sweep at least *once* through the lattice. We find that the quality of the results is not improved compared to using only one half-sweep when using two or more half-sweeps, but, in agreement with this discussion, can become worse. Thus, in the Lanczos t-DMRG, *only one* half sweep should be used to update the basis of the system.

It is preferable to have as small a number of target states as possible, since, on general grounds, one expects that a smaller number of basis states should lead to the same discarded weight. Thus, utilizing a pure-state density matrix containing only $|\psi(t + dt)\rangle$ would be preferable. Note, however, that such a basis might lose its capability to represent the previous time step $|\psi(t)\rangle$ well, leading to a possibly large error during the time evolution. On the other hand, if the time step is small enough, the two time steps should be sufficiently similar, so that the effective basis should be capable of representing both states well. In Secs. 6.2.1 and 6.2.2 we discuss the effect of changing the number of intermediate states on the error.

6.1.2 Trotter t-DMRG

The idea of using a Trotter-Suzuki decomposition [10] of the time-evolution operator for carrying out the time evolution in DMRG-like algorithms was first discussed by G. Vidal [169], who called the algorithm 'time-evolving block decimation' (TEBD) procedure. There is a large overlap between this algorithm and the DMRG; Daley *et al.* [107] used it as a basis to incorporate the adaptive Trotter t-DMRG into an existing DMRG code. Independently, White and Feiguin [170] implemented the method into their code. The approach is discussed in detail in Ref. [171]. The idea is to split up the time-evolution operator into *local* time-evolution operators U_l acting only on the *bond* l . For lattice Hamiltonians containing only terms connecting nearest-neighbor sites, this is easily performed using the Trotter-Suzuki decomposition, which in second order is given by

$$e^{-i\Delta\tau H} \approx e^{-i\Delta\tau H_{\text{even}}/2} e^{-i\Delta\tau H_{\text{odd}}} e^{-i\Delta\tau H_{\text{even}}/2}. \quad (6.2)$$

Here H_{even} and H_{odd} are the parts of the Hamiltonian containing terms on even and odd bonds, respectively. Since each bond term H_l with H_{even} or H_{odd} commutes with the other terms, $e^{-i\Delta\tau H}$ can then be factorized into terms acting on individual bonds. As depicted in Fig. 4.4, in the DMRG procedure two sites are usually treated exactly, i.e., the entire Hilbert space of the two sites is included. The Trotter variant of the t-DMRG exploits this feature by applying $U_l = e^{-i\Delta\tau H_l}$ at the bond given by the two “exact” sites. In this way, in contrast to the Lanczos approach discussed above, the time-evolution operator has no further approximations other than the error introduced by the Trotter decomposition. In particular, the error introduced by the cutoff is avoided. The wave function of the lattice is then updated by performing two half-sweeps over the lattice and applying U_l at the “dividing bond”. In this way, only one wave function must be retained and it is possible to work with the density matrix for a pure state. The flowchart is sketched in Fig. 6.2. However, the method is restricted to systems with local or nearest-neighbor terms in the Hamiltonian.

6.1.3 Comparing the Adaptive Lanczos and Trotter t-DMRG Variants

While the sweeping procedure in the Lanczos and the Trotter approach is very similar, the number of sweeps in the Trotter approach is determined by the order of the Trotter decomposition. For a Trotter decomposition to second order, two half-sweeps are needed, instead of one in the Lanczos case; for higher order decompositions, more sweeps are needed [171], so that, in general, one might expect that this approach might be slower than the Lanczos approach. Note, however, that the dimension of the site basis normally is quite small so that the application of a local time-evolution operator is much faster than the calculation of all the necessary Lanczos vectors. Usually, the gain in time in the Lanczos approach by avoiding one half-sweep is therefore smaller than the time spent for the additional half-sweep in the Trotter approach. However, the Trotter error is, in general, larger than the error in the Lanczos approximation of the time-evolution operator, which was discussed in Sec. 3.2. Thus, there is an interplay of possible errors - it is not a priori clear which method is more exact and which requires smaller resources. The errors of both approaches are discussed in the next section. As a rule of thumb, the more target states, the larger the dimension m of the density-matrix basis must be. Due to the fact that the Trotter approach relies on a single target state, it is to be expected that it needs a smaller m than the Lanczos approach which, as discussed in Sec. 6.1.1, is based on a variable number of intermediate time-steps in the time-interval $[t, t + dt]$. Therefore, it is expected to be slower than the Trotter approach. As we will see now, although the Lanczos approach is more difficult to control

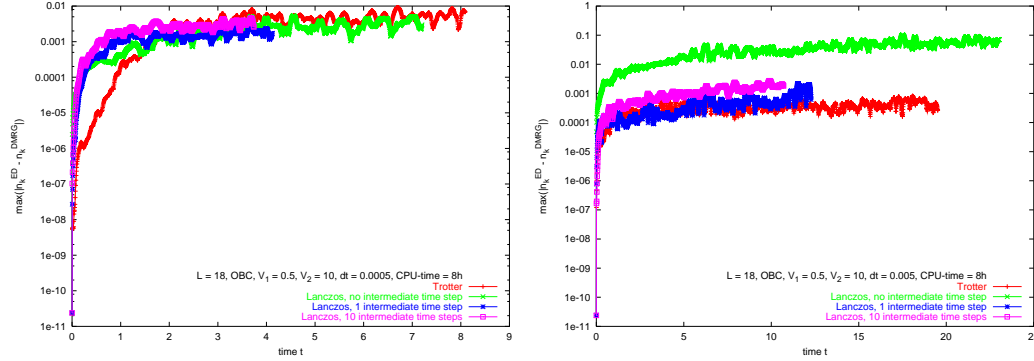


Figure 6.3: Maximum value of the deviation between results for the momentum distribution $\langle n_k \rangle$ obtained with the Lanczos time-evolution method and with the Lanczos and Trotter adaptive t-DMRG for a system of spinless fermions at half filling with $L = 18$ pushed out of equilibrium by changing the interaction strength from $V_0 = 0.5$ to $V = 10$. The left plot shows results for $dt = 5 \cdot 10^{-4}$, the right for $dt = 5 \cdot 10^{-3}$. The results compare calculations that took 8 CPU hours.

than the Trotter variant, both are very accurate and errors $< 1\%$ after several hundred time steps can be attained. Thus, in combination, both approaches give a toolset to treat a large class of strongly correlated out-of-equilibrium systems in quasi one-dimensional geometries.

6.2 Error analysis

Fig. 6.3 displays an error analysis for a quench scenario for a system with $L = 18$ sites. As can be seen, an appropriate choice of the parameters leads to errors in the observables that is $\ll 1\%$ at the end of the time evolution. However, a bad choice of parameters can lead to results with errors as big as errors $\approx 10\%$. Therefore, care has to be taken when choosing the control parameters for the calculation. In the following, we investigate the error for two out-of-equilibrium situations treated in this thesis in detail. First, we analyze the errors for the quench scenario discussed in chapter 8 for various choices of parameters by comparing observables to results from the Lanczos time-evolution method for $L = 24$ at half filling. Next, we analyze the error for a system of hard-core bosons by comparing to exact results obtained via the Jordan-Wigner transformation [33, 13, 34] for a system with $L = 60$ and 20 particles.

The possible control parameters for the Trotter variant are the time step dt and the maximum number m_{\max} of density-matrix basis states kept during the time evolution. As discussed above, we aim to reach a particular target discarded weight

Parameters	Error
$dt = 0.005, m_{\max} = 1000, \epsilon = 10^{-9}$	$4.7 \cdot 10^{-3}$
$dt = 0.005, m_{\max} = 300, \epsilon = 10^{-9}$	$7.1 \cdot 10^{-3}$
$dt = 0.005, m_{\max} = 1000, \epsilon = 10^{-6}$	$2.0 \cdot 10^{-2}$
$dt = 0.001, m_{\max} = 1000, \epsilon = 10^{-9}$	$2.7 \cdot 10^{-2}$
$dt = 0.01, m_{\max} = 1000, \epsilon = 10^{-9}$	$1.9 \cdot 10^{-3}$
Lanczos, 5 interm. states $dt = 0.1, m_{\max} = 1000, \epsilon = 10^{-9}$	$6.1 \cdot 10^{-4}$

Table 6.1: Error in $\langle n_k \rangle$ at the end of the time evolution ($t = 15$) obtained with the various sets of control parameters when using the Trotter t-DMRG, compared to the Lanczos t-DMRG when using large time-steps.

during the time evolution – hence, the third control parameter for the Trotter t-DMRG is ϵ .

For the Lanczos variant, two more control parameters play a role: The calculations can be controlled by changing the number of intermediate time steps, and, in principle, by changing the number of half-sweeps. As discussed before, we choose to perform only one half-sweep. We compare in the following the results when keeping only $|\psi(t + dt)\rangle$ as a target state, and, hence, working with a pure state density-matrix as in the Trotter variant, with the case when including $|\psi(t)\rangle$ and $|\psi(t + dt)\rangle$ as target states. In addition, when choosing relatively large time steps, the accuracy is tested when including five intermediate states in total from the current time-interval. Note that the tolerance in the stopping criterion of the Lanczos procedure, Eq. 3.21, is another control parameter. Based on the discussion in Sec. 3.2, we choose the same parameters, i.e., $\text{tol} = 10^{-13}$ and a minimum number of Lanczos vectors $m_{L,\min} = 10$. In this way, the error contributed by the Lanczos approximation of the time-evolution operator is minimized.

In principle, one can consider adding additional target states in both variants, e.g., $\hat{H}|\psi\rangle$ during the time evolution. Since the situation is already pretty difficult (for the Lanczos case we already have a *five-dimensional* parameter space), we do not do so and investigate only the simplest situations.

6.2.1 Accuracy of the Method for a Quench Scenario

As discussed in Sec. 2.5, an important class of out-of-equilibrium situations is the sudden change of an intrinsic parameter, i.e., a quench. Usually the initial state is homogeneous, i.e., the particle number is non-zero everywhere on the lattice, so that problems arising from regions with small or zero particle number

as encountered, e.g., for particles in a trap, are avoided. Quenches should thus be scenarios where the t-DMRG is expected to work reliably without any further complications (aside from the correct choice of control parameters).

In Fig. 6.4, the relative error in the energy is displayed for a quench for a one-dimensional, half-filled system of spinless fermions. Note that the energy should be constant in time. Therefore, no comparison to exact results obtained by other methods is needed, so that it can always be monitored in a t-DMRG run as long as the Hamiltonian is time-independent. Hence, this quantity is the main source of information about the accuracy of a certain simulation, and, therefore, it is helpful to compare it with the errors in other observables obtained by comparing them to exact results, where available.

The initial state is the ground state at $V = 0.5$. The time evolution is performed with $V = 2$, i.e., the interaction is changed by a small amount, and $V = 40$, i.e., a change of the order of 10 times the bandwidth. As can be seen in Fig. 6.4, the relative error in the energy at the end of the time evolution can be $< 10^{-4}$. However, the accuracy varies significantly depending on the choice of the control parameters.

In Fig. 6.5, the relative error in the momentum distribution function,

$$\langle n_k \rangle = \frac{1}{L} \sum_{l,m} e^{-i(l-m)k} \langle c_m^\dagger c_l \rangle, \quad (6.3)$$

is shown for the same choice of control parameters as in Fig. 6.4. The plots show the maximum deviation found in $\langle n_k \rangle$ at the various instances of time and thus the upper bound for the error in this quantity. In most cases, its magnitude is, unfortunately, much higher than the error found in the energy. It is therefore not possible to quantify the error in other observables using the error in the energy. However, an appropriate choice of parameters leads to an error in $\langle n_k \rangle$ which is less than 1% at the end of the time evolution. This is reflected in a very small error in the energy. Calculations with large system sizes therefore need to aim for a possibly small relative error in the energy, if possible of the order of 10^{-3} or smaller, in order to obtain errors in other observables of a few percent or less.

The momentum distribution function is obtained as the Fourier transform of the one-particle density matrix; thus, an average over the lattice is performed. In order to analyze errors in quantities where no average is performed, the density-density correlation function

$$C_d(r) = \langle n_i n_{i+r} \rangle - \langle n_i \rangle \langle n_{i+r} \rangle \quad (6.4)$$

is analyzed in Fig. 6.6 for the same sets of parameters as in Figs. 6.4 and 6.5. This quantity goes to zero for $|i - j| \rightarrow \infty$ and, in addition, oscillates between positive

and negative values. Hence, the relative error is not meaningful due to the possible division by numbers very close to zero. Therefore, in Fig. 6.6 the absolute value of the maximum difference with the exact results is plotted. Depending on the choice of parameters, the error ranges from values $\sim 10^{-4}$ up to ~ 0.1 .

For the calculations presented in chapter 8, the standard choice for the parameters is a time step $dt = 0.005$, a target discarded weight of $\epsilon = 10^{-9}$ and a maximal number of basis states $m_{\max} = 1000$, i.e., the case analyzed in the top row in Figs. 6.4 – 6.6. We find this set of parameters to be “best” by comparing the errors in $\langle n_k \rangle$ at time $t = 15$ and the needed CPU time. For this choice of parameters, the relative error in the energy is, for both variants of the t-DMRG, $\leq 10^{-4}$, the relative error in $\langle n_k \rangle$ is < 0.01 , and the absolute error in the density-density correlation function is $< 3 \cdot 10^{-4}$.

In Appendix A, we present more details about these calculations. For the cases considered, the time evolution of the number of density-matrix eigenstates m as well as the discarded weight ϵ are shown. As one can see for most of the chosen sets of control parameters, one needs a larger m for the Lanczos approach, making it slower. However, in order to better analyze the two quenches with $V = 2$ or $V = 40$, respectively, time steps small enough for resolving the oscillations for the latter case have been chosen. For larger time steps, using intermediate time steps should lead to a smaller error in the Lanczos t-DMRG when compared to the Trotter approach. In order to investigate this situation, we focus now on $V = 2$, choose $dt = 0.1$, and use 5 intermediate time steps as target states. In Fig. 6.7 we compare the error of the Lanczos t-DMRG with five intermediate time steps against the Trotter t-DMRG when using $dt = 0.005$, $m_{\max} = 1000$, $\epsilon = 10^{-9}$, i.e., our standard set of parameters. As can be seen, although the error in the energy is larger, the errors of the observables in the Lanczos approach for this large value of dt are smaller than the errors of the Trotter approach. However, when comparing the CPU times, we find that it is, in spite of the larger time step, much slower than the Trotter variant. It is not helpful to use a much larger time step since otherwise the resolution in the time evolution becomes too small for a meaningful investigation of the observables of interest. Hence, when applicable, we choose the faster Trotter variant of the t-DMRG with small values of dt to treat quenches. In Tab. 6.1, the errors in $\langle n_k \rangle$ at the end of the time evolution ($t = 15$) for a quench with $V = 2$ are compared for the various sets of control parameters for the Trotter variant and for the Lanczos variant with $dt = 0.1$.

6.2.2 Accuracy of the Method for Wavepacket Dynamics

Another important class of non-equilibrium situations is when the initial state is prepared by applying external fields. An example is a system of trapped particles which is investigated after the trap is released. Such a situation is discussed

in chapter 7. The situation with trapped particles is a rather difficult case for the DMRG because the density on extended regions of the system is zero – this leads to a vanishing entanglement with the rest of the system, i.e., an appropriate density-matrix basis is difficult to obtain when calculating the ground state of such systems. In order to overcome this difficulty, we modify the warmup sweep and adjust the quantum numbers according to the desired local filling. Our calculations show that the initial state found in this way has very small errors (the energy for a trapped system of hard-core bosons is correct up to deviations of the order of 10^{-6}). In Fig. 6.8, the maximum of the absolute error of the local density $\langle n_i \rangle$ and the maximum of the relative error in $\langle n_k \rangle$ are displayed for a system of $L = 60$ lattice sites and with $N = 20$ initially trapped hard-core bosons. The comparison is done with exact results obtained via a Jordan-Wigner transformation. (At this point, we acknowledge Marcos Rigol for giving us his data for the hard-core bosons). As can be seen, even for this more difficult system, the errors at the end of the time evolution are $< 1\%$ for an appropriate choice of control parameters.

In Appendix A, we present the time dependence of the number of density-matrix states m and discarded weight ϵ for this case. As can be seen in Fig. 6.8, the Lanczos method with only one target state is found to have, by far, the smallest error for this kind of problem. Hence, we conclude that for this class of problems, the Lanczos variant of the t-DMRG works better. This is supported by similar calculations with initially trapped soft-core bosons [172].

6.3 Discussion

In this chapter, we have presented extensions to the DMRG that can treat time-dependent problems. In particular, the Lanczos and the Trotter variants of the adaptive t-DMRG have been presented. An error analysis for a quench and for particles released from a trap have been presented. For quenches, we find that the Trotter variant has the smaller errors or is much faster than the Lanczos variant. For the particles released from a trap, the Lanczos method with a single target state works significantly better. We find that, with an appropriate choice of parameters, the errors of the methods can be controlled to within 1% at the end of the time evolution. Therefore, both approaches represent powerful tools to treat a variety of strongly correlated quantum systems in general out-of-equilibrium situations.

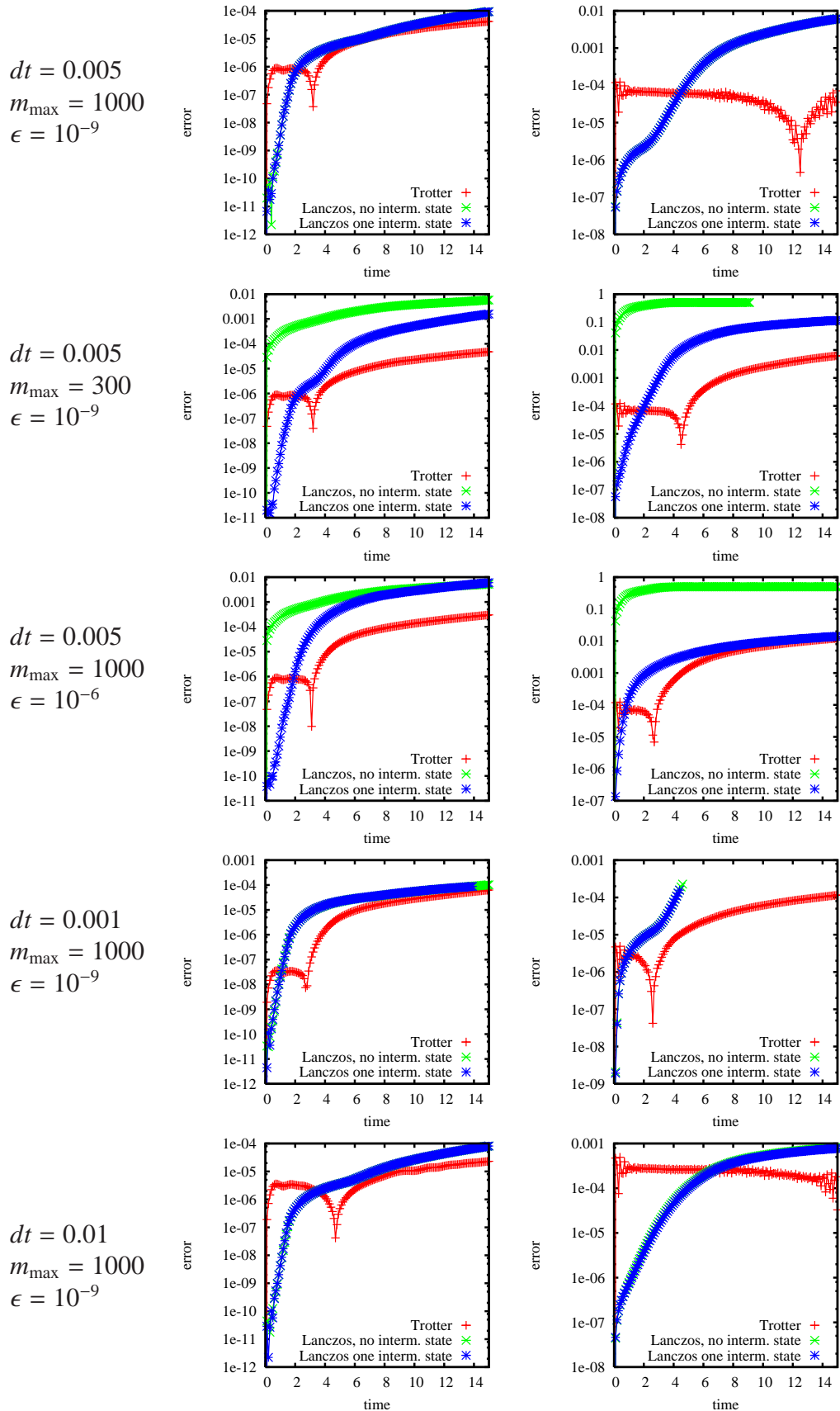
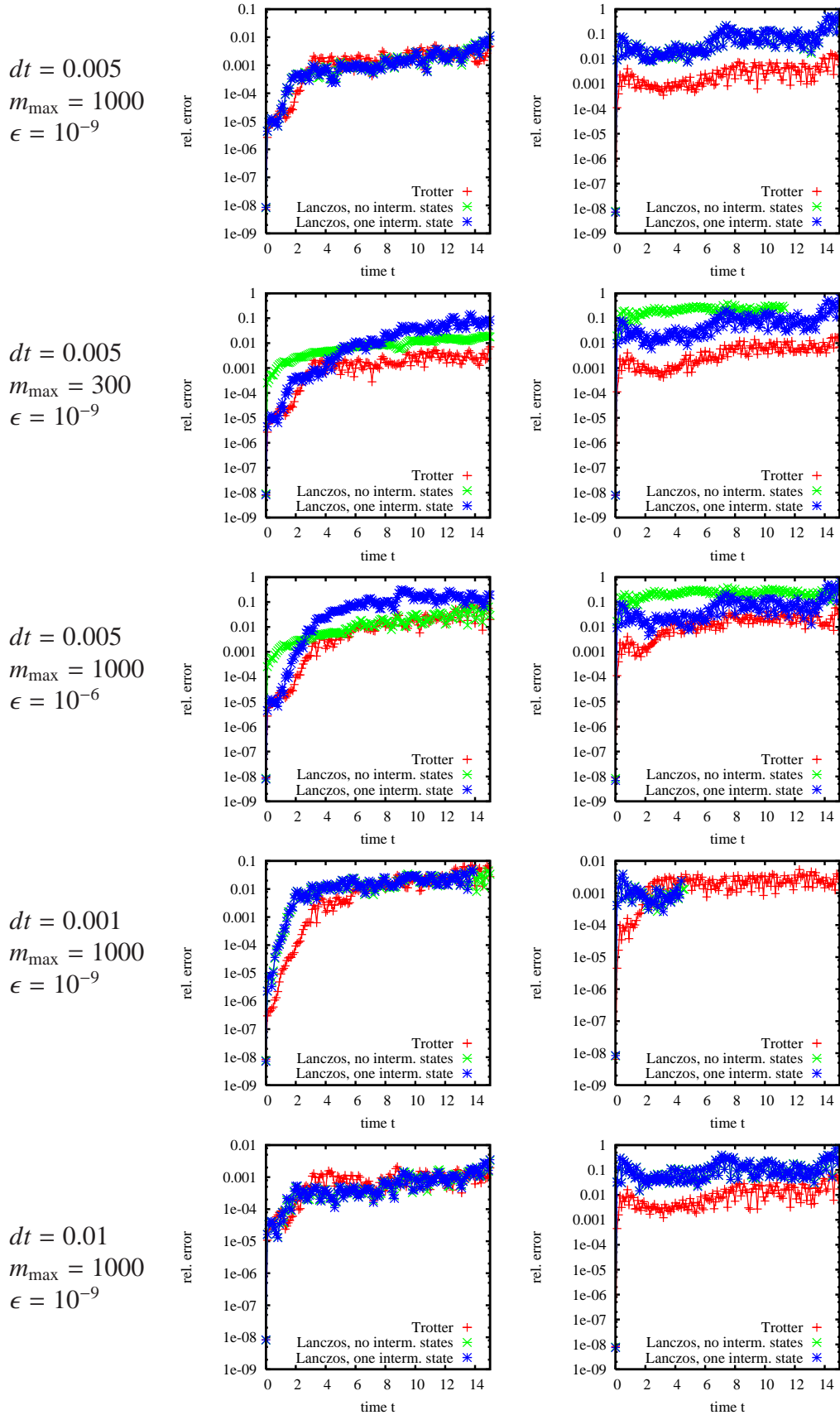


Figure 6.4: Relative error in the energy for a quench in a system with $L = 24$ sites for the choices of control parameters indicated. The plots in the left column show results with $V = 2$, in the right column with $V = 40$. In all cases, the initial state is obtained with $V_0 = 0.5$.

Figure 6.5: Relative error in $\langle n_k \rangle$ for the same situation as in Fig. 6.4.

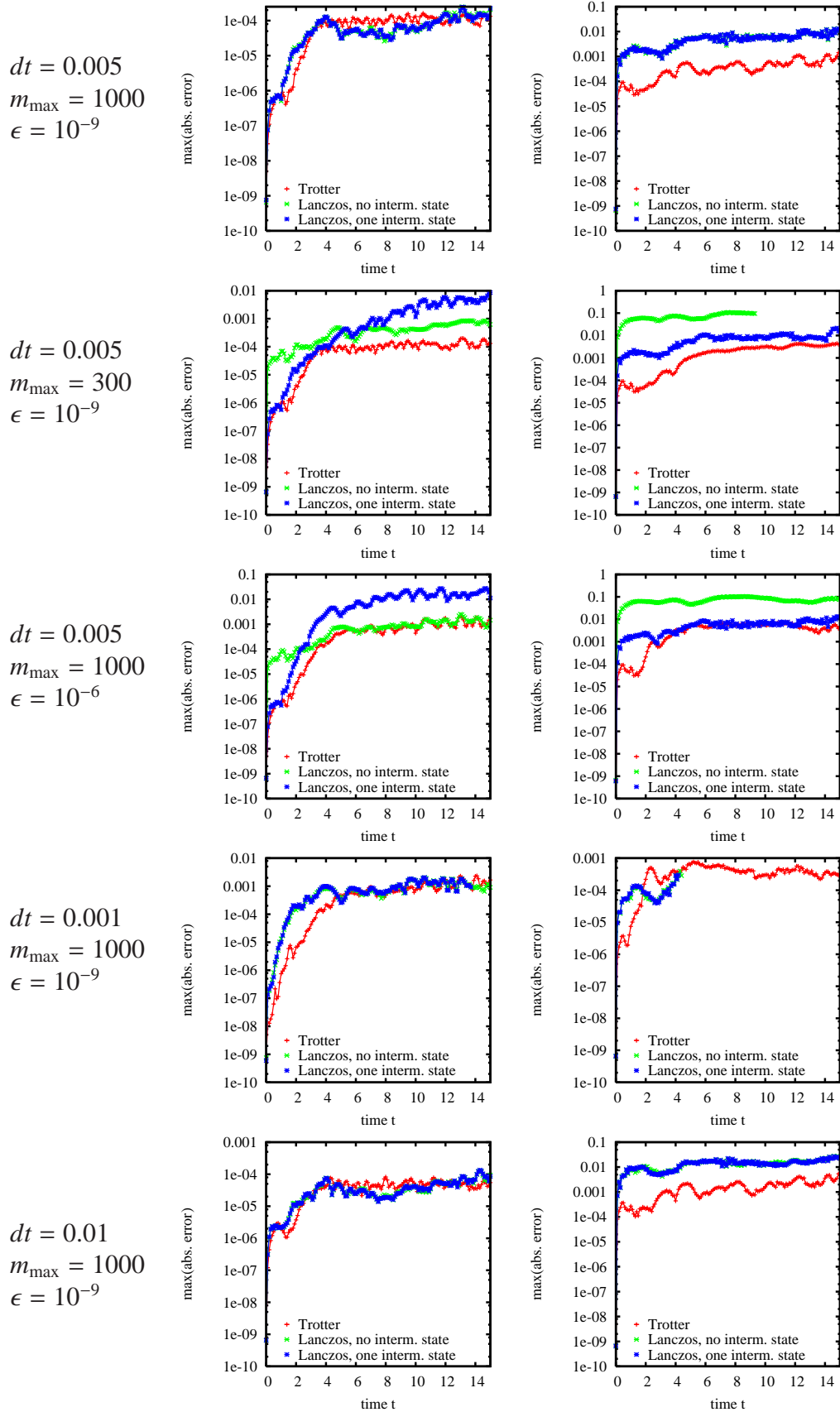


Figure 6.6: Absolute error of the cumulant of the density-density correlation function for the same situation as in Fig. 6.4.

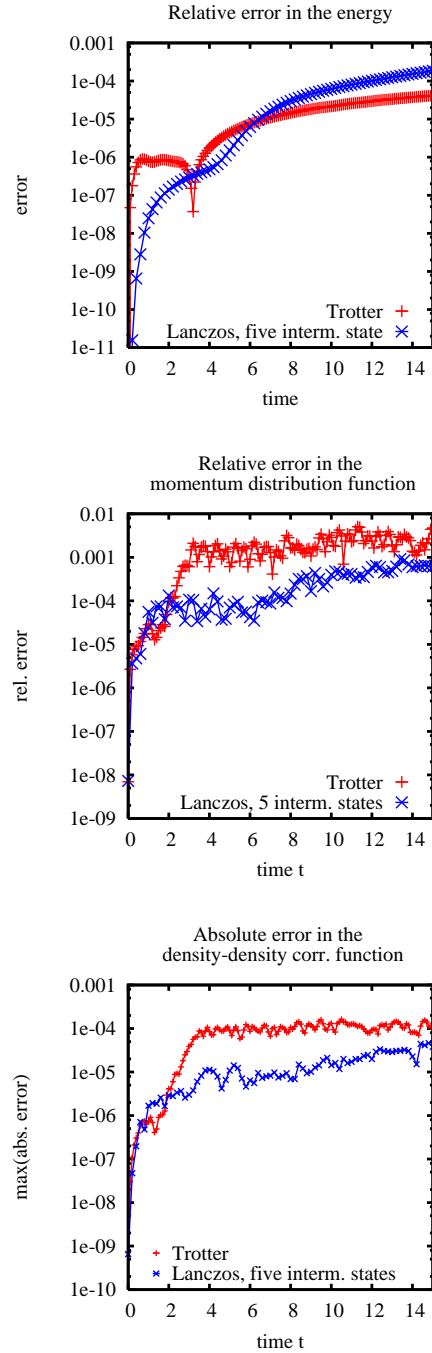


Figure 6.7: Comparison of the errors obtained for the Trotter variant and our standard set of parameters (i.e., $dt = 0.005$, $m_{\max} = 1000$, $\epsilon = 10^{-9}$) with the errors of the Lanczos approach with a larger time step $dt = 0.1$ and 5 intermediate time steps as target states. The plots display the relative error in the energy (top), the relative error in $\langle n_k \rangle$ (middle) and the absolute error in the cumulant of the density-density correlation function (bottom).

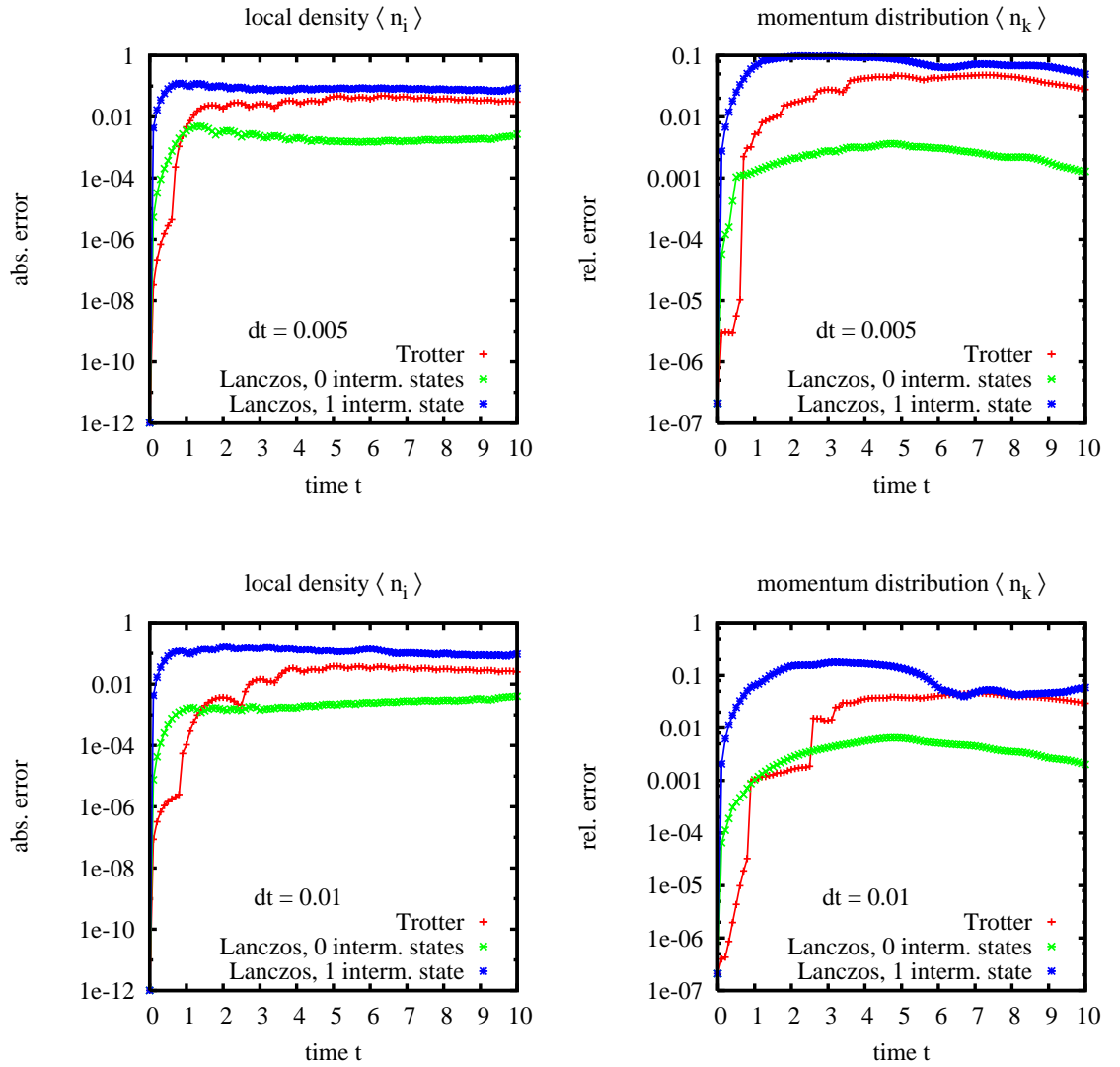


Figure 6.8: Error analysis for a system with $L = 60$ and $N = 20$ hard-core bosons released from a trap. The comparison is done with exact results obtained via a Jordan-Wigner transformation [33]. The left column shows the maximum of the absolute error in the local density. The right column shows the maximum of the relative error in the momentum distribution function. The cases for $dt = 0.005$ (upper row) and $dt = 0.01$ (lower row) are shown.

Part II

Time Evolution of Strongly Correlated Quantum Systems

Chapter 7

Coherent Matter Waves of Interacting Bosons on a Lattice

In this chapter, we study how coherent matter waves emerge after releasing initially trapped bosons on a one-dimensional lattice. This is relevant for the possible realization of an atom laser in experimental setups using optical lattices. We treat the general out-of-equilibrium evolution of a one-dimensional Bose gas with finite on-site Coulomb repulsion U , whose initial state is prepared as a Mott insulator. It was previously shown that, in the hard-core limit, $U \rightarrow \infty$, an initial Fock state develops quasi-long-range correlations when the bosons are allowed to evolve freely on a one-dimensional lattice [13, 34]. In particular, the momentum distribution function $n_k \equiv \langle n_k \rangle$ develops sharp peaks at momenta $k = \pm\pi/2a$, where a is the lattice constant. An examination of the one-particle density matrix shows that, after the formation of the peaks in n_k , it decays as $1/\sqrt{x}$ at long distances, as it does for hard-core bosons in equilibrium [173, 174], demonstrating that, in fact, the peaks in n_k signal the emergence of quasi-coherence at a finite wavevector. A detailed picture of the (quasi-)coherent part is obtained by examining the lowest natural orbital (NO), i.e., the eigenvector of the one-particle density matrix corresponding to the largest eigenvalue. Once the peaks in $\langle n_k \rangle$ form, the NO evolve at a constant velocity $v_{NO} = \pm 2at/\hbar$, where t is the nearest-neighbor hopping amplitude, without appreciable change in their form. These are the maximal group velocities on a lattice with a tight-binding dispersion $\epsilon_k = -2t \cos ka$. The process of formation of the quasi-condensate is also characterized by a power law. The population of the quasi-condensate increases in a universal way as $\sim 1.38 \sqrt{t\tau/\hbar}$, as a function of the evolution time τ , independently of the initial number of particles in the Fock state. The time τ_m at which the maximal occupation of the NO is reached depends linearly on the number of particles N_b in the initial Fock state, and is given by $\tau_m = 0.32N_b\hbar/t$.

The appearance of quasi-condensates at $k = \pm\pi/2a$ can be understood on the

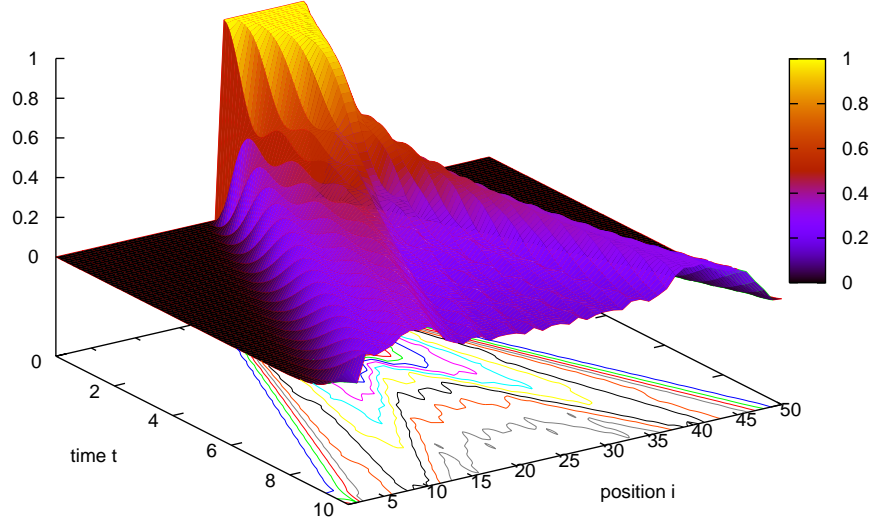


Figure 7.1: Time evolution of the local density $\langle n_i \rangle$ of an initially uncorrelated Fock state of 10 hard-core bosons on a lattice with $L = 50$ sites obtained using the t-DMRG.

basis of total energy conservation, as discussed in Ref. [33]. Given the dispersion relation of hard-core bosons on a lattice, since the initial Fock state has a flat momentum distribution function, its total energy is $E_T = 0$. If all the particles were to condense into one state, it would be to the one with an energy $\bar{\epsilon}_k = E_T/N$. Taking into account the dispersion relation $\epsilon_k = -2t \cos ka$, $\bar{\epsilon}_k = 0$ corresponds to $k = \pm\pi/2a$. Actually, since there is only quasi-condensation in the one-dimensional case, the argument above applies only in that the occupation of a given state is maximized. In addition, the minimum in the density of states at these quasi-momenta strengthens the quasi-condensation into a single momentum state.

Since hard-core bosons can be treated exactly [14, 13, 175, 34, 30], they are extremely well-suited for a theoretical study of nonequilibrium dynamics because large systems (with hundreds to thousands of bosons) can be examined over long times. However, the experimental investigation is hampered by the quite stringent requirements for the realization of such systems. We therefore consider here the case of finite interactions, modeled by the one-dimensional Hubbard model

$$H = -t \sum_i (b_i^\dagger b_{i+1} + h.c.) + \frac{U}{2} \sum_i n_i (n_i - 1) , \quad (7.1)$$

where b_i^\dagger and b_i are bosonic creation and annihilation operators, respectively, and $n_i = b_i^\dagger b_i$ is the density operator. The hard-core limit corresponds to $U \rightarrow \infty$. The

value at which the Mott insulator appears has been estimated as $U_c/t \sim 3.5$ in one dimension for a commensurate density $n = 1$ [32]. We treat systems with values of the interaction $U \geq 6$, hence, for all the cases considered here, the systems are clearly Mott insulators.

In this chapter, we apply the t-DMRG to study the free expansion of soft-core bosons out of an initial Mott insulator state in which the bosons are spread over several lattice sites and compare it to the hard-core case. The error analysis for the t-DMRG has been discussed in Sec. 6.2.2. Fig. 7 shows the expansion of hard-core bosons obtained with the t-DMRG. At least for large values of U , the results are expected to be very similar to those for hard-core bosons. However, it is quite unclear if the scenario obtained with hard-core bosons prevails when going to small values of the interaction. As shown next, the essential features are preserved even for small values of the interaction U . In addition, tuning the strength of the interaction allows for new control possibilities.

We consider here the free expansion of N_b interacting bosons described by the Hamiltonian (7.1) on a one-dimensional lattice with L sites, lattice constant a , and open boundary conditions. In the cases considered here, we take $N_b = 20$ and $L = 60$. Due to memory limitations, it is not possible to allow for all possible occupations of a given site. In general, the maximum number of bosons per site needed to have an accurate description of the system increases as U decreases. In all cases treated here, a maximum of three bosons per site was sufficient. Even at the smallest interaction studied here ($U/t = 6$), no appreciable difference was observed when the cutoff was changed from 3 to 4 bosons per site. Since the system becomes more dilute in the course of the free expansion, the limitation in the number of bosons per site becomes even less important at later times. The time sequences shown are all limited to times shorter than the time it takes the matter wave to reach the boundary of the system.

7.1 Local Density and Momentum Distribution Function

In this section, we compare the time evolution of the local density, $\langle n_i \rangle(t)$, and of the momentum distribution function for a system with a high value of the interaction, $U/t = 40$.

Figure 7.2 shows a comparison of the density (Fig. 7.2(a)) and the momentum distribution function (Fig. 7.2(b)) at four different times. At such high values of the interaction, it is expected that the particles behave as hard-core bosons. In fact, there is no noticeable difference in the density profiles at any time. However, the momentum distribution functions at $\tau = 0$ show clear differences. While hard-

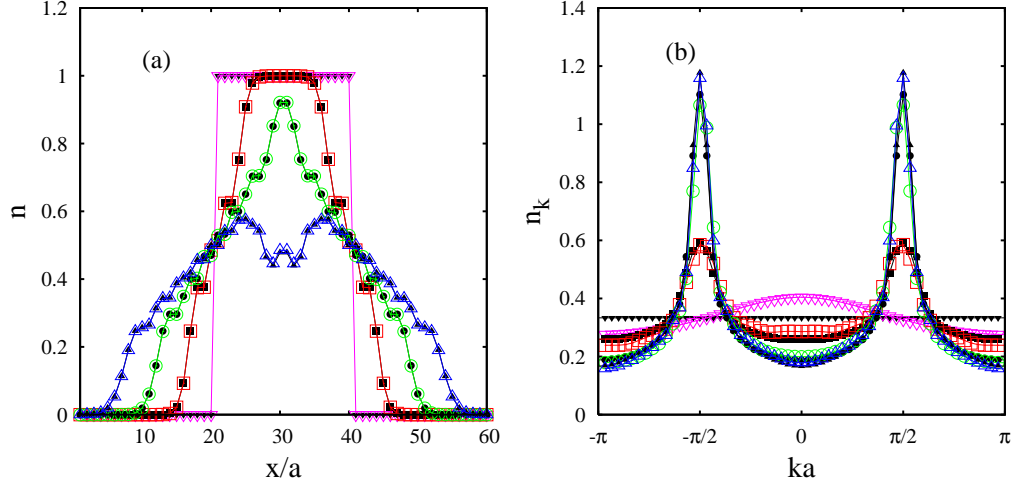


Figure 7.2: Comparison between hard-core bosons (filled black symbols) and soft-core bosons (unfilled colored symbols) with $U/t = 40$ for (a) density and (b) n_k at time $\tau = 0$ (∇), $\tau = 2.52$ (\square), $\tau = 4.98$ (\circ), and $\tau = 7.5$ (\triangle) in units of $1/t$.

core bosons are equally distributed over all momenta, the soft-core case has a maximum at $k = 0$, showing that even in a Mott insulator, the fluctuations of the number of particles at each side populate that state preferentially. Nevertheless, after the Mott insulator is allowed to expand, the difference between both systems becomes barely noticeable. Already at the second time shown in Fig. 7.2, where a Mott plateau still exists at the center of the cloud (Fig. 7.2(a)), the momentum distribution functions of the hard- and soft-core bosons are very close to each other. This is expected because the constraint of a hard core should become less relevant when the system is diluted.

Now we discuss the behavior of the expansion for smaller values of the interaction U . Although at $U/t = 40$ the momentum distribution function closely follows the shape of n_k of hard-core bosons, a tiny asymmetry can be seen in Fig. 7.2(b) around the peaks at $k = \pi/2a$. Such an asymmetry indicates that the maximum of n_k is not exactly at $k = \pi/2a$, but is shifted slightly. A more detailed analysis for $6 \leq U/t \leq 40$ is presented in Fig. 7.3. Figure 7.3(a) shows n_k around $k = \pi/2a$ with the data points from the t-DMRG calculations denoted by symbols and the connecting lines resulting from spline interpolations between them. It is clearly seen that the maximum of n_k is displaced to smaller momenta as U decreases. The spline interpolation allows for a better determination of the maxima in n_k , since a denser set of k -points corresponds to having a much longer lattice in a physical realization. On the other hand, the actual set of k -points in the t-DMRG simulation corresponding to $L = 60$ is dense enough to allow for a smooth inter-

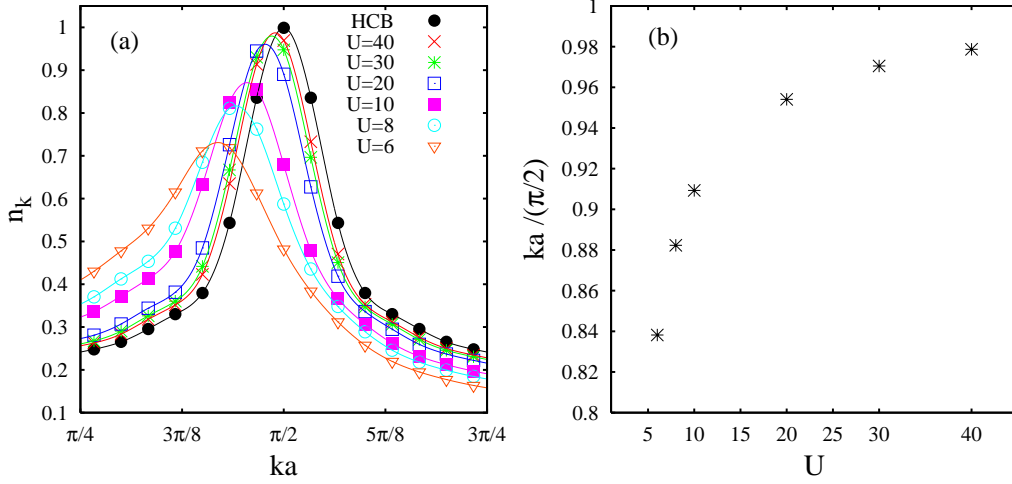


Figure 7.3: (a) The momentum distribution n_k at time $\tau = 4.5/t$ for different values of U/t . The symbols correspond to t-DMRG results on a lattice with $L = 60$, while the lines in the respective colors are spline interpolations. (b) The position of the peaks of the interpolated splines in n_k as a function of U/t .

pole without introducing artefacts due to the spline procedure. Figure 7.3(b) shows the location of the maxima of n_k as a function of U in units of $2a/\pi$, giving a guide for a fine tuning of the wavelength of the matter wave via the interaction strength.

7.2 Spatial Decay of Correlations

In order to see the establishment of coherence explicitly, we examine the spatial behavior of the one-particle density matrix. We would expect a change from an exponential decay in the Mott-insulating state to a power-law behavior if (quasi-)coherence emerges. Fig. 7.4 shows the spatial behavior of the one-particle density matrix both at time $\tau = 0$ [Fig. 7.4(a)], when bosons are in a Mott-insulating state, and at time $\tau \sim 7.5$ [Fig. 7.4(b)], when the peaks around $k = \pm\pi/2a$ are well established. Figure 7.4(a) shows the spatial dependence of the one-particle density matrix measured from the center of the bosonic region in a semi-logarithmic plot for different values of U . As expected for a Mott insulator, an exponential decay with a correlation length that shortens as U is increased is observed. Figure 7.4(b) shows the decay of the one-particle density matrix on a log-log scale at a time long enough so that the peaks around $k = \pm\pi/2a$ are fully developed. The evaluation was made in the part of the system where the lowest NO is appreciable, i.e., in the

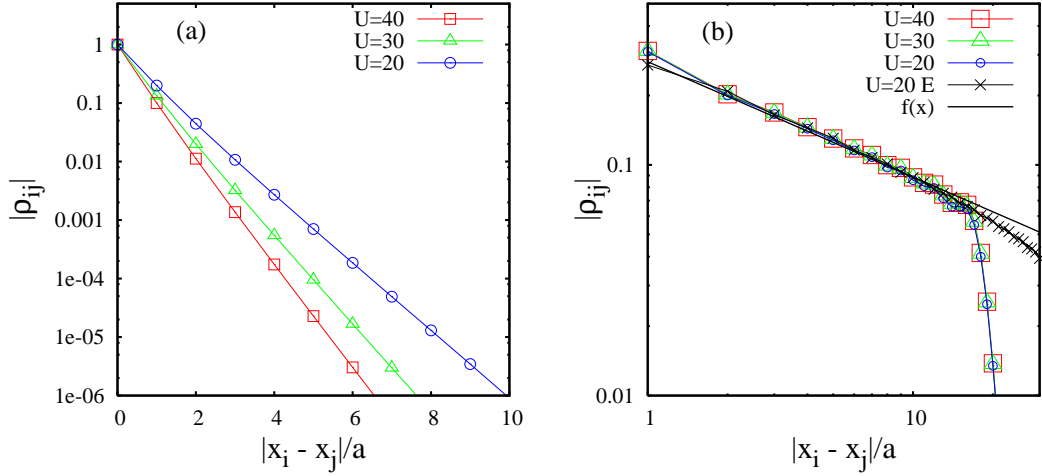


Figure 7.4: (a) Modulus of the one-particle density matrix ρ_{ij} versus distance $|x_i - x_j|$ in units of the lattice constant a at $\tau = 0$. (b) The same quantity at time $\tau = 7.38$, where the peaks in n_k are fully developed. Crosses ($U = 20E$) correspond to the one-particle density matrix in equilibrium for the same number of particles and system size. The black line corresponds to $f(x) \sim 1/\sqrt{|x_i - x_j|}$.

region of the system where a well developed quasi-condensate can be expected. Fig. 7.5 shows the spatial dependence of the lowest NO at the same time as in Fig. 7.4(b). The correlations in Fig. 7.4(b) were measured from the site $x_j = 37a$ (a position where the NO is well developed) and with $x_i > x_j$. For comparison, we superimpose the one-particle density matrix for $U/t = 20$, $N_b = 20$, and $L = 60$ in equilibrium, where, due to the lower density with respect to the initial state in Fig. 7.4(a), a quasi-condensate exists. Over the distances where the NO has an appreciable value, no difference with the corresponding quantity in equilibrium can be noticed. It can be clearly seen that the one-particle density matrix has developed a power-law decay (the same as the one in the system in equilibrium) at the later time, with a power that approaches the one of hard-core bosons. Unfortunately, the expansion of the cloud and the total system size are not as large in the soft-core as in the hard-core case, so that the exponent cannot be as accurately determined. Nevertheless, it is clear that a change from an exponential to a power-law decay takes place, indicating that a quasi-coherent matter wave has developed.

7.3 Conclusions

In this chapter, we have presented the non-trivial generalization of a nonequilibrium phenomenon originally found in systems of hard-core bosons that expand

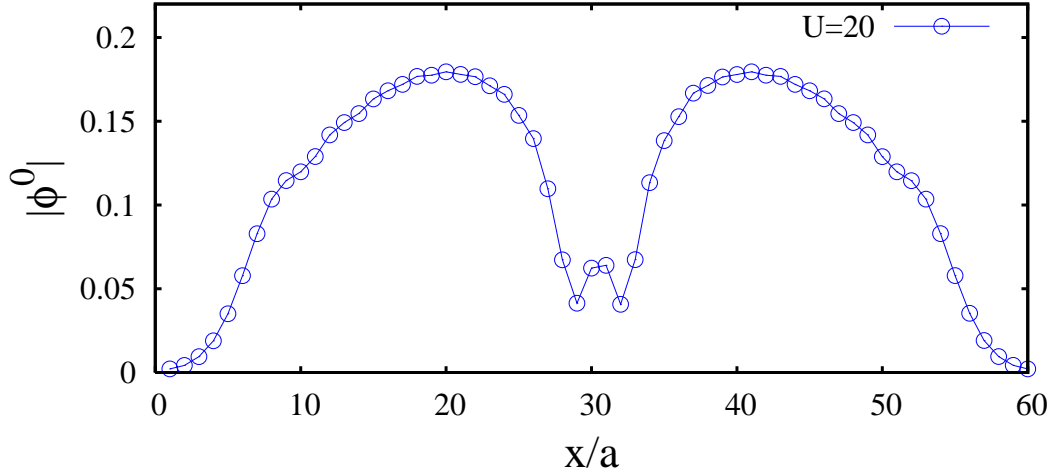


Figure 7.5: Spatial dependence of the lowest NO at time $t = 7.38$ for $U/t = 20$.

freely on a one-dimensional lattice. First, we have shown that, starting from a strongly correlated Mott-insulating state, the emergence of coherent matter waves at finite momenta persists away from the hard-core limit, i.e., to finite values of the on-site repulsion U which range down to the critical values, as long as a Mott-insulating state is attainable for the initial state. Although of relevance for experiments, the accurate treatment of this complicated many-body problem has not been possible – only the development of the t-DMRG enables us to carry out the investigation for systems large enough and times long enough so that predictions useful for experiments can be made. By comparing to exact results in the hard-core case, we have shown that our t-DMRG calculations, although approximate, are very reliable, as discussed in detail in Sec. 6.2.2. Two new features appear in the soft-core case: (i) Although the time evolution of the density profiles is indistinguishable from those of hard-core bosons at large values of U , the initial momentum distribution functions are markedly different. Nevertheless, after the Mott region melts, the momentum distribution functions of both systems become nearly identical. (ii) As the strength of the interaction is reduced, a shift of the momentum of the coherent matter wave to values smaller than $\pi/2a$ is observed. The appearance of a power law in the spatial decay of the one-particle density matrix demonstrates explicitly the (quasi-)coherent nature of the resulting matter wave. The results show that it is possible to engineer atom lasers with a high degree of control. The momentum of the coherent matter wave can first be regulated by setting the wavelength of the underlying optical lattice and further fine-tuned by regulating the depth of the potentials in the lattice, i.e., the intensity of the corresponding laser beam.

Chapter 8

Strongly Correlated Fermions after a Quantum Quench

As described in chapter 2, recent experiments on optical lattices have made it possible to investigate the behavior of strongly correlated quantum systems after they have been quenched. Such systems can be considered to be closed, i.e., they have no significant exchange of energy with a heat bath, so that energy is conserved to a very good approximation during the time evolution. As discussed in Sec. 2.5.1, since these systems are characterized by a large number of interacting degrees of freedom, application of the ergodic hypothesis leads to the expectation that the time average of observables should become equal to the thermal average after sufficiently long times. Various authors have recently given voice to such an expectation [76, 77, 78]. However, in Sec. 2.5.1 we have argued that relaxation to a thermal state is not expected to happen. This has been confirmed in an experiment on a one-dimensional optical lattice, where, however, the non-thermal behavior was ascribed to integrability [8]. Rigol *et al.* found that an integrable system of hard-core bosons relaxes to a state well-described by the generalized Gibbs-Boltzmann ensemble, Eq. (2.49), that takes into account the full set of integrals of motion [82]; similar results were found by Cazalilla for the integrable Luttinger model [84].

As discussed in Sec. 2.5.1, a non-thermal behavior is to be expected for both integrable as well as non-integrable systems. In this chapter, we investigate this by calculating the full time evolution of a strongly correlated system whose integrability can easily be destroyed by turning on an additional interaction term. Using the adaptive time-dependent density matrix renormalization group method (t-DMRG) introduced in chapter 6, we find that, in a certain parameter range, two different initial states with the same energy relax, to within numerical precision, to states with indistinguishable momentum distribution functions. A comparison with quantum Monte Carlo (QMC) simulations [176] shows that they do not cor-

respond to a thermal state. By using a generalized Gibbs ensemble, Eq. (2.49), we can improve the agreement with the time averages of the evolved system when using the expectation values of the powers of the Hamiltonian $\langle \hat{H}^n \rangle$ as constraints. This applies to both the integrable as well as to the non-integrable case.

We investigate spinless fermions on a one-dimensional lattice modelled by the Hamiltonian

$$\hat{H} = -t_h \sum_j (c_{j+1}^\dagger c_j + h.c.) + V \sum_j n_j n_{j+1}, \quad (8.1)$$

with nearest-neighbor hopping amplitude t_h (taken to be one) and nearest-neighbor interaction strength V at half-filling. The well-known ground-state phase diagram for the half-filled system consists of a Luttinger liquid (LL) for $V < V_c = 2t_h$, separated from a charge-density-wave (CDW) insulator ($V > V_c$) by a quantum critical point [177]. This model is integrable, with an exact solution via the Bethe Ansatz [15, 178]. We consider open chains of up to $L = 100$ sites pushed out of equilibrium by suddenly quenching the strength of V from an initial value $V(t = 0) = V_0$ to a different value $V(t > 0) = V$. Furthermore, we study the effect of adding a next-nearest-neighbor repulsion

$$V_2 \sum_j n_j n_{j+2} \quad (8.2)$$

to the model, which makes it non-integrable. We compute the time evolution using the Lanczos time-evolution method described in Sec. 3.2 and the adaptive t-DMRG. We study the momentum distribution function (MDF)

$$\langle n_k \rangle(t) = \frac{1}{L} \sum_{l,m=1}^L e^{ik(l-m)} \langle c_l^\dagger c_m \rangle(t), \quad (8.3)$$

i.e., the Fourier transform of the one-particle density matrix, $\rho_{lm} = \langle c_l^\dagger c_m \rangle$. In the t-DMRG, we utilize the Trotter approach developed in Refs. [107, 170] as well as the Lanczos approach [166, 179] with additional intermediate time steps added within each time interval [168]. We hold the discarded weight fixed to $\varepsilon \leq 10^{-9}$ during the time evolution, but additionally restrict the number of states kept to be in the range $100 \leq m \leq 1500$. A detailed error analysis of the t-DMRG for quantum quenches has been presented in Sec. 6.2.1. In all calculations presented in this chapter, the maximum error in the energy, which is a constant of motion, is 1%, and, in most cases, less than 0.1%, at the largest times reached.

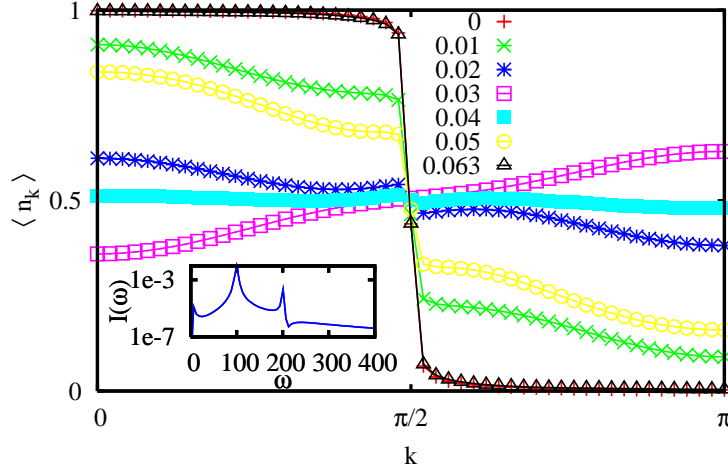


Figure 8.1: Time evolution of an initial LL state ($V_0 = 0.5$) in the strong coupling limit with $V = 100$ for $L = 100$ sites at the times indicated. Inset: spectral analysis of $\langle n \rangle(k = \pi)$.

8.1 The Strong Coupling Limit

When an initial Luttinger liquid state is quenched to the strong coupling regime, $V \gg t_h$, we find that $\langle n_k(t) \rangle$, displayed in Fig. 8.1, exhibits collapse and revival on short time scales, whereas the density-density correlation function remains essentially unchanged, i.e., retains the power-law decay of the LL. This can be understood by considering a quench to the atomic limit, $t_h = 0$. In this limit, the time evolution of an observable is given by

$$\langle O \rangle(t) = \langle \psi_0 | e^{itV \sum_j n_j n_{j+1}} O e^{-itV \sum_j n_j n_{j+1}} | \psi_0 \rangle, \quad (8.4)$$

i.e., all observables O that commute with the density operator, including the density-density correlation function, are time-independent. Furthermore, since the only remaining interaction is the nearest-neighbor density-density interaction, it can be shown analytically that the one-particle density matrix $\rho_{m,l}(t)$ involves only two frequencies ($\omega_1 = V$ and $\omega_2 = 2V$), resulting in a periodic oscillation with a revival time of $T_{\text{revival}} = 2\pi/V$. The exact expression is derived in Appendix B. Thus, in analogy to the observed collapse and revival of a BEC in an optical lattice [7], the single-particle properties of an initial LL state exhibit collapse and revival with this period. However, in the course of the time evolution, one- and two-particle propagators are not connected any more by only one anomalous dimension. As

discussed in Sec. 2.3, in Ref. [65], the *local* compressibility

$$\kappa_i^l = \sum_{|j| \leq l(V_{\text{trap}})} \left(\langle \hat{n}_i \hat{n}_{i+j} \rangle - \langle \hat{n}_i \rangle \langle \hat{n}_{i+j} \rangle \right) \quad (8.5)$$

can be used to characterize local quantum phases in non-homogeneous systems ($l(V_{\text{trap}})$ is estimated by the correlation length). In the atomic limit, this quantity does not change with time, while $\langle n_k \rangle(t)$ exhibits insulating behavior for times between two revivals, as displayed in Fig. 8.1. This shows that in non-equilibrium situations it is difficult to characterize a system as “metallic” or “insulating”.

8.2 Relaxation to a Non-Thermal Quasi-Stationary State

For small but finite hopping amplitudes, $t_h \ll V$, the time evolution retains the oscillatory behavior of the atomic limit; two frequencies ω_1 and ω_2 are indeed dominant in the spectrum, as can be seen in the inset of Fig. 8.1. However, the finite hopping amplitude leads to a dephasing of the oscillation on a time scale of $t_{\text{dephase}} \sim 1/t_h$. Afterwards, observables oscillate with a small amplitude around a fixed value, suggesting that the system reaches a quasi-stationary state.

In order to further characterize such states, we study the evolution of the system for various values of V . In Fig. 8.2, the momentum distribution function, obtained by performing an average in time from time $t = 3$ to $t = 10$, at the quantum critical point, $V = V_c$, and at a point in the CDW region, $V = 5t_h$, are shown. In order to investigate to what extent the (quasi-)stationary behavior is generic, we examine its dependence on the initial state. We do this by preparing two qualitatively different initial states with the same average energy $\langle H \rangle$ for each case: one a ground state in the LL regime and the other a ground state in the CDW regime. This is possible for a certain range of V in the intermediate coupling regime. In Fig. 8.2, results for two such initial states are compared with each other and with the MDF obtained for a system in thermal equilibrium and the same average energy, calculated using QMC simulations [176].

At the critical point, $V = V_c$, Fig. 8.2(a), the MDFs for the two initial states coincide with each other, to within the accuracy of the calculations (approximately the symbol size) or less. Therefore, information about the initial state is not preserved in this quantity, consistent with the expectation for an ergodic evolution. However, the difference from the thermal distribution is significant; thermalization is not attained. The left inset shows the time evolution of $\langle n_k \rangle(t)$ for $k = \pi$ for both initial conditions, demonstrating that the system reaches a quasi-stationary state. A small, but discernible shift from the thermal value can also be seen for

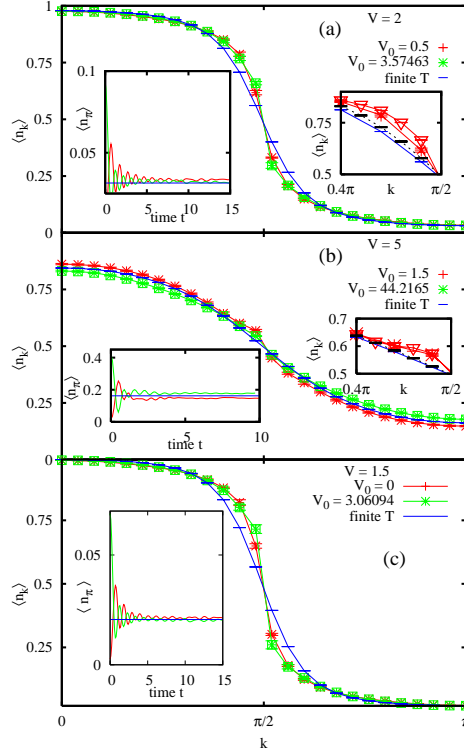
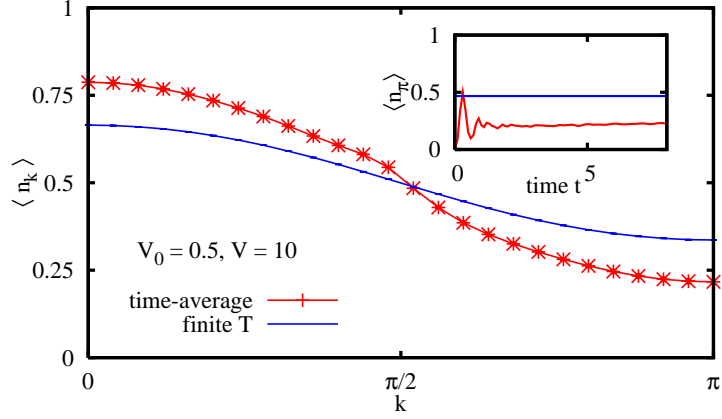


Figure 8.2: Time-averaged momentum distributions when quenching to (a) $V = 2$ (quantum critical point) and (b) $V = 5$ (insulator) for $L = 50$ sites. The time averages of two independent initial states with the same energy are compared to each other and to the thermal expectation value. In the right inset, results for $L = 50$ (*) are compared to $L = 100$ (∇). As a reference, the finite T results for $L = 50$ (blue lines) and $L = 100$ (dashed line) are shown. In (c), the results for a quench when remaining in the Luttinger liquid phase ($V = 1.5$) are shown.

both initial conditions, even at $k = \pi$. In the right inset, the points with the largest differences just below the Fermi vector $k_F = \pi/2$ are plotted when the system size is doubled from $L = 50$ to $L = 100$. As can be seen, the finite-size effects are of the order of the symbol size or smaller and do not affect the conclusions.

In order to investigate the importance of quantum criticality, we have also examined the behavior for $V = 1.5$ and $V = 2.5$, i.e., below and above the transition point. We find almost identical behavior, indicating that the lack of thermalization is not associated with the quantum critical point. Note, however, that the LL regime ($V < 2$) is critical.

For $V = 5$, Fig. 8.2 (b), all three curves show small, but significant differences. This means that the time evolution starting from different initial states can

Figure 8.3: Time-averaged momentum distribution $\langle n_k \rangle$ for $V=10$.

be distinguished from each other as well as from the thermal state, i.e., neither relaxation to one distinguished quasi-stationary state nor thermalization occurs. For this case, $|V_0 - V|$ is larger than for $V = 2$, and, in addition, the values of V_0 necessary to obtain the same energy in the initial state ($V_0 = 1.5$ and $V_0 = 44.2165$) differ strongly. This suggests that the initial states are far apart from each other in some sense, a notion that will be made more precise below.

The differences with the thermal distribution increase for larger $|V_0 - V|$. As can be seen in Fig. 8.3 for $V = 10$, the difference between the time average and the thermal distribution is significant, clearly confirming that thermalization does not occur. The differences observed increase gradually as a function of $|V_0 - V|$, ruling out a transition, as suggested for the Bose-Hubbard model [78].

In order to investigate the impact of the lack of integrability on thermalization, we now extend our model (8.1) by turning on a next-nearest-neighbor interaction. In Fig. 8.2, we display results with $V_0 = 0.5$ and $V_0 = 2.46689$ (zero n.n.n. interaction), and the quenched evolution at $V = 2$, $V_2 = 0.4$. As in the integrable case, both initial states lead to indistinguishable time-averaged MDF's, but significantly different from the thermal one, showing differences very similar to those in Figs. 8.2 (a). When $V_0 = 0.5$ and $V = 10$, $V_2 = 1$, the difference from the thermal state is comparable to the case shown in Fig. 8.3. Therefore, the non-thermal nature of the emerging steady state is clearly *not* related to the integrability of the system.

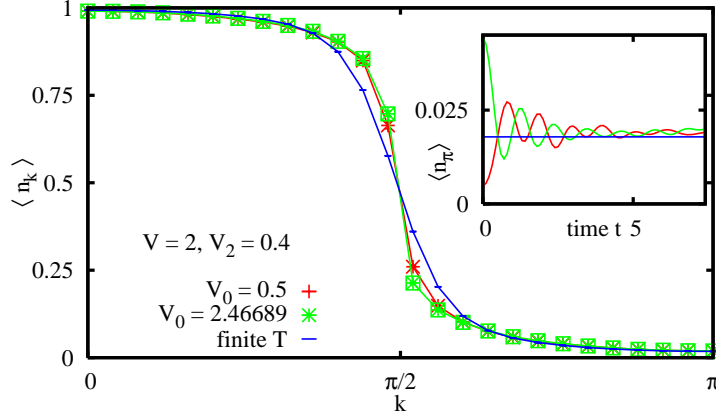


Figure 8.4: Comparison of finite- T data and time-averaged values of the momentum distribution $\langle n_k \rangle$ for the non-integrable case with $V = 2$ and $V_2 = 0.4$.

8.3 Application of the Generalized Gibbs Ensemble

In Sec. 2.5.1, we discussed the use of a generalized Gibbs ensemble taking into account powers of H as constraints,

$$\varrho = \exp \left[- \sum_n \lambda_n H_n \right]. \quad (8.6)$$

The values of the λ_n are fixed by the condition that $\text{Tr}(\varrho H^n) = \langle H^n \rangle$, taking $H^0 = 1$ to enforce normalization. Here, ϱ is fully determined by $\dim(H)$ powers of H . The statistical expectation value of any observable is then given (for a non-degenerate spectrum) by

$$\text{Tr}(\varrho O) = \sum_{\nu} |\langle \nu | \psi_0 \rangle|^2 \langle \nu | O | \nu \rangle, \quad (8.7)$$

with $|\nu\rangle$ the eigenstates of H . As discussed in Sec. 2.5.1, the r.h.s. of this expression is equal to the time average of $\langle \hat{O} \rangle(t)$.

For Hamiltonian (8.1) with $L = 16$ sites, we can follow the time evolution to long times by carrying out a full diagonalization. We find that the time average does not change when the time range is increased from $t \leq 10$ to $t \leq 100$ and that this average agrees with $\text{Tr}(\varrho O)$. This is shown in Fig. 8.5. Although the available times are limited to $t \sim 10$ for the larger systems accessible to the t-DMRG, comparison with the $L = 16$ results yields qualitative and rough quantitative agreement of the time averages for the times available. This provides some evidence that the quasi-stationary state found using the t-DMRG will not change

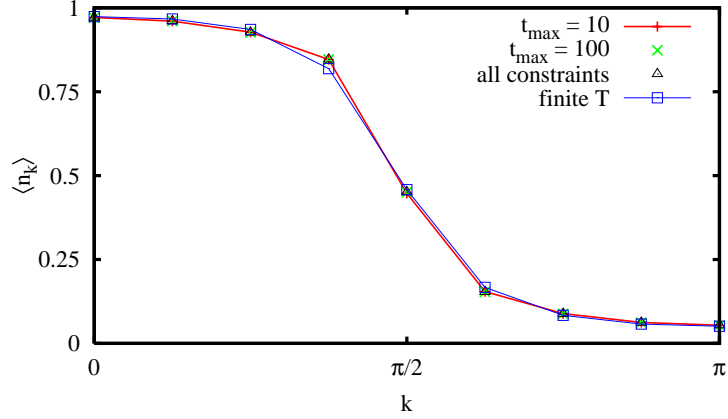


Figure 8.5: Comparison of time averages for times between $t = 3$ and $t_{\max} = 10$ and $t_{\max} = 100$ with the statistical average of Eq. (8.7) and with a thermal state for a quench with $V_0 = 0.5$ and $V = 2$ for a system with $L = 16$ sites. Note that the results presented are obtained using full diagonalization of the Hamiltonian and have, therefore, an error much smaller than the symbol size.

strongly on larger time scales. Note that the accuracy of the results presented in Fig. 8.5 is of the order of the machine precision. Although the results are very similar to each other, a clear difference remains which would be better visible if more k -points closer to k_F would be available.

We now investigate the extent to which the statistical expectation value within the generalized Gibbs ensemble approaches the time average of the evolution after a quench by studying the energy distribution, defined as

$$P_\psi(E) = \sum_\nu \delta(E - \epsilon_\nu) |\langle \nu | \psi \rangle|^2, \quad (8.8)$$

which is normalized if $\langle \psi | \psi \rangle = 1$. The energy distribution in the generalized Gibbs ensemble can analogously be defined as $P_G(E) = \text{Tr} \delta(E - H) \rho$, with ρ as defined previously. In Fig. 8.6, we show $P_\psi(E)$ calculated using full diagonalization on $L = 16$ sites for an initial state $V_0 = 0.5$ evolved at the quantum critical point, $V = 2$, compared with the distribution in the Gibbs ensemble $P_G(E)$ as the number of constraints is increased from 1 to 3. It is evident that increasing the number of constraints systematically improves the agreement and that only a small number of moments are necessary to obtain very good agreement, at least for this case.

A quantitative measure of the distance Δ of two different quench situations can

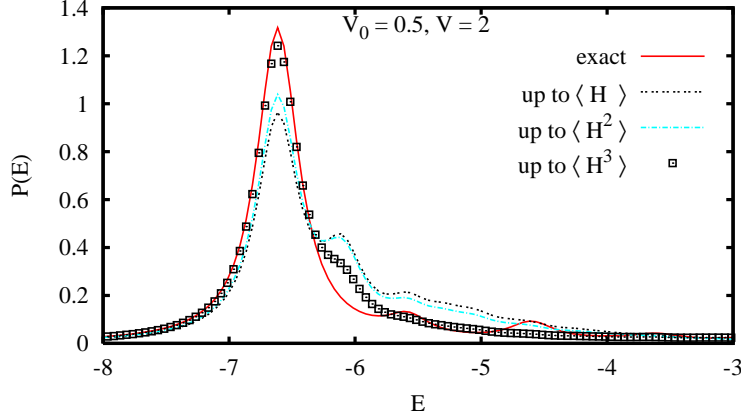


Figure 8.6: Influence of the constraints $\langle H^n \rangle$ on the energy distribution function $P(E)$.

be introduced as

$$\Delta = \int dE |P(E) - P'(E)|. \quad (8.9)$$

Based on this, we take as an estimate the distance of two distributions as $|P(E) - P'(E)| = \Delta/W$, where W is the bandwidth of the spectrum of H . For the moments of H for two different energy distributions P and P' , we have

$$\begin{aligned} \langle \hat{H}^n \rangle_P - \langle \hat{H}^n \rangle_{P'} &= \int dE E^n \{P_\psi(E) - P_{\psi'}(E)\} \\ &\leq \int dE E^n |P_\psi(E) - P_{\psi'}(E)| \\ &\simeq \frac{1}{n+1} W^n \Delta. \end{aligned} \quad (8.10)$$

Therefore, if the distance of the distributions $\Delta \ll 1$, the relative distance of the moments $(\langle \hat{H}^n \rangle_P - \langle \hat{H}^n \rangle_{P'})/W^n < \Delta/(n+1)$ will also remain small, such that the values of the observables after a quench converge to values close to each other. Estimating Δ for the respective two initial states of Fig. 8.2, albeit in smaller systems with $L = 16$, we obtain for the case of Fig. 8.2 (a), $\Delta = 0.12439$, for Fig. 8.2 (b), $\Delta = 0.41521$, and for Fig. 8.2 (c), $\Delta = 0.16752$. On the other hand, the comparison of P_ψ and the thermal distribution P_β leads to $\Delta = 0.68581$, $\Delta = 1.24616$, and $\Delta = 0.71432$, respectively. Thus, the distance between the thermal distribution and the one defined by the initial states is always larger than those defined by the pair of initial states with the same energy, in accordance with the observation that a non-thermal quasi-stationary state is reached.

8.4 Discussion

In this chapter, we have investigated the short-time behavior and the relaxation of an initial Luttinger liquid state after a quantum quench. Using the adaptive time-dependent DMRG, we have been able to investigate systems and times large enough to find the quasi-stationary state. In the atomic limit, we find collapse and revival of the initial Luttinger liquid state. This persists in the strong coupling limit $t_H \ll V$, but due to the finite hopping amplitude, relaxation on a time scale $\sim 1/t_h$ is obtained. In the general case, independent of the integrability of the system, the emerging quasi-stationary state is non-thermal. The time average is identical to expectation values with a generalized Gibbs ensemble when considering $\dim(H)$ powers of H as constants of the motion, as following from Eq. (2.54). Under certain conditions, independent initial conditions relax to the same quasi-stationary state which can, in turn, be very close to a thermal state. This can be quantified using a measure Δ , which we have calculated on small systems for various pairs of V_0 and V .

Chapter 9

Summary and Conclusion

In this thesis, we have studied strongly correlated quantum systems on one-dimensional lattices in equilibrium and out-of-equilibrium situations. We have demonstrated that it is possible to extend well-established numerical methods like the Lanczos method, discussed in Chapter 3, and the DMRG, treated in detail in Chapter 4, to handle non-equilibrium systems with a high accuracy. The Lanczos time-evolution method can be applied in such a way that the errors become of the order of the machine precision. For the DMRG, we have discussed in chapter 6 two possible variants of algorithms for *adaptive* time-dependent DMRG procedures. The first approach is based on the Lanczos time-evolution method introduced in Sec. 3.2. The second approach uses a Trotter-Suzuki decomposition of the time-evolution operator in a quite clever way. In Sec. 6.2, both approaches are shown to have errors in the observables that are $< 1\%$ at the end of the time-evolution. For quantum quenches with an initial state with a homogeneous distribution of the particles on the lattice, we find that for a suitable choice of control parameters, the Trotter approach is faster while the error of both approaches is comparable. For a system of particles released from an initial trap, we find the Lanczos variant to be more accurate. Thus, both variants represent powerful tools to treat non-equilibrium situations of quasi one-dimensional strongly correlated quantum systems.

In chapter 5, we have applied the usual DMRG method to elucidate the quantum critical behavior of the ionic Hubbard model in one spatial dimension. We find strong indications for a scenario with *two* critical points, in accordance with a calculation using a bosonization Ansatz [12]. The critical points are characterized by the closing of gaps and by the divergence of the electric and the bond-order susceptibilities. We find that, at the first critical point, only charge degrees of freedom become critical, while the second transition point is associated with a closing of the spin gap. We find that at the first critical point a second order transition takes

place, albeit with values of the exponents different from the Ising values, which were proposed in Ref. [12]. The second transition is also continuous and possibly of Kosterlitz-Thouless type, although it is difficult to clarify this point.

Using the adaptive t-DMRG, we have investigated two non-equilibrium situations:

In chapter 7 we have found an emerging (quasi-)coherent matter wave of soft-core bosons with a wavevector that depends on the interaction strength. This demonstrates that it is possible to engineer atom lasers on optical lattices using soft-core bosons.

In chapter 8 we have investigated the time evolution of a strongly correlated fermion system after a quantum quench. The system is integrable using the Bethe Ansatz, but can easily be made non-integrable by adding an additional next-nearest-neighbor interaction. In the strong coupling limit, we find collapse and revival of an initial Luttinger liquid state on short time scales. After a typical time of the order of $\sim 1/t_h$, where t_h is the nearest neighbor hopping amplitude, we find relaxation to a quasi-stationary state, i.e., the observables oscillate around an average with an amplitude which is much smaller than the amplitude at the beginning of the time evolution. According to Boltzmann's ergodic hypothesis, thermalization might be expected. However, as discussed in Sec. 2.5.1, the emergent quasi-stationary state after a quantum quench is expected to be *non-thermal*. This is independent of the integrability and the dimensionality of the system. However, for certain parameters, we find that two different initial states with the same energy are found to relax to the same non-thermal quasi-stationary state, and that the obtained quasi-stationary state for certain parameters can be quite close to a thermal state. The difference is small, so that in experiments it may be difficult to distinguish it from a thermal state. By considering $\dim(H)$ powers of the Hamiltonian H as constants of the motion, it is, basing on Jayne's principle of maximum entropy, possible to formulate a generalized Gibbs-Boltzmann ensemble. We find that the statistical expectation value then is equal to the time average, showing that emergent quasi-stationary state can, indeed, be described by a density-matrix.

The investigation of strongly-correlated quantum systems out of equilibrium is at its beginnings. With the methods developed in this thesis, it is possible to investigate a large class of non-equilibrium situations and exciting new results are expected. For example, considering the successful application of the ground-state DMRG to systems of coupled chains, the treatment of non-equilibrium situations for systems that are not purely one-dimensional should be possible. This is of particular interest for a better understanding of the relaxation dynamics of quantum many-body systems. Although, as discussed in this thesis, the final state is non-thermal, experiments on optical lattices seem to indicate that in higher di-

mensional systems thermalization is obtained within resolution of the methods [180]. Therefore, further theoretical investigations on this issue are necessary which should be, at least partially, possible with the new methods available. It is also of interest for experiments to consider the emergence of coherent matter waves on systems beyond one spatial dimension. An investigation is on the way [181].

Further examples for possible applications of the new methods can be found in the field of ultrafast processes. The advent of femtosecond and even *attosecond* spectroscopy [182] opens new possibilities to investigate elementary processes, e.g., in chemical reactions. We expect that the numerical methods developed in this work should be helpful to gain theoretical insight into experimental results. This is also valid for experiments on optical lattices, where a combination of our numerical approaches with the excellent possibilities of controlling the experiments promises new developments and insights into the non-equilibrium dynamics of strongly correlated quantum systems. Our knowledge about the behavior of quantum many-body systems in non-equilibrium situations is very limited; we believe that the development of the numerical methods discussed in this thesis will contribute to change this situation.

Appendix A: Details to the t-DMRG

In this appendix, we show the time dependence of the number m of density-matrix basis states kept during the time-evolution and of the discarded weight ϵ when performing the t-DMRG runs with a variable m and a fixed ϵ , but a maximum number m_{\max} of kept basis states. In Figs. 1 and 2, the analysis for a quench is shown. In Fig. 3, the case of initially trapped hard-core bosons is shown.

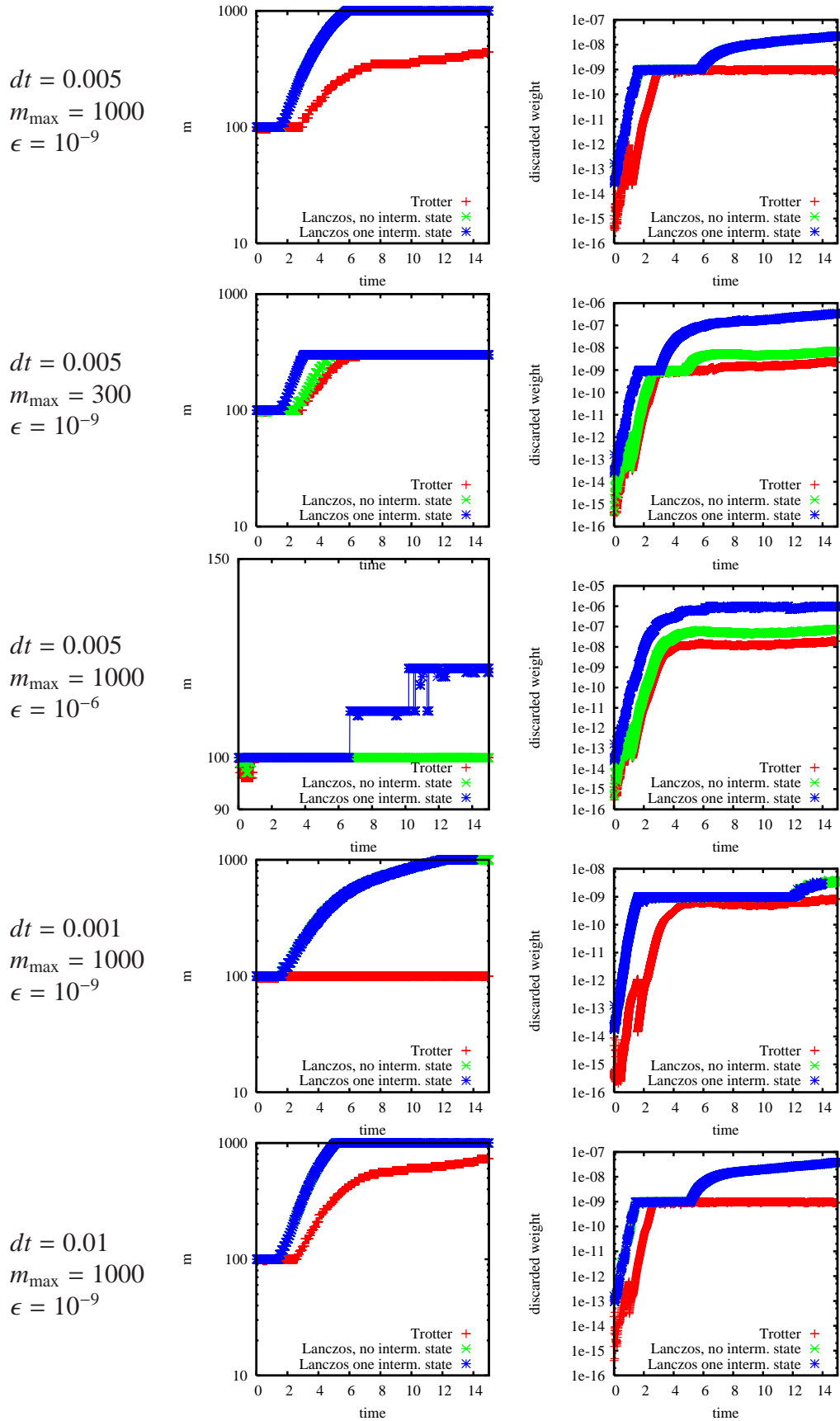


Figure 1: Time dependence of the number of density-matrix eigenstates kept (left column) and of the discarded weight (right column) for the various sets of parameters for a quench with $V = 2$.

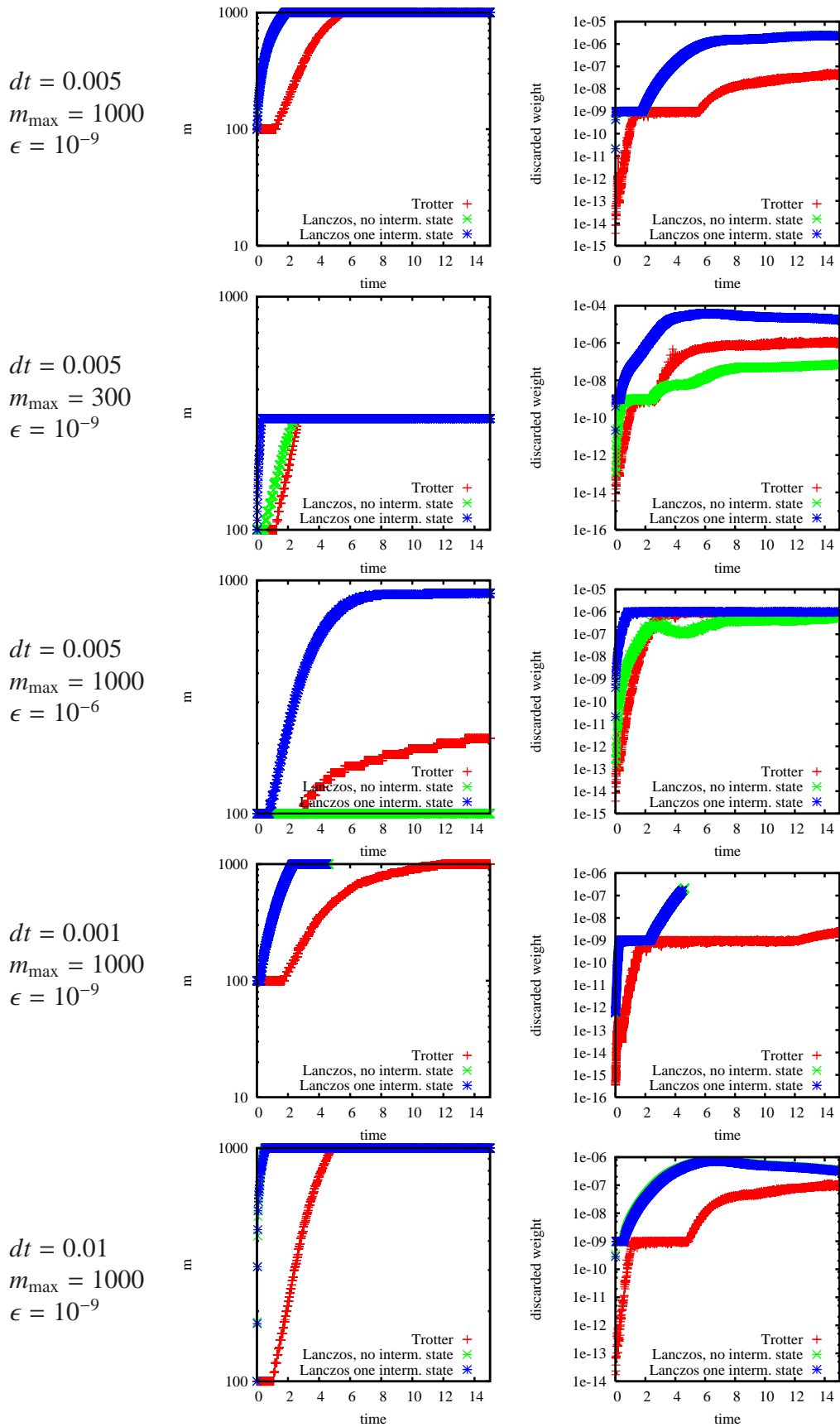


Figure 2: Time dependence of the number of density-matrix eigenstates kept (left column) and of the discarded weight (right column) for the various sets of parameters for a quench with $V = 40$.

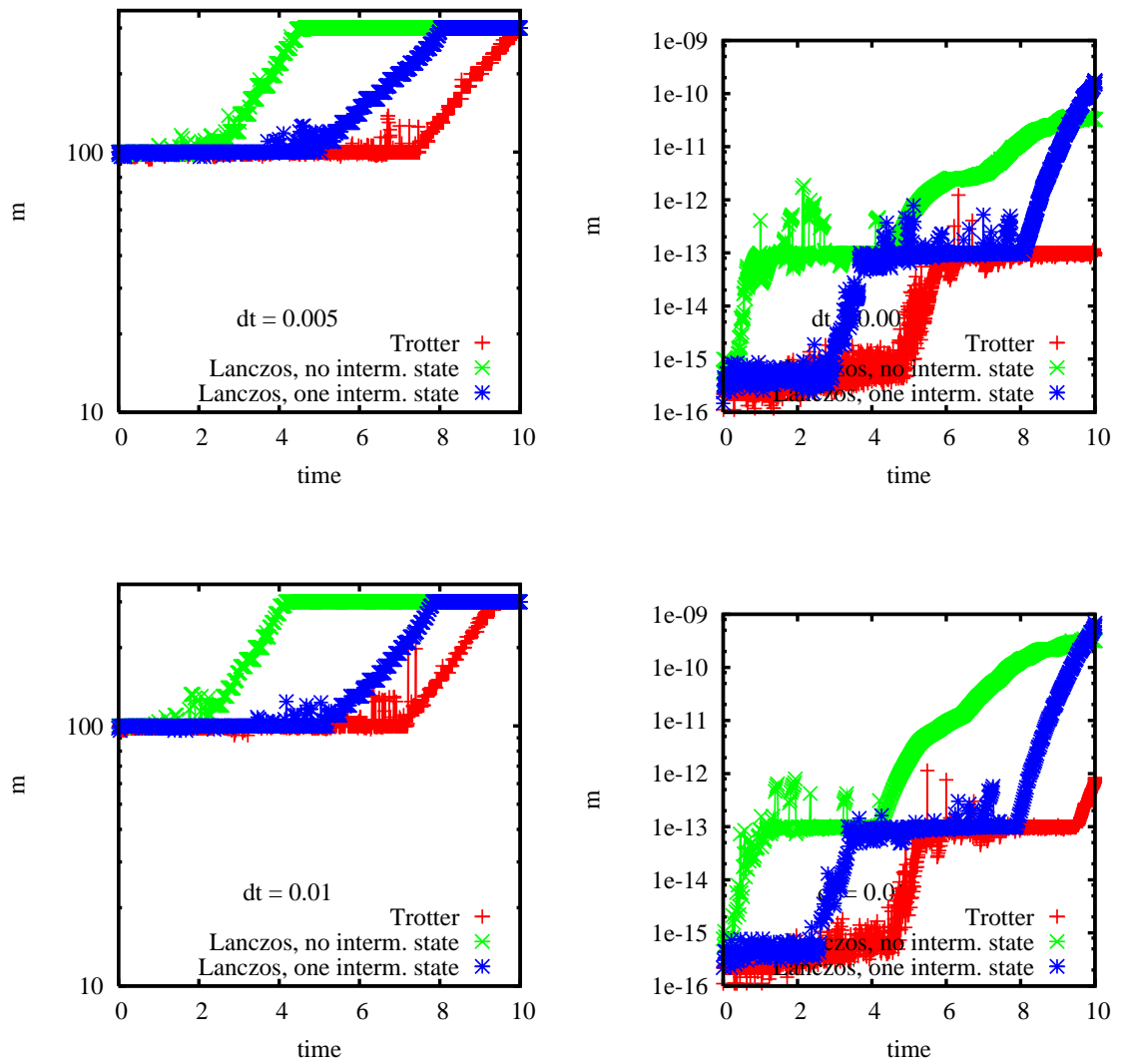


Figure 3: The same analysis as before for a system of initially trapped $N = 20$ hard-core bosons on a lattice with $L = 60$ sites.

Appendix B: Time Dependence of the OPDM after a Quantum Quench in the Atomic Limit

In this appendix, we present the detailed calculation of the time evolution of the one-particle density matrix (OPDM) for a system of spinless fermions, when at later times the hopping is set to zero. As a starting point, we consider the time evolution of an arbitrary observable

$$\langle \hat{O} \rangle(t) = \langle \psi_0 | e^{iVt \sum_j n_j n_{j+1}} \hat{O} e^{-iVt \sum_{j'} n_{j'} n_{j'+1}} | \psi_0 \rangle \quad (1)$$

$$= \langle \psi_0 | \prod_j e^{iVt n_j n_{j+1}} \hat{O} \prod_{j'} e^{-iVt n_{j'} n_{j'+1}} | \psi_0 \rangle \quad (2)$$

Therefore, *all* observables \hat{O} which commute with the density operator $n_i \equiv c_i^\dagger c_i$ are time independent. However, one-particle propagators, like the OPDM, are time dependent due to the fermionic commutation relations. The elements of the OPDM evolve in time according to

$$\varrho_{ml}(t) = \langle \psi_0 | \prod_\mu e^{iVt n_\mu n_{\mu+1}} c_m^\dagger c_l \prod_\nu e^{-iVt n_\nu n_{\nu+1}} | \psi_0 \rangle \quad (3)$$

For the detailed calculation, we need to consider various cases:

1.) $m = l$: $\Rightarrow \varrho_{ml}(t) = \text{const.}$

2.) $|m - l| > 1$:

If $\mu \neq m, l$ and $\mu + 1 \neq m, l$, the operator $e^{iVt n_\mu n_{\mu+1}}$ commutes with $c_m^\dagger c_l$ and will find a ‘‘partner’’ in the product over ν , such that the contribution of these two operators reduces to a factor 1. Since this happens for most values of μ and ν , as

intermediate result we obtain

$$\Rightarrow \varrho_{ml}(t) = \langle e^{iVt n_m n_{m+1}} e^{iVt n_{m-1} n_m} e^{iVt n_l n_{l+1}} e^{iVt n_{l-1} n_l} c_l^\dagger c_m e^{-iVt n_m n_{m+1}} e^{-iVt n_{m-1} n_m} e^{-iVt n_l n_{l+1}} e^{-iVt n_{l-1} n_l} \rangle \quad (4)$$

The operator $n_m n_{m+1}$ is idempotent:

$$(n_m n_{m+1})^a = n_m n_{m+1}, \quad a \in \mathbb{N}$$

This leads to the following useful relation:

$$\begin{aligned} e^{-iVt n_{m-1} n_m} &= 1 + \sum_{a=1}^{\infty} \frac{(-iVt)^a}{a!} (n_m n_{m+1})^a \\ &= 1 + n_m n_{m+1} \underbrace{(e^{-iVt} - 1)}_{\equiv T} \end{aligned} \quad (5)$$

With this, we can calculate the commutation of the remaining time-evolution operators with the operator $c_l^\dagger c_m$. For example we obtain (with $\bar{T} = e^{iVt} - 1$)

$$\begin{aligned} e^{iVt n_{l-1} n_l} c_l^\dagger c_m &= [1 + n_{l-1} n_l \bar{T}] c_l^\dagger c_m \\ &= c_l^\dagger c_m + \bar{T} n_{l-1} c_l^\dagger \underbrace{c_l c_l^\dagger}_{=1-n_l} c_m \\ &= c_l^\dagger c_m + \bar{T} c_l^\dagger c_m n_{l-1} - \bar{T} n_{l-1} \underbrace{c_l^\dagger c_l}_{\rightarrow 0} c_m \\ &= c_l^\dagger c_m (1 + \bar{T} n_{l-1}) \\ &= c_l^\dagger c_m e^{iVt n_{l-1}}, \end{aligned}$$

where in the last line we used the fact that, according to Eq. (5), for any idempotent operator n the equality $e^{an} = 1 + n(e^a - 1)$. Similarly, we obtain

$$e^{iVt n_{l+1} n_l} c_l^\dagger c_m = c_l^\dagger c_m e^{iVt n_{l+1}} \quad (6)$$

$$e^{iVt n_{m+1} n_m} c_l^\dagger c_m = c_l^\dagger c_m \quad (7)$$

$$e^{iVt n_{m-1} n_m} c_l^\dagger c_m = c_l^\dagger c_m \quad (8)$$

$$c_l^\dagger c_m e^{-iVt n_m n_{m+1}} = e^{-iVt n_{m+1}} c_l^\dagger c_m \quad (9)$$

$$c_l^\dagger c_m e^{-iVt n_{m-1} n_m} = e^{-iVt n_{m-1}} c_l^\dagger c_m \quad (10)$$

$$c_l^\dagger c_m e^{-iVt n_l n_{l+1}} = c_l^\dagger c_m \quad (11)$$

$$c_l^\dagger c_m e^{-iVt n_{l-1} n_l} = c_l^\dagger c_m \quad (12)$$

$$(13)$$

The time-dependence of the elements of the one-particle density-matrix is thus given by

$$\begin{aligned}
Q_{ml}(t) &= \langle e^{iVtn_{l+1}} e^{iVtn_{l-1}} c_l^\dagger c_m e^{-iVtn_{m+1}} e^{-iVtn_{m-1}} \rangle \\
&= \langle [1 + n_{m+1}T] [1 + n_{m-1}T] [1 + n_{l+1}\bar{T}] [1 + n_{l-1}\bar{T}] c_l^\dagger c_m \rangle \\
&= \langle [1 + T(n_{m+1} + n_{m-1}) + T^2 n_{m+1} n_{m-1}] [1 + \bar{T}(n_{l+1} + n_{l-1}) + \bar{T}^2 n_{l+1} n_{l-1}] c_l^\dagger c_m \rangle \\
&= \langle c_l^\dagger c_m \rangle \\
&\quad + T \langle (n_{m+1} + n_{m-1}) c_l^\dagger c_m \rangle \\
&\quad + \bar{T} \langle (n_{l+1} + n_{l-1}) c_l^\dagger c_m \rangle \\
&\quad + T^2 \langle n_{m+1} n_{m-1} c_l^\dagger c_m \rangle \\
&\quad + T\bar{T} \langle (n_{m-1} n_{l-1} + n_{l+1} n_{m-1} + n_{m+1} n_{l-1} + n_{m+1} n_{l+1}) c_l^\dagger c_m \rangle \\
&\quad + \bar{T}^2 \langle n_{l+1} n_{l-1} c_l^\dagger c_m \rangle \\
&\quad + T^2 \bar{T} \langle (n_{l-1} n_{m+1} n_{m-1} + n_{l+1} n_{m+1} n_{m-1}) c_l^\dagger c_m \rangle \\
&\quad + T\bar{T}^2 \langle (n_{m-1} n_{l+1} n_{l-1} + n_{m+1} n_{l+1} n_{l-1}) c_l^\dagger c_m \rangle \\
&\quad + T^2 \bar{T}^2 \langle n_{m+1} n_{m-1} n_{l+1} n_{l-1} c_l^\dagger c_m \rangle
\end{aligned}$$

with

$$\begin{aligned}
T &= (e^{-iVt} - 1) \\
\bar{T} &= (e^{iVt} - 1) \\
T^2 &= e^{-2itV} - 2e^{-itV} + 1 \\
\bar{T}^2 &= e^{2itV} - 2e^{itV} + 1 \\
T\bar{T} &= 2(1 - \cos(tV)) \\
T^2\bar{T} &= 2(\cos(tV) - 1) - (e^{-itV} - 1)^2 \\
T\bar{T}^2 &= 2(\cos(tV) - 1) - (e^{itV} - 1)^2 \\
T^2\bar{T}^2 &= 2(3 - 4\cos(tV) + \cos(2tV))
\end{aligned}$$

Thus the time-evolution of the density matrix is governed by only two frequencies $\propto 1/V$ and $\propto 1/2V$.

3.) $m = l \pm 1$:

We will perform the calculation for $m = l + 1$ – the other case is analogous.

Starting point is again

$$\varrho_{mm+1}(t) = \langle \psi_0 | \prod_{\mu} e^{iVt n_{\mu} n_{\mu+1}} c_m^{\dagger} c_{m+1} \prod_{\nu} e^{-iVt n_{\nu} n_{\nu+1}} | \psi_0 \rangle \quad (14)$$

For $\mu \neq m, m+1$ and $\mu+1 \neq m, m+1$, the time evolution operators on the right commute with $c_m^{\dagger} c_{m+1}$ and do not contribute to the time evolution. This leads to the simplified expression

$$\varrho_{mm+1} = \langle e^{iVt n_m n_{m+1}} e^{iVt n_{m+1} n_{m+2}} e^{iVt n_m n_{m-1}} c_m^{\dagger} c_{m+1} e^{-iVt n_m n_{m+1}} e^{-iVt n_{m+1} n_{m+2}} e^{-iVt n_m n_{m-1}} \rangle \quad (15)$$

Similar to the above step, the time-evolution operators are further simplified, leading to the expression

$$\begin{aligned} \varrho_{mm+1}(t) &= \langle e^{iVt n_{m-1}} c_m^{\dagger} c_{m+1} e^{-iVt n_{m+2}} \rangle \\ &= \langle c_m^{\dagger} c_{m+1} \rangle \\ &\quad + (e^{itV} - 1) \langle n_{m+2} c_m^{\dagger} c_{m+1} \rangle \\ &\quad + (e^{-itV} - 1) \langle n_{m-1} c_m^{\dagger} c_{m+1} \rangle \\ &\quad + 2(1 - \cos(tV)) \langle n_{m-1} n_{m+2} c_m^{\dagger} c_{m+1} \rangle \end{aligned}$$

An analogous calculation for $l = m - 1$ leads to

$$\varrho_{m m-1}(t) = \langle e^{itV n_{m+1}} c_m^{\dagger} c_{m-1} e^{-itV n_{m-2}} \rangle \quad (16)$$

Thus, the time-evolution of the next-to-diagonal elements of ϱ is governed by only one frequency $\propto 1/V$.

The time-evolution of the momentum distribution is obtained as the Fourier transform of the OPDM,

$$n(k, t) = \frac{1}{L} \sum_{m,l=1}^L e^{-ik(l-m)} \varrho_{ml}(t) . \quad (17)$$

Thus, considering the obtained expressions for $\varrho_{ml}(t)$, it is also governed by only two frequencies $\propto 1/V$ and $\propto 1/(2V)$.

Bibliography

- [1] S. R. WHITE, *Phys. Rev. Lett.* **69**, 2863 (1992).
- [2] I. PESCHEL, X. WANG, M. KAULKE, and K. HALLBERG, editors, *Density Matrix Renormalization - A New Numerical Method in Physics*, Berlin, 1999, Springer Verlag.
- [3] U. SCHOLLWÖCK, *Rev. Mod. Phys.* **77**, 259 (2005).
- [4] R. M. NOACK and S. R. MANMANA, *AIP Conf. Proc.* **789**, 93 (2005).
- [5] I. BLOCH, *Nature Physics* **1**, 23 (2005).
- [6] M. GREINER, O. MANDEL, T. ESSLINGER, T. W. HÄNSCH, and I. BLOCH, *Nature* **415**, 39 (2002).
- [7] M. GREINER, O. MANDEL, T. W. HÄNSCH, and I. BLOCH, *Nature* **419**, 51 (2002).
- [8] T. KINOSHITA, T. WENGER, and D. S. WEISS, *Nature* **440**, 900 (2006).
- [9] L. E. SADLER, J. M. HIGBIE, S. R. LESLIE, M. VENGALATTORE, and D. M. STAMPER-KURN, *Nature* **443**, 312 (2006).
- [10] M. SUZUKI, *Prog. Theor. Phys.* **56**, 1454 (1976).
- [11] M. HOCHBRUCK and C. LUBICH, *SIAM J. Numerical Anal.* **Vol. 34**, pp 1911 (1997).
- [12] M. FABRIZIO, A. GOGOLIN, and A. NERSESYAN, *Phys. Rev. Lett.* **83**, 2014 (1999).
- [13] M. RIGOL and A. MURAMATSU, *Phys. Rev. Lett.* **93**, 230404 (2004).
- [14] B. PAREDES, A. WIDERA, V. MURG, O. MANDEL, S. FÖLLING, I. CIRAC, G. V. SHLYAPNIKOV, T. W. HÄNSCH, and I. BLOCH, *Nature* **429**, 277 (2004).

- [15] H. BETHE, *Z. Phys.* **71**, 205 (1931).
- [16] K. G. WILSON, *Rev. Mod. Phys.* **47**, 773 (1975).
- [17] N. W. ASHCROFT and N. D. MERMIN, *Solid State Physics*, Thomson Learning, 1976.
- [18] J. W. NEGELE and H. ORLAND, *Quantum Many-Particle Systems*, Addison-Wesley Publishing Group, 1988.
- [19] R. P. FEYNMAN, *Int. J. Theor. Phys.* **21**, 467 (1982).
- [20] R. P. FEYNMAN, *Found. Phys.* **16**, 507 (1985).
- [21] R. P. FEYNMAN, *Optics News* **11**, 11 (February 1985).
- [22] The ALPS collaboration (F. Alet. *et al.*), *J. Phys. Soc. Jpn. Suppl.* **74**, 30 (2005).
- [23] <http://alps.comp-phys.org>.
- [24] M. C. GUTZWILLER, *Chaos in Classical and Quantum Mechanics*, Springer, 1990.
- [25] J. HUBBARD, *Proc. R. Soc. (London) A* **276**, 238 (1963).
- [26] M. C. GUTZWILLER, *Phys. Rev. Lett.* **10**, 159 (1963).
- [27] J. KANAMORI, *Prog. Theor. Phys.* **30**, 275 (1963).
- [28] F. H. L. ESSLER, H. FRAHM, F. GÖHMANN, A. KLÜMPER, and V. E. KOREPIN, *The One-Dimensional Hubbard Model*, Cambridge University Press, 2005.
- [29] A. AUERBACH, *Interacting Electrons and Quantum Magnetism*, Springer, New York, 1994.
- [30] P. JORDAN and E. WIGNER, *Z. Phys.* **47**, 631 (1928).
- [31] M. P. A. FISHER, P. B. WEICHMAN, G. GRINSTEIN, and D. S. FISHER, *Phys. Rev. B* **40**, 546 (1989).
- [32] T. D. KÜHNER, S. R. WHITE, and H. MONIEN, *Phys. Rev. B* **61**, 12474 (2000).
- [33] M. RIGOL, *Numerically Exact Studies of Ultracold Atoms on Optical Lattices*, PhD thesis, University of Stuttgart, 2004.
- [34] M. RIGOL and A. MURAMATSU, *Mod. Phys. Lett. B* **19**, 861 (2005).

- [35] M. OLSHANII, *Phys. Rev. Lett.* **81**, 938 (1998).
- [36] D. S. PETROV, G. V. SHLYAPNIKOV, and J. T. M. WALRAVEN, *Phys. Rev. Lett.* **85**, 3745 (2000).
- [37] V. DUNJKO, V. LORENT, and M. OLSHANII, *Phys. Rev. Lett.* **86**, 5413 (2001).
- [38] V. I. ARNOLD, *Mathematical Methods of Classical Mechanics*, Springer Verlag, New York, 1989.
- [39] L. D. LANDAU, *Soviet. Phys. JETP* **3**, 920 (1957).
- [40] L. D. LANDAU, *Soviet. Phys. JETP* **5**, 101 (1957).
- [41] L. D. LANDAU, *Soviet. Phys. JETP* **8**, 70 (1958).
- [42] K. SCHÖNHAMMER, Luttinger Liquids: The Basic Concepts, in *Strong Interactions in Low Dimensions*, edited by D. BAERISWYL and L. DEGIORGI, volume 25 of *Physics and Chemistry of Materials with Low-Dimensional Structures*, pp. 93–136, Kluwer Academic Publishers, 2004.
- [43] T. GIAMARCHI, *Quantum Physics in One Dimension*, volume 121 of *International Series of Monographs on Physics*, Oxford University Press, 2004.
- [44] S. TOMONAGA, *Progr. Theor. Phys.* **5**, 544 (1950).
- [45] J. M. LUTTINGER, *J. Math. Phys.* **4**, 1154 (1963).
- [46] J. SÓLYOM, *Adv. Phys.* **28**, 201 (1979).
- [47] F. GEBHARD, *The Mott Metal-Insulator Transition*, Springer-Verlag, Berlin, 1997.
- [48] F. D. M. HALDANE, *Phys. Rev. Lett.* **45**, 1358 (1980).
- [49] F. D. M. HALDANE, *Journal of Physics C: Solid State Physics* **14**, 2585 (1981).
- [50] V. MEDEN and K. SCHÖNHAMMER, *Phys. Rev. B* **46**, 15753 (1992).
- [51] J. VOIT, *Phys. Rev. B* **47**, 6740 (1993).
- [52] C. KOLLATH, U. SCHOLLWÖCK, and W. ZWERGER, *Phys. Rev. Lett.* **95**, 176401 (2005).
- [53] X. G. WEN, *Phys. Rev. B* **43**, 11025 (1991).

- [54] A. M. CHANG, L. N. PFEIFFER, and K. W. WEST, *Phys. Rev. Lett.* **77**, 2538 (1996).
- [55] R. CLAESSEN, M. SING, U. SCHWINGENSCHLÖGL, P. BLAHA, M. DRESSEL, and C. S. JACOBSEN, *Phys. Rev. Lett.* **88**, 096402 (2002).
- [56] M. SING, U. SCHWINGENSCHLÖGL, R. CLAESSEN, P. BLAHA, J. M. P. CARMELO, L. M. MARTELO, P. D. SACRAMENTO, M. DRESSEL, and C. S. JACOBSEN, *Phys. Rev. B* **68**, 125111 (2003).
- [57] H. BENTHIEN, F. GEBHARD, and E. JECKELMANN, *Phys. Rev. Lett.* **92**, 256401 (2004).
- [58] H. BENTHIEN, *Dynamical Properties of Quasi One-Dimensional Correlated Electron Systems*, PhD thesis, University of Marburg, 2005.
- [59] S. SACHDEV, *Quantum Phase Transitions*, Cambridge University Press, Cambridge, 1999.
- [60] J. M. YEOMANS, *Statistical Mechanics of Phase Transitions*, Oxford University Press, 1992.
- [61] C. AEBISCHER, *Dielectric Catastrophe at the Mott Transition*, PhD thesis, Université de Fribourg (Suisse), 2002.
- [62] C. AEBISCHER, D. BAERISWYL, and R. M. NOACK, *Phys. Rev. Lett.* **86**, 468 (2001).
- [63] K. KIM and P. B. WEICHMAN, *Phys. Rev. B* **43**, 13583 (1991).
- [64] C. COHEN-TANNOUJJI, B. DIU, and F. LALOE, *Quantum Mechanics*, Wiley-Interscience, 1977.
- [65] M. RIGOL, A. MURAMATSU, G. G. BATROUNI, and R. T. SCALETTAR, *Phys. Rev. Lett.* **91**, 130403 (2003).
- [66] G. G. BATROUNI, V. ROUSSEAU, R. T. SCALETTAR, M. RIGOL, A. MURAMATSU, P. J. H. DENTENEER, and M. TROYER, *Phys. Rev. Lett.* **89**, 117203 (2002).
- [67] M. RIGOL and A. MURAMATSU, *Phys. Rev. A* **69**, 053612 (2004).
- [68] T. STÖFERLE, H. MORITZ, C. SCHORI, M. KÖHL, and T. ESSLINGER, *Phys. Rev. Lett.* **92**, 130403 (2004).
- [69] M. GIRARDEAU, *J. Math. Phys.* **1**, 516 (1960).

- [70] T. KINOSHITA, T. WENGER, and D. S. WEISS, *Science* **305**, 1125 (2004).
- [71] R. GRIMM, M. WEIDEMÜLLER, and Y. B. OVCHINNIKOV, *Adv. At. Mol. Opt. Phys.* **42**, 95 (2000).
- [72] J. L. LEBOWITZ and O. PENROSE, *Physics Today* **26**, 155 (1973).
- [73] http://en.wikipedia.org/wiki/Chaos_theory/.
- [74] F. HAAKE, *Quantum Signatures of Chaos*, Springer, Berlin, 2nd edition, 2001.
- [75] A. R. KOLOVSKY and A. BUCHLEITNER, *Europhysics Letters* **68**, 632 (2004).
- [76] J. BERGES, S. BORSANYI, and C. WETTERICH, *Phys. Rev. Lett.* **93**, 142002 (2004).
- [77] K. SENGUPTA, S. POWELL, and S. SACHDEV, *Phys. Rev. A* **69**, 053616 (2004).
- [78] C. KOLLATH, A. LAEUCHLI, and E. ALTMAN, *cond-mat/0607235* (unpublished).
- [79] H. TASAKI, *Phys. Rev. Lett.* **80**, 1373 (1998).
- [80] E. T. JAYNES, *Phys. Rev.* **106**, 620 (1957).
- [81] R. BALIAN, *From Microphysics to Macrophysics*, Texts and Monographs in Physics, Springer, 1982.
- [82] M. RIGOL, V. DUNJKO, V. YUROVSKY, and M. OLSHANII, *cond-mat/0604476* (2006).
- [83] M. RIGOL, A. MURAMATSU, and M. OLSHANII, *Phys. Rev. A* **74**, 053616 (2006).
- [84] M. A. CAZALILLA, *Phys. Rev. Lett.* **97**, 156403 (2006).
- [85] W. H. PRESS, S. A. TEUKOLSKY, W. T. VETTERLING, and B. P. FLANNERY, *Numerical Recipes in C++*, Cambridge University Press, 2nd edition, 1993.
- [86] H. Q. LIN, *Phys. Rev. B* **42**, 6561 (1990).
- [87] O. GOLINELLI, T. JOLICŒUR, and R. LACAZE, *Phys. Rev. B* **50**, 3037 (1994).
- [88] A. L. MALVEZZI, *Braz. Journ. of Phys.* **33** (March 2003).
- [89] N. LAFLORENCIE and D. POILBLANC, *Lect. Notes Phys.* **645**, 227 (2004).

- [90] A. LÄUCHLI, (talk given at the first ALPS users' workshop in Lugano, Sept. 2004, http://www.comp-phys.org:16080/lugano04/Talks/QLM_ED.pdf).
- [91] B. N. PARLETT, *The Symmetric Eigenvalue Problem*, Prentice-Hall, Englewood Cliffs, New Jersey, 1980.
- [92] G. H. GOLUB and C. F. V. LOAN, *Matrix Computations*, Johns Hopkins University Press, 3rd edition, 1996.
- [93] D. S. WATKINS, *Fundamentals of Matrix Computations*, Wiley-Interscience, 2nd edition, 2002.
- [94] Z. BAI, J. DEMMEL, J. DONGARRA, A. RUHE, and H. VAN DER VORST, editors, *Templates for the Solution of Algebraic Eigenvalue Problems: a Practical Guide*, SIAM, 2000.
- [95] J. K. CULLUM and R. A. WILLOUGHBY, *Lanczos algorithms for large symmetric eigenvalue computations*, volume 1, Progress in Scientific Computing, 1985.
- [96] C. LÁNCZOS, *J. Res. Natl. Bur. Stand* **45**, 225 (1950).
- [97] E. DAGOTTO, *Rev. Mod. Phys.* **66**, 763 (1994).
- [98] J. K. CULLUM and R. A. WILLOUGHBY, *J. Comput. Phys.* , 44:329 (1981).
- [99] **Arnoldi Package** (ARPACK, a collection of Fortran subroutines).
- [100] **Iterative Eigensolver Template Library** (IETL, provides generic C++ routines).
- [101] A. LAUCHLI and D. POILBLANC, *Phys. Rev. Lett.* **92**, 236404 (2004).
- [102] G. ROUX, S. R. WHITE, S. CAPPONI, A. LAUCHLI, and D. POILBLANC, *Phys. Rev. B* **72**, 014523 (2005).
- [103] A. A. ALIGIA, K. HALLBERG, B. NORMAND, and A. P. KAMPF, *Phys. Rev. Lett.* **93**, 076801 (2004).
- [104] B. DAMSKI, H.-U. EVERTS, A. HONECKER, H. FEHRMANN, L. SANTOS, and M. LEWENSTEIN, *Phys. Rev. Lett.* **95**, 060403 (2005).
- [105] E. R. DAVIDSON, *J. Comput. Phys.* **17**, 87 (1975).
- [106] G. L. G. SLEIPEN and H. A. VAN DER VORST, *SIAM J. Matrix Anal. Appl.* **17**, 401 (1996).

- [107] A. J. DALEY, C. KOLLATH, U. SCHOLLWÖCK, and G. VIDAL, *J. Stat. Mech.: Theor. Exp.*, P04005 (2004).
- [108] C. MOLER and C. V. LOAN, *SIAM Review* **45**, 3 (2003).
- [109] M. HOCHBRUCK and C. LUBICH, *BIT* **Vol. 39**, pp 620 (1999).
- [110] M. HOCHBRUCK, C. LUBICH, and H. SELHOFER, *SIAM J. Sci. Comput.* **Vol. 19**, pp 1552 (1998).
- [111] S. R. WHITE and R. M. NOACK, *Phys. Rev. Lett.* **68**, 3487 (1992).
- [112] K. HALLBERG, *Adv. Phys.* **55** (2006).
- [113] F. B. ANDERS and A. SCHILLER, *Phys. Rev. Lett.* **95**, 196801 (2005).
- [114] R. M. NOACK and S. R. WHITE, The Density Matrix Renormalization Group, in *Density Matrix Renormalization - A New Numerical Method in Physics*, edited by I. PESCHEL, X. WANG, M. KAULKE, and K. HALLBERG, pp. 27–66, Springer Verlag, 1999.
- [115] M. A. MARTÍN-DELGADO, G. SIERRA, and R. M. NOACK, *J. Phys. A: Math. Gen.* **32**, 6079 (1999).
- [116] K. HALLBERG, Density Matrix Renormalization, in *Theoretical Methods for Strongly Correlated Electrons*, edited by D. SÉNÉCHAL, A.-M. TREMBLAY, and C. BOURBONNAIS, CRM Series in Mathematical Physics, pp. 3–38, Springer Verlag, 2004.
- [117] <http://quattro.phys.sci.kobe-u.ac.jp/dmrg/condmat.html>, maintained by T. Nishino, updated daily.
- [118] <http://komet337.physik.uni-mainz.de/Jeckelmann/DMRG/>, maintained by E. Jeckelmann.
- [119] L. D. LAUNDAU and E. M. LIFSHITZ, *Course on theoretical physics: Quantum Mechanics*, volume 3, Pergamon Press, New York, 1965.
- [120] R. P. FEYNMAN, *Statistical Mechanics: A Set of Lectures*, Benjamin, Reading, MA, 1972.
- [121] E. SCHMIDT, *Math. Annalen* **63**, 433 (1907).
- [122] <http://theory.caltech.edu/people/preskill/ph229/>, "Quantum Computation", lecture notes by J. Preskill.

- [123] S. R. WHITE, *Phys. Rev. B* **48**, 10345 (1993).
- [124] C. D. E. BOSCHI and F. ORTOLANI, *Eur. Phys. J. B* **41**, 503 (2004).
- [125] S. R. WHITE and D. HUSE, *Phys. Rev. B* **48**, 3844 (1993).
- [126] S. R. WHITE and I. AFFLECK, *Phys. Rev. B* **54**, 9862 (1996).
- [127] R. M. NOACK, S. R. WHITE, and D. J. SCALAPINO, The Density-Matrix Renormalization Group for Fermion Systems, in *Computer Simulations in Condensed Matter Physics VII*, edited by D. P. LANDAU, K. K. MON, and H. B. SCHÜTTLER, pp. 85–98, Heidelberg, Berlin, 1994, Springer Verlag.
- [128] R. M. NOACK, S. DAUL, and S. KNEER, Properties of the Hubbard Chain, in *Density Matrix Renormalization - A New Numerical Method in Physics*, edited by I. PESCHEL, X. WANG, M. KAULKE, and K. HALLBERG, pp. 197–209, Springer Verlag, 1999.
- [129] S. R. MANMANA, V. MEDEN, R. M. NOACK, and K. SCHÖNHAMMER, *Phys. Rev. B* **70**, 155115 (2004).
- [130] I. P. McCULLOCH and M. GULACSI, *Aust. J. Phys.* **53**, 597 (2000).
- [131] I. P. McCULLOCH and M. GULACSI, *Philos. Mag. Lett.* **81**, 447 (2001).
- [132] I. P. McCULLOCH, A. R. BISHOP, and M. GULACSI, *Philos. Mag. B* **81**, 1603 (2001).
- [133] K. HALLBERG, *Phys. Rev. B* **52**, 9827 (1995).
- [134] T. D. KÜHNER and S. R. WHITE, *Phys. Rev. B* **60**, 335 (1999).
- [135] C. RAAS, G. S. UHRIG, and F. B. ANDERS, *Phys. Rev. B* **69**, 041102(R) (2004).
- [136] E. JECKELMANN, *Phys. Rev. B* **66**, 045114 (2002).
- [137] S. ÖSTLUND and S. ROMMER, *Phys. Rev. Lett.* **75**, 3537 (1995).
- [138] N. NAGAOSA and J. TAKIMOTO, *J. Phys. Soc. Jpn* **55**, 2735 (1986).
- [139] J. HUBBARD and J. TORRANCE, *Phys. Rev. Lett.* **47**, 1750 (1981).
- [140] T. EGAMI, S. ISHIHARA, and M. TACHIKI, *Science* **261**, 1307 (1993).
- [141] Z. SOOS and S. MAZUMDAR, *Phys. Rev. B* **18**, 1991 (1978).
- [142] R. RESTA and S. SORELLA, *Phys. Rev. Lett.* **74**, 4738 (1995).

- [143] P. STREBEL and Z. SOOS, *J. Chem. Phys.* **53**, 4077 (1970).
- [144] G. ORTIZ, P. ORDEJÓN, R. MARTIN, and G. CHIAPPE, *Phys. Rev. B* **54**, 13515 (1996).
- [145] T. WILKENS and R. MARTIN, *Phys. Rev. B* **63**, 235108 (2001).
- [146] M. C. REFOLIO, J. M. L. SANCHO, and J. RUBIO, *Phys. Rev. B* **72**, 035121 (2005).
- [147] M. TORIO, A. ALIGIA, and H. CECCATTO, *Phys. Rev. B* **64**, 121105 (2001).
- [148] N. GIDOPOULOS, S. SORELLA, and E. TOSATTI, *Eur. Phys. J. B* **14**, 217 (2000).
- [149] Y. ANUSOOYA-PATI, Z. SOOS, and A. PAINELLI, *Phys. Rev. B* **63**, 205118 (2001).
- [150] A. KAMPF, M. SEKANIA, G. JAPARIDZE, and P. BRUNE, *J. Phys.: Condens. Matter* **15**, 5895 (2003).
- [151] Y. TAKADA and M. KIDO, *J. Phys. Soc. Jpn.* **70**, 21 (2001).
- [152] J. LOU, S. QIN, T. XIANG, C. CHEN, G.-S. TIAN, and Z. SU, *Phys. Rev. B* **68**, 045110 (2003).
- [153] Y. ZHANG, C. WU, and H. LIN, *Phys. Rev. B* **67**, 205109 (2003).
- [154] S. CAPRARA, M. AVIGNON, and O. NAVARRO, *Phys. Rev. B* **61**, 15667 (2000).
- [155] S. GUPTA, S. SIL, and B. BHATTACHARYYA, *Phys. Rev. B* **63**, 125113 (2001).
- [156] K. POŽGAJČIĆ and C. GROS, *Phys. Rev. B* **68**, 085106 (2003).
- [157] S. R. MANMANA, *Vom Bandisolator zum Mott-Hubbard-Isolator in einer Raumdimension*, Diploma thesis, Georg-August-Universität Göttingen, 2002.
- [158] J. VOIT, *J. Phys. C: Solid State Phys.* **21**, L1141 (1988).
- [159] J. DES CLOIZEAUX and J. PEARSON, *Phys. Rev.* **128**, 2131 (1962).
- [160] A. GIRLANDO and A. PAINELLI, *Phys. Rev. B* **34**, 2131 (1986).
- [161] E. JECKELMANN, *Phys. Rev. Lett.* **89**, 236401 (2002).
- [162] A. A. ALIGIA, *Phys. Rev. B* **69**, 041101 (2004).

- [163] U. SCHOLLWÖCK, *J. Phys. Soc. Jpn. (Suppl.)* **74**, 246 (2005).
- [164] M. A. CAZALILLA and J. B. MARSTON, *Phys. Rev. Lett.* **88**, 256403 (2002).
- [165] H. G. LUO, T. XIANG, and X. Q. WANG, *Phys. Rev. Lett.* **91**, 049701 (2003).
- [166] P. SCHMITTECKERT, *Phys. Rev. B* **70**, 121302(R) (2004).
- [167] D. GOBERT, C. KOLLATH, U. SCHOLLWÖCK, and G. SCHÜTZ, *Phys. Rev. E* **71**, 036102 (2005).
- [168] A. E. FEIGUIN and S. R. WHITE, *Phys. Rev. B* **72**, 020404(R) (2005).
- [169] G. VIDAL, *Phys. Rev. Lett.* **93**, 040502 (2004).
- [170] S. R. WHITE and A. E. FEIGUIN, *Phys. Rev. Lett.* **93**, 076401 (2004).
- [171] C. KOLLATH, *The adaptive time-dependent density-matrix renormalization-group method: development and applications*, PhD thesis, RWTH Aachen, 2005.
- [172] Oral communication by K. Rodriguez.
- [173] M. RIGOL and A. MURAMATSU, *Phys. Rev. A* **70**, 031603 (2004).
- [174] M. RIGOL and A. MURAMATSU, *Phys. Rev. A* **72**, 013604 (2005).
- [175] M. RIGOL and A. MURAMATSU, *Phys. Rev. Lett.* **94**, 240403 (2005).
- [176] A. W. SANDVIK, *Phys. Rev. B* **59**, R14157 (1999).
- [177] J. GUBERNATIS, D. SCALAPINO, R. SUGAR, and W. TOUSSAINT, *Phys. Rev. B* **32**, 103 (1985).
- [178] C. N. YANG and C. P. YANG, *Phys. Rev.* **150**, 321 (1966).
- [179] S. R. MANMANA, A. MURAMATSU, and R. M. NOACK, *AIP Conf. Proc.* **789**, 269 (2005).
- [180] Oral communication by D. S. Weiss.
- [181] K. RODRIGUEZ, S. R. MANMANA, R. M. NOACK, and A. MURAMATSU, in preparation.
- [182] <http://www.attoworld.de/>.

Publications

Parts of this thesis have been published or a publication is in preparation at the time of writing. A complete list of publications can be obtained at

http://www.theo3.physik.uni-stuttgart.de/salva/publika_e.html

The publications relevant for this thesis are listed in the following:

Submitted:

1. S.R. Manmana, S. Wessel, R.M. Noack, and A. Muramatsu,
Strongly Correlated Fermions After a Quantum Quench,
Submitted to Phys. Rev. Lett.

Peer-Reviewed Journals:

1. K. Rodriguez, S.R. Manmana, M. Rigol, R.M. Noack, and A. Muramatsu,
Coherent matter waves emerging from Mott-insulators,
New J. Phys. **8**, 169 (2006).
Invited paper to the focus issue “Cold Atoms in Optical Lattices”.
2. The ALPS collaboration (F. Alet, *et al.*),
The ALPS Project: Open Source Software for Strongly Correlated Systems,
J. Phys. Soc. Jpn. Suppl. **74**, 30 (2005).
3. S.R. Manmana, V. Meden, R.M. Noack, and K. Schönhammer,
Quantum Critical Behavior of the One-Dimensional Ionic Hubbard Model,
Phys. Rev. B **70**, 155115 (2004).

Review Articles:

1. R.M. Noack and S.R. Manmana,
Diagonalization- and Numerical Renormalization-Group-Based Methods for Interacting Quantum Systems,
Lecture Notes for the Conference Proceedings “IX. Training Course in the Physics of Correlated Electron Systems and High-Tc Superconductors”,
AIP Conference Proceedings **789**, 93 – 163 (2005).

Conference Proceedings:

1. S.R. Manmana, A. Muramatsu, and R.M. Noack,
Collapse and Revival Starting from a Luttinger Liquid,
Conference Proceedings, ESF Exploratory Workshop “Effective Models for Low-Dimensional Strongly Correlated Systems”,
AIP Conference Proceedings **816**, 198 – 203 (2006).

2. S.R. Manmana, A. Muramatsu, and R.M. Noack,
Time Evolution of One-Dimensional Quantum Many Body Systems,
Conference Proceedings “IX. Training Course in the Physics of Correlated
Electron Systems and High-Tc Superconductors”,
AIP Conference Proceedings **789**, 269 – 278 (2005).

Lebenslauf

Nachname: Manmana

Vornamen: Salvatore Rosario

Staatsangehörigkeit: italienisch

Geburtsdatum: 16. November 1976

Geburtsort: Catania (Italien)

Familienstand: ledig

1983-1987: Grundschule: *Anton-Bruckner-Schule*, Ludwigsburg

1987-1996: Gymnasium: *Friedrich-Schiller-Gymnasium*, Ludwigsburg

Juni 1996 Abitur

1996-1998: Universität Stuttgart: Physikstudium

1998-1999: *Eötvös-Loránd Universität* Budapest (Ungarn): Physikstudium

Studentenprojekt: *“Decoherence in a Semi-Classical Two-Body System”*

1999-2002: *Georg-August Universität*, Göttingen: Physikstudium

Juni 2002 Diplom in Physik; Titel der Diplomarbeit:

“Vom Bandisolator zum Mott-Hubbard-Isolator in einer Raumdimension”

Betreuer: Prof. K. Schönhammer

2002-2006: Doktorand an den Universitäten in Stuttgart und in Marburg

Themengebiet: *“Zeitentwicklung stark korrelierter Quantensysteme”*

Betreuer: Prof. R.M. Noack und Prof. A. Muramatsu

Acknowledgements

During my PhD, I was supported from many sides and by many persons. First of all I would like to thank Reinhard Noack and Alejandro Muramatsu for their supervision and the many (nearly continuous) interesting discussions, and for the proposal and encouragement to work on time-dependent extensions for the DMRG. Especially I would like to thank them for their permanent support and their agreement to try to do a “shared” PhD between Marburg and Stuttgart, understanding that it was of great importance for me in this difficult time to be in Stuttgart at least a good part of my time.

Because of my rather delocalized existence as a (quantum?) traveller between Marburg and Stuttgart, I am indebted to persons from both places and I would like to express my gratitude to all of them; their attitude towards me was always open, sincere and humorous. Especially I would like to thank Florian Gebhard who was always happy to discuss about physics (and other topics) and who could give me good advice in various situations. My work would have not been possible if the system administrators at both places would not have done such a good job; I am indebted to Catia Lavallo and Marcos Rigol in Stuttgart and to Leo Tincani in Marburg for their excellent work. I acknowledge many many nice and interesting discussions with all three of them and having a really good time at both places. In addition, I am indebted to Marcos Rigol for his data for the HCBs and for his helpful suggestions. The responsibility for having a good time at both institutes is not only shared between these three and the professors, but also many more had their share in it. I would like to point out that at both places the coffee is quite good and that, especially after lunch, there were many possibilities for nice and interesting discussions about physics (and general topics) with Mitsuhiro Arikawa, Stefan Wessel, Catia Lavallo, Stefano Giovanazzi, Jürgen Falb, Stefan Harrer, Farshid Karim Pour, Gerhard Loske, Luis Santos, Paolo Pedri, Martin Feldbacher, Fakher Assaad, Fatiha Ouchni and Heiko Gimperlein at the Stuttgart coffee round. I am especially indebted to Stefan Wessel for the countless discussions about our results at the end of the PhD and that he really always found the time to discuss. I also acknowledge Karen Rodriguez and Arturo Arguelles for many nice discussions about topics related to DMRG (and not related to DMRG).

In Marburg, the nice time was due to (in addition to the above mentioned) Holger Benthien, Anja Grage, Satoshi Ejima, Satoshi Nishimoto, Jörg Bühnemann, and Jörg Rissler. I acknowledge all the interesting discussions, not only about physics. I also enjoyed having the possibility to discuss with Örs Legeza during his stays in Marburg.

Of great importance was the help in administrative problems, that I always obtained by the secretaries of both groups, Frau Poljak and Frau von den Bergen, whom I would like to thank in this place.

Especially at the beginning of my PhD while working on the ionic Hubbard model, we had many discussions with Volker Meden, who I want to acknowledge at this point. I also would like to acknowledge all the good and interesting discussions with many people who I met on the workshops that I attended.

I want to express my gratitude to my family, who was always an important support for me. Celia Vogel I thank for the many nice conversations and movie evenings, wishing her that she will manage the final part of her PhD. I also want to thank all my friends who were a continuous support and for the good time we had together.

Last, but not least, I acknowledge financial support by the SFB 382, by the SFB/TR 21, and by the European Graduate College / DFG-OTKA International Research Training Group “Electron-Electron Interactions in Solids” in Marburg and Budapest. I also acknowledge HLRS Stuttgart and NIC Jülich for the allocation of CPU time. Finally, I would like to express my gratitude to all the ones who contributed during this time, but who I have forgotten to mention here, hoping that they are not angry about my forgetfulness. I acknowledge the Deutsche Bahn for providing their trains with plugs so that I could continue using my Laptop during my travels.